

This manuscript is a preprint. Although it has undergone journal-led peer-review, it has yet to be accepted. Subsequent versions of this manuscript may thus have different content. If accepted, the final version of this manuscript will be available via the 'Peer-reviewed Publication DOI' link on the right-hand side of this webpage.

Please feel free to contact any of the authors directly or to comment on the manuscript using [hypothes.is](https://web.hypothes.is/)(<https://web.hypothes.is/>). We welcome feedback!

1 **Deep-water reservoir distribution on a salt-influenced slope,**  
2 **Santos Basin, offshore Brazil**

3

4 C. R. Rodriguez<sup>1§</sup>, C. A-L. Jackson<sup>2</sup>, R. E. Bell<sup>2</sup>, A. Rotevatn<sup>3</sup>, M. Francis<sup>4</sup>5 *<sup>1</sup>Exploration Multiclient, WesternGeco Schlumberger, 10001 Richmond Avenue, Houston,*  
6 *Texas, 77042, United States.*7 *<sup>2</sup>Basins Research Group (BRG), Department of Earth Science and Engineering, Imperial*  
8 *College London, SW7 2BP, United Kingdom*9 *<sup>3</sup>Department of Earth Science, University of Bergen, Allégaten 41, 5007 Bergen, Norway*10 *<sup>4</sup>WesternGeco Schlumberger, Schlumberger House, Gatwick Airport, Horley, West Sussex,*  
11 *RH6 0NZ, United Kingdom*12 §Corresponding author email: [clararodriguez@slb.com](mailto:clararodriguez@slb.com)

13

14 **Abstract**15 Studies of near-seabed datasets show that salt tectonics controls the distribution and  
16 architecture of deep-water reservoirs in many salt-influenced basins. It is typically difficult,  
17 however, to study the distribution and stratigraphic evolution of depositional systems  
18 preserved at deeper, economically significant depths, reflecting poor seismic imaging of  
19 steeply dipping strata flanking high-relief salt structures. 3D seismic and borehole data from  
20 the Santos Basin, offshore Brazil allow us to identify a range of depositional elements that  
21 form the building blocks of three main tectono-stratigraphic phases. During the first phase,  
22 channel systems and lobes were confined within updip minibasins and to the hangingwalls of  
23 salt-detached faults. During the second phase, channel systems and lobes filled updip  
24 minibasins to bypass sediment downslope, with coarse clastic deposition then occurring in

25   downdip minibasins, >100 km from the coeval shelf margin. Syndepositional seafloor relief  
26   caused: (i) channel system deflection and diversion around salt-cored highs; (ii) channel  
27   system uplift and rotation on the flanks of rising salt structures; (iii) lateral and frontal  
28   confinement of channel systems. During the final phase, rising salt walls dissected previously  
29   deposited deep-water systems, with MTCs deposition becoming increasingly important. Our  
30   results have important implications for post-salt prospectivity in the Santos Basin and other  
31   salt-influenced sedimentary basins, with a range of reservoirs and trapping styles present in  
32   this underexplored interval. More specifically, we show that large volumes of clastic sediment  
33   were not trapped behind the 'Albian Gap', a salt-controlled depocenter dominating the north-  
34   western basin margin, but were instead delivered further basinward.

35

## 36   **1. Introduction**

37   Understanding the spatial distribution and temporal evolution of deep-water depositional  
38   systems relative to the style and evolution of seafloor relief is key to improving the ability to  
39   predict reservoir presence, architecture and hydrocarbon trapping styles along deep-water  
40   slopes. Seafloor relief and related controls on sediment distribution and architecture can be  
41   induced by: (i) tectonic events (e.g., Hubbard et al., 2009; Callec et al., 2010; Lin et al., 2014;  
42   Spychala et al., 2017; McArthur et al., 2019); (ii) erosional and depositional features (e.g.,  
43   Deptuck et al., 2007; Kolla, 2007; Ortiz-Karpf et al., 2015; Spychala et al., 2015); (iii) mud  
44   diapirism (e.g., Morley et al., 2003; Adeogba et al., 2005); and (iv) salt movement (e.g. Rowan  
45   and Weimer, 1998; Stewart and Clark, 1999; Booth et al., 2003; Gee and Gawthorpe, 2006;  
46   Jackson et al., 2010; Mayall et al., 2010; Oluboyo et al., 2014; Doughty-Jones et al., 2017).

47 Here we focus on understanding how salt-induced seafloor relief interacts with deep-water  
48 sedimentation, thus controlling reservoir distribution and architecture and related trapping  
49 styles along deep-water slopes (e.g. Booth et al., 2003; Gee and Gawthorpe, 2006, 2007;  
50 Jackson et al., 2010; Mayall et al., 2010; Oluboyo et al., 2014; Sylvester et al., 2015; Doughty-  
51 Jones et al., 2017; Wang et al., 2017). Overall, these studies suggest that the style of salt-  
52 sediment interaction is a result of; i) the nature (e.g. grain-size, erosive power, etc) and  
53 temporal evolution of deep-water depositional systems; ii) downdip changes in salt-related  
54 structural style (i.e., from predominantly thin-skinned extensional styles near the updip basin  
55 margins, to thin-skinned contractional styles towards the basin center), with a key control  
56 being the orientation, scale and growth rate of structures relative to the incoming deep-water  
57 systems; and iii) the timing of sediment deposition relative to the formation, growth and  
58 decay of salt-induced seafloor relief.

59 Salt-induced seafloor relief can lead to lateral confinement, frontal confinement or blocking,  
60 deflection and diversion of deep-water depositional systems (e.g., Clark and Cartwright 2009;  
61 2011; Mayall et al., 2010). Furthermore, sediment subsidence into salt can lead to the  
62 formation of minibasin; i.e., relatively small (5-30 km in diameter by up to several kilometres  
63 deep) synsedimentary depocenters (e.g. Jackson and Talbot, 1991; Hudec and Jackson, 2007,  
64 2011; Hudec et al., 2009; Goteti et al., 2012). In salt-influenced slopes, deep-water  
65 depositional systems may fill updip minibasins before spilling into neighbouring downdip  
66 minibasins, showing progressive basinward filling or “healing” of the slope (e.g. Winker, 1996;  
67 Prather et al., 1998; Badalini et al., 2000; Booth et al., 2003; Smith, 2004; Hudec et al., 2009;  
68 Albertão et al., 2011; Jackson et al., 2010; Oluboyo et al., 2014).

69

70 Seismic reflection data are a key tool to understand how salt-influenced seafloor relief  
71 controls deep-water sediment distribution and stratigraphic architecture. Most previous  
72 seismic reflection-based studies have focused on shallowly buried (i.e. near-seafloor),  
73 relatively young deep-water depositional systems that are then used to understand salt-  
74 sediment interactions in older, more deeply buried systems (e.g., Winker, 1996; Beaubouef  
75 and Friedmann, 2000; Pirmez et al., 2000; Fonnesu, 2003; Gee and Gawthorpe, 2006, 2007;  
76 Clark and Cartwright, 2009; 2011). The salt-influenced geometry and temporal evolution of  
77 deeply buried systems have also been studied, but only over relatively small areas (within a  
78 single or a few closely spaced minibasins; e.g., Booth et al., 2003; Jones et al. 2012). In  
79 contrast, regional studies cover many minibasins, but have typically focused on detailed  
80 analysis of specific stratigraphic intervals recording relatively short time scales (ca. 15 Myrs;  
81 e.g.; Olubuyo et al., 2014).

82 This study focuses on central deep-water Santos Basin, offshore eastern Brazil. Here, high-  
83 quality seismic reflection and borehole data provide a rare opportunity to analyse deep  
84 Turonian-to-Paleocene deep-water clastic systems that were deposited on a salt-influenced  
85 slope. In contrast to previous studies, our data allow us to document the long-term (ca. 60  
86 Myrs) stratigraphic record of salt-sediment interaction across >10 minibasins that cover an  
87 area of c. 20,122 km<sup>2</sup>. Previous studies in the Santos Basin predict that little or no deep-water  
88 sand was deposited during the Turonian-to-Paleocene due to the presence of a salt-controlled  
89 intra-slope depocenter called the 'Albian Gap' (e.g.; Modica and Brush, 2004; Guerra and  
90 Underhill, 2012). In this study, we challenge the conclusions of these previous studies,  
91 showing evidence for the existence of deep-water depositional elements up to 100 km from  
92 the coeval shelf margin. More specifically, we: i) document the spatial and temporal variations

93 in the size and type of deep-water depositional elements within the post-salt succession; ii)  
94 assess the key controls on minibasin development, paleo-seafloor relief and deep-water  
95 stratigraphic architecture; and iii) determine the exploration significance of this hitherto  
96 poorly explored succession. This study improves our current understanding of the distribution  
97 of and controls on, depositional systems along salt-influenced deep-water slopes, providing  
98 new insights into the tectono-stratigraphic evolution of this salt-dominated basin.

99

## 100 **2. Geological Setting**

101 The study area is located on the São Paulo Plateau (SPP), Santos Basin, offshore eastern Brazil  
102 (Figs. 1 a,b). The Santos Basin formed during the opening of the South Atlantic in the earliest  
103 Cretaceous, with the main Hauretivan rift phase being characterized by the development of  
104 half-graben filled with fluvial and lacustrine sediments (Guaratiba Group; Fig. 1c) (Meisling et  
105 al., 2001; Modica and Brush, 2004; Moreira et al., 2007). The end of the rift phase was marked  
106 by the deposition of the main source rocks and reservoirs in the Santos Basin; these included  
107 organic-rich lacustrine mudstones and carbonates of the Barremian 'sag' sequence (upper  
108 Guaratiba Group), which largely filled and smoothed relict rift-related topography (Fig. 1c;  
109 Meisling et al., 2001; Modica and Brush, 2004; Moreira et al., 2007). Episodic marine  
110 incursions and an arid climate during the Aptian promoted deposition of the Ariri Formation,  
111 an up-to-2.5 km-thick evaporite-dominated succession (Fig. 1 c, d-; e.g. Modica and Brush,  
112 2004; Davison, 2007; Karner and Gambôa, 2007; Moreira et al., 2007; Gambôa et al., 2008;  
113 Davison et al., 2012; Fiduk and Rowan, 2012; Jackson et al., 2014a; Rodriguez et al., 2018).  
114 During the Albian, a shallow-marine carbonate platform was established near the basin

115 margin, with deep-water marlstones deposited basinward in deeper waters (Itanhaem  
116 Formation; Figs. 1c,d; e.g., Modica and Brush, 2004). Salt-related deformation commenced in  
117 the Albian, with margin tilting and the downslope flow of salt causing stretching and faulting  
118 of the carbonate platform, and the development of normal fault-bound rafts in the upslope  
119 extensional domain (Fig. 1c; e.g.; Davison et al., 2012; Guerra and Underhill, 2012; Jackson,  
120 2012).

121 In the Late Cretaceous, periodic uplift and erosion of the onshore Serra do Mar mountain belt  
122 drove progradation of a thick clastic wedge into the Santos Basin (Itajai-Acu Formation; Fig.  
123 1c,d; e.g., Modica and Brush, 2004; Moreira et al., 2007; Guerra and Underhill, 2012). Regional  
124 paleogeographic mapping based on widely spaced 2D seismic reflection and limited borehole  
125 data suggest large volumes of sediment were supplied by the Paraíba do Sul river drainage  
126 system, which at this time lay to the N and NW of the São Paulo Plateau (Fig. 2a, Modica and  
127 Brush, 2004). However, according to Modica and Brush (2004), much of this sediment was  
128 trapped in a relatively proximal setting due to formation of the Albian Gap, a large (4 km thick,  
129 200 km long, 10 km wide), salt-controlled, intraslope depocenter bounding the seaward limit  
130 of the extensional domain (Figs. 2 a,b; Jackson et al., 2015a). The interpretation of Modica  
131 and Brush (2004) thus argues for limited sediment dispersal to the slope during the Late  
132 Cretaceous, implying limited deep-water prospectivity on the São Paulo Plateau (Fig. 2a). Late  
133 Campanian-Maastrichtian uplift of the Serra do Mar deflected the Paraíba do Sul river  
134 drainage system to the NE, starving the central deep-water Santos Basin of sediment (Fig. 2b;  
135 Cobbold et al., 2001; Modica and Brush, 2004; Guerra and Underhill, 2012). Subsequently,  
136 during the Eocene, sediment supply to the basin was thus largely derived from catastrophic  
137 failure of the middle Eocene shelf margin, which produced debris flows and turbidites of the

138 Lower Marambaia Formation that were locally trapped in the proximal domain (Fig. 2c).  
139 Previous studies also suggest the upper Marambaia Formation varies little in thickness and is  
140 dominated by fine-grained sediments, recording a global marine flooding event and sea level  
141 highstand (Figs. 1c, d; Modica and Brush, 2004; Moreira et al., 2007; Guerra and Underhill,  
142 2012).

143 By integrating 3D seismic reflection and borehole data we here show that: (i) deep-water  
144 systems of the Itajai-Acu Formation were deposited on the São Paulo Plateau, some distance  
145 seaward of the Albian Gap and the coeval Late Cretaceous shelf edge; and (ii) large thickness  
146 variations occur within the Marambaia Formation due to continue salt diapirism, and the  
147 emplacement of relatively small, intra-minibasin and larger, shelf-derived mass transport  
148 complexes (MTCs).

149

### 150 **3. Data and methods**

151 In this study, we integrate a 20,122 km<sup>2</sup>, high-quality, three-dimensional, post-stack time-  
152 migrated seismic reflection dataset provided by CGG, and eight publicly available boreholes  
153 (Fig. 1b). The dataset is located in the central deep-water Santos Basin, 200 km southeast of  
154 the present Brazilian shelf edge and 200 km southwest of the Campos Basin (Fig. 1b). The  
155 seismic dataset contains trace information from sea level down to 5.5 second two-way time  
156 (s, TWT), with a vertical sample rate of 4 ms, inline spacing (east-west) of 18.75 m and  
157 crossline spacing (north-south) of 25 m. Data from four boreholes indicate that vertical  
158 seismic resolution within the post-salt varies not only with depth, but also spatially due to  
159 variations in composition (Fig. 3, and Table 1). Vertical resolution within the post-salt



160 sequence decreases from c. 8 m at relatively shallow depths (<2500 ms TWT), to up to 31 m  
161 where the post-salt sequence is relatively thick (4500 ms TWT), to up to 64 m where the post-  
162 salt sequence is thickest (>5000 ms TWT) (Fig. 3 and Table 1). This decrease in seismic  
163 resolution limits the opportunity to identify and map depositional systems occurring deep  
164 within the post-salt sequence. Seismic profiles are displayed with SEGY normal polarity,  
165 where a downward increase in acoustic impedance is represented by a positive reflection  
166 event (red) and a downward decrease in acoustic impedance is represented by a negative  
167 reflection event (blue) (inset on Fig. 3). The boreholes contain lithology information and  
168 formation markers. Well-log data are restricted to the pre-salt and salt sequences. Only  
169 borehole 329D, which penetrates the center of a minibasin encircled by salt diapirs, contain  
170 age data for the post-salt interval (Figs. 3 and 4).

171 We mapped seven key seismic horizons and correlated these to stratigraphic information (e.g.  
172 age, lithology) provided by borehole 329D (Fig. 3). We chose horizons defining clear vertical  
173 changes in seismic facies, or which correlated to major lithological breaks or unconformities  
174 identified in boreholes. The key seismic horizons are of high-amplitude and are regionally  
175 mappable, whereas other horizons can only be locally interpreted within a few updip  
176 minibasins in the north of the study area (e.g.; intra-units 2, 3 and 4 horizons, Fig. 3). These  
177 seismic horizons were used to generate seismic isochron maps of key stratigraphic intervals  
178 that illustrate how syndepositional, salt-induced subsidence and uplift varied in space and  
179 time, and how this then impacted the development of deep-water depositional systems.

180 We use a range of volume- and surface-based seismic attributes to identify and map deep-  
181 water depositional elements (Table 3); i.e.; (i) *amplitude contrast*, which calculates amplitude  
182 derivatives between neighbouring seismic traces in order to highlight salt structures, faults

183 and mass transport complexes (Schlumberger, 2012); (ii) *variance*, which identifies abrupt  
184 lateral changes in seismic reflection continuity (Hart, 2008); and (iii) *sweetness*, which  
185 integrates amplitude strength (envelope) and instantaneous frequency to highlight lateral  
186 changes in seismic facies variations related to inferred changes in lithology (Hart, 2008). We  
187 visually blend sweetness and variance to identify and analyze seismic geomorphology of  
188 deep-water depositional elements (Fig. 3; see also Hart, 2008). By integrating seismic  
189 reflection and borehole data, we identify three main seismic facies (i.e., SF1-SF3; Fig. 3 and  
190 Table 2). The integration of map and section views with borehole derived lithology data was  
191 central to our interpretation of deep-water depositional elements along the slope.

192

#### 193 **4. Minibasin structure and stratigraphy**

194 Based on their location relative to the present shelf-edge, their map-view geometry, and the  
195 thickness of sediment they contain, we recognise three intraslope minibasin types: (i)  
196 *proximal thick minibasins* (e.g; minibasins A, B, C, D, E; Figs. 4a, b, c); (ii) *medial shallow*  
197 *minibasins* (e.g.; minibasins F, G, H; Figs. 4a, b, d); and (iii) *distal elongated minibasins* (e.g.;  
198 minibasins I, J, K, L, M; Figs. 4a, b, e). Seismic facies mapping and borehole-derived lithological  
199 data also indicate minibasin structure, bulk composition, and, therefore, likely depositional  
200 environment, vary in time and space (Fig 4). We define five key stratigraphic units based on  
201 vertical seismic facies variations within the minibasins (i.e., units 1-5; Figs. 3 and 4c-e). The  
202 approximate age of each unit is largely based on a tie to stratigraphic age information  
203 provided by boreholes 329D and 723C (Figs. 3 and 5b). Our age assignments are broadly  
204 consistent with, and are thus supported by, regional seismic and stratigraphic data presented

205 in several previous studies (e.g. Modica and Brush, 2004; Moreira et al. 2007; Contreras et al.,  
206 2010; Guerra and Underhill, 2012). In this section, we describe the structure and bulk  
207 stratigraphy of these minibasins, before outlining their tectono-stratigraphic development  
208 and the geomorphology of the deep-water depositional elements they contain.

209

#### 210 **4.1 Proximal thick minibasins:**

211 **Structure:** The updip, most proximal part of the study area, immediately seawards of the  
212 coeval shelf edge break, is characterized by relatively thick (> 2.5 km, 1.5 mi) minibasin-fill  
213 that are underlain by relatively thin (< 500 m, 1640 ft.) or apparently welded salt (e.g.;  
214 minibasins A-E; Figs. 4a, b, c; see also Jackson et al., 2014b). The minibasins trend N to NE, are  
215 up to 30 km (19 mi) long and 5 km (2.4 mi) wide, and are bound by similarly trending, upright  
216 salt walls that are up to 5 km (2.4 mi) wide. Internally, the bases of most minibasins are  
217 defined by 'bowl'-shaped packages (*sensu* Rowan and Weimer, 1998), which appear to record  
218 deposition of Unit 1 during simple vertical subsidence into underlying thick salt (Fig. 4c). Units  
219 2 and 3 within minibasins B, D and E were also deposited during simple vertical subsidence as  
220 suggested by the 'bowl-like' shape of the deepest seismic-stratigraphic units. In contrast,  
221 rather than being dominated by bowl-shaped packages, the middle and upper parts of some  
222 minibasins are defined by 'wedge'-shaped packages, suggesting the latter stages of  
223 subsidence were characterized by asymmetric subsidence and minibasin tilting (e.g.; units 2,  
224 3 and 4 in minibasins A, C; Fig. 4c).

225 We interpret that minibasin tilting occurred as salt was preferentially expelled from beneath  
226 one side of the subsidence depocentre. Differential salt evacuation, coupled with localised

227 welding, caused lateral migration of the earlier-formed depocenter from the minibasin centre  
228 to one of its margins (e.g., minibasins A and C, Fig. 4c; see Jackson and Cramez, 1989; Rowan  
229 and Weimer, 1998; Hudec et al., 2009; Jackson et al. 2014b). Our interpretation that minibasin  
230 welding led to asymmetric subsidence and the deposition of wedge-shaped packages is also  
231 supported by the local development of turtle-structure anticlines, which reflect structural  
232 inversion of minibasin stratigraphy (minibasin C, Fig. 4c; see Trusheim, 1960; Jackson and  
233 Cramez, 1989; Duval et al. 1992; Hudec et al., 2011; Jackson & Hudec, 2017).

234 **Stratigraphy:** A borehole penetrates the central, deepest part of a partly-enclosed proximal  
235 deep minibasin (minibasin C, Figs. 3, 4c). This borehole indicates the Unit 1 is dominated by  
236 interbedded Albian-Cenomanian marlstone and mudstone (c. 87%), with lesser proportions  
237 of coarser-grained carbonate (c. 12%) and clastics (c. 1%). In contrast, overlying units are  
238 relatively sandstone-rich (c. 45%), although very fine-grained lithologies (i.e. mudstone) still  
239 dominate (>50%; Unit 2 and Unit 3; Fig. 3). The unit capping the minibasins (i.e., Unit 5) is  
240 mudstone-dominated (Fig. 3).

241

## 242 **4.2 Medial shallow minibasins:**

243 **Structure:** The eastern, most distal part of the study area, which bounds the western flank  
244 of the Outer São Paulo Fold belt (*sensu* Jackson et al. 2015b), is characterized by minibasin-  
245 fill that are thinner (<1.5 km) than those further west (e.g., minibasins F, G, H; Figs. 4 a, b, d).  
246 The shallow minibasins are underlain by relatively thick salt (> 2 km) and welds are absent.  
247 The minibasins are sub-circular to oval in planform, are up to 20 km long and 10 km wide, and  
248 are enclosed by narrow (<2 km), nearly-triangular diapirs and salt-cored buckle folds (Fig. 4d).

249 The salt-cored structures bounding the shallow minibasins trend either NE or NW, thus  
250 defining a crude polygonal pattern (Fig. 4a, b). Internally, Units 1, 2 and 4 are characterized  
251 by negligible thickness variations along the shallow minibasins, although local bowl-shaped  
252 packages are suggestive of deposition during simple vertical subsidence into underlying thick  
253 salt (e.g., minibasin F; Fig. 4d). Instead, Unit 3 is defined by thin (<200 m) wedge-shaped  
254 packages indicating deposition during asymmetric subsidence (e.g., minibasins F, H; Fig. 4d).

255 **Stratigraphy:** A borehole penetrating a distal shallow minibasin indicates that Unit 1  
256 comprises only interbedded mudstone and marlstone (borehole 369A, Fig. 5a). Likewise, the  
257 overlying post-Cenomanian units (2-4) are also dominated (c. 80%) by very fine-grained  
258 lithologies (i.e. mudstone and marlstone). However, even in this relatively distal location,  
259 some sandstone (40 m net thickness) occurs within Unit 3 (i.e. borehole 369A, Figs. 4d, 5a).  
260 The unit capping the minibasins comprises only mudstone and marlstone (Unit 5, Fig. 5a).

261

### 262 **4.3 Distal minibasins:**

263 **Structure:** Downdip, in the most distal location of the study area includes part of the Inner  
264 São Paulo Plateau Fold Belt (ISPFB, *sensu* Jackson et al. 2015b). This area is characterized by  
265 north-south oriented minibasins that are up to 30 km long and 5 km wide. Strata within this  
266 minibasins are relatively thin (<1.5 km) and the minibasin-fill are typically underlain by  
267 relatively thick salt (c. 1 km; Fig. 4a, b). Some thicker (up to 2.5 km) minibasins overlying thin  
268 (<100 m) salt are also locally developed (e.g. minibasin M, eastern part of Fig. 4e). The distal  
269 minibasins are bound by salt walls that have flat or rugose-tops, or broadly N-trending, salt-  
270 cored anticlines (e.g., minibasins L, M, Fig. 4e; e.g., Jackson et al. 2014a, 2015b). The distal

271 minibasins are internally deformed by NE-trending, salt-cored buckle folds that are spaced  
272 approximately 5 km from one another (e.g, minibasins J and K, Fig. 4e). Internally, Unit 1 and  
273 Unit 2 are concordantly folded above the salt-cored buckle folds with local development of  
274 bowl-shaped packages characteristic of deposition during vertical minibasin subsidence (e.g.,  
275 minibasin M; Fig. 4e). In contrast, Unit 3 is of variable thickness, defining relatively thin (<200  
276 m), wedge- and bowl-shaped packages that overlie Unit 2 across an incision surface (Fig. 4e).  
277 Units 4 and 5 cap the distal minibasins and the flat-topped, bounding salt walls (Fig. 4e).

278 **Stratigraphy:** Most of the boreholes penetrating the Inner São Paulo Fold Belt and the distal  
279 minibasins indicate Unit 1 is comprised of interbedded mudstone and marlstone (Itanhaem  
280 Formation; boreholes 532A, 723C, 709, 594, Fig. 4a). However, a notable exception occurs on  
281 the eastern flank of minibasin K, where Unit 1 contain relatively coarse-grained lithologies  
282 (e.g. c. 63 m net thickness of siltstone and c. 22 m net thickness of sandstones; borehole 723C,  
283 Fig. 5b). The overlying post-Cenomanian units are also dominated by fine-grained lithologies  
284 (mudstone, c. 70% of total unit thickness), except on the eastern flank of minibasin K where  
285 relatively coarse-grained lithologies occur (i.e., siltstone, borehole 723C, 80% of total unit  
286 thickness, 170 m net thickness; Fig. 5b). Sandstone is rare (<5% of total unit thickness), with  
287 volumetrically minor proportions only locally developed (i.e. 723C, c. 27 m net thickness, Unit  
288 3, Fig. 5b). In a similar way to the more proximal minibasins, the unit capping the distal  
289 minibasins is mainly composed of mudstone (>81% of total unit thickness), although  
290 interbedded carbonate, sandstone and siltstone occur in its lower part (Fig. 5b)

291

## 292 **5. Deep-water depositional elements**

293 Having defined the key types and bulk lithological trends within the intraslope minibasins, we  
294 here integrate seismic stratigraphy and seismic attribute analysis to identify, describe and  
295 map the deep-water depositional elements they contain (Table 3). We identify five main  
296 seismic geomorphic elements, which we infer represent the following deep-water  
297 depositional elements; i) channels (with and without lateral accretion packages (LAPs); ii)  
298 levees; iii) lobes; iv) MTCs; and v) background deposits (Table 3).

299

### 300 ***Channels***

301 In cross-section, this depositional element is characterized by 20-150 m thick packages of  
302 parallel, continuous, flat-lying, moderate-to-high amplitude seismic reflections (Table 3).  
303 Package bases are flat and only weakly erosional (Table 3). In plan-view, these packages  
304 define relatively narrow (0.2-3 km), elongate (up to 200 km), low sinuosity (<1.5), channel  
305 forms that pass downdip into lobe-shaped depositional elements. We note these channel  
306 forms are defined by SF1, i.e., relatively high amplitudes, and high sweetness and low variance  
307 values, suggesting they are sandstone-prone (Table 2). This interpretation is supported by  
308 borehole 329D, which penetrates a channel feature and that indicates high-amplitude,  
309 continuous seismic facies correspond to the presence of sandstone (SF1; Fig. 5). Based on this  
310 observation and by comparison to other borehole-calibrated, seismic reflection-based studies  
311 (e.g. Prather et al. 1998; Samuel et al., 2003), we infer channel depositional elements defined  
312 by relatively moderate-to-low amplitudes are filled by finer-grained lithologies such as  
313 siltstone or mudstone.

314 Based on their seismic expression, geometry and scale, and by comparison to notable  
315 examples from other deep-water margins, this depositional element is interpreted as the  
316 seismic expression of turbidite-fed, relatively low-sinuosity, submarine channels (e.g. Gulf of  
317 Mexico, Prather et al., 1998, Prather 2003; Nile Delta, Samuel et al., 2003, Espirito Santo  
318 Basin; Alves et al., 2009; Lower Congo Basin, offshore Angola; Kolla et al. 2000; Mayall and  
319 Stewart; 2000; Fonnesu, 2003; Mayall and O'Byrne, 2002; Gee and Gawthorpe; 2006, 2007).

320 The inner bends of the relatively sinuous submarine channels (sinuosity index of at least 1.5)  
321 are characterized by up to 50 m thick, stacked packages of moderate-to-high-amplitude  
322 reflections that dip in towards the channel axis. Seismic attribute analysis indicates these  
323 crescent-shaped dipping reflections have a strike extent (i.e. parallel to the overall channel  
324 trend) of up to 1 km wide and dip extent (i.e. normal to the overall channel trend) of up to 5  
325 km (Table 3). Boreholes do not penetrate the dipping reflections, although their high  
326 amplitudes and high sweetness values suggest they are sandstone-dominated.

327 The inner bend dipping reflections could represent intra-channel terrace deposits (Deptuck  
328 et al., 2007; Hansen et al., 2017). Such deposits are however typically defined by flat-lying  
329 rather than dipping reflections, being cross-cut by inclined, more poorly imaged erosion  
330 surfaces that dip in towards the channel axis and which document relatively abrupt shifts in  
331 the channel position during net lateral migration (Hansen et al., 2017; Babonneau et al.,  
332 2010). An alternative interpretation is that the dipping reflections represent lateral accretion  
333 packages (LAPs) that developed due to lateral migration of the adjacent channel (cf. Kolla et  
334 al., 2000; Abreu et al. 2003; Janocko et al. 2013). This interpretation is consistent with the  
335 overall geometry of these features (i.e. inward dip towards the channel axis) and their  
336 development only on the inner bends of relatively sinuous channels. Although LAPs previously



337 reported at outcrop are significantly smaller, and more specifically thinner, than those  
338 documented here (e.g. up to 13 m thick in the lower Isaac Formation, British Colombia,  
339 Canada; Arnott, 2007; up to 4 m thick in the Rosario Formation of Baja California, Mexico;  
340 Dykstra & Kneller, 2009), our examples from the Santos Basin are comparable in scale to those  
341 described using 3D seismic reflection data from offshore west Africa (up to 40 m, Abreau et  
342 al. 2003; up to 50 m, Janocko et al. 2013).

343

#### 344 ***Levees***

345 Some of the submarine channels are locally flanked by wedge-shaped seismic packages of  
346 subparallel, low-to-moderate amplitude seismic reflections that are thickest (up to 150 m but  
347 typically thinner) immediately adjacent to the channels (Table 3). Due to the predominantly  
348 low-amplitude seismic reflections these elements are not clearly imaged by surface  
349 attributes. However, isochron maps indicate this depositional element is up to 5 km wide, up  
350 to 10 km long in dip extent, and are typically asymmetrically developed on both sides of the  
351 channel (isochron map on Table 3). None of the boreholes available penetrate this  
352 depositional element; however, these wedge-shaped seismic packages are characterized by  
353 low-to-moderate- amplitudes and sweetness values, suggesting they are composed of  
354 relatively fine-grained lithologies such as siltstone or mudstone.

355 Based on their seismic expression, geometry, scale and development adjacent to submarine  
356 channels, we interpret these depositional elements as levees, deposited by sediment gravity  
357 currents that escaped from their channels. Geometrically similar features are identified in  
358 many deep-water basins (e.g. Fonnesu, 2003; Viana et al., 2003; Gee and Gawthorpe, 2006,

359 2007; Clark and Cartwright, 2009, 2011; Janocko et al., 2013; Oluboyo et al., 2014; Ortiz-Karpf  
360 et al., 2015).

361

### 362 ***Lobes***

363 This depositional element is defined by tabular to mounded packages of subparallel,  
364 continuous, moderate-to-high-amplitude reflections. These packages are up to 10 km long, 5  
365 km wide and 200 m thick, thinning towards their fringes. Bidirectional downlap onto  
366 underlying strata is also observed in distal locations (Table 3). The plan-view morphology of  
367 this element ranges from sub-rounded, to lobate, to elongate occurring at the mouth of  
368 channel depositional elements (Table 3). Based on their high-amplitude character and  
369 moderate-to-high-sweetness values, we infer this depositional element is sandstone-  
370 dominated. This inference is supported by borehole data, which indicates some of the units  
371 containing these depositional elements are sandstone-bearing (Unit 2, Unit 3, 329D and Unit  
372 3 in 723C, 369A; Figs. 3, 5). Further support for a sandstone dominated composition comes  
373 from the mounded externally morphology of these features, which may reflect differential  
374 compaction between the lobes and adjacent finer-grained sediment.

375 Based on their geometry in map- and section-view, we interpret these depositional elements  
376 as lobes that occur at the mouth of and are genetically linked to updip submarine channels  
377 (cf. Gee and Gawthorpe, 2006, 2007; Saller et al., 2008; Prélat et al., 2010; Oluboyo et al.,  
378 2014; Doughty-Jones et al., 2017).

379

### 380 ***Mass-transport complexes (MTCs)***

381 This depositional element is characterized by up to 200 m thick, 50 km long packages of  
382 discontinuous to chaotic, low-to-moderate amplitude reflections (Table 3). The basal surface  
383 of this element is either sharp and apparently not erosional, or highly irregular and defined  
384 by 'v'-shaped grooves. The upper surfaces are invariably rugose. The plan-view morphologies  
385 of these elements are fan-shaped, defined by laterally extensive subparallel lineations or  
386 locally ponded within the minibasins (Table 3). Within these chaotic intervals we recognise  
387 laterally restricted 'blocks' of parallel, continuous moderate-to-high-amplitude reflectivity.  
388 These blocks are up to 100 m thick, 1 km long and 5 km wide.

389 Based on the seismic stratigraphy and geometry, we interpret these depositional elements as  
390 mass-transport complexes (MTCs). The chaotic seismic facies likely represent highly  
391 disaggregated, debritic material, whereas the coherent packages represent relatively  
392 coherent slide blocks (cf. Posamentier and Kola, 2003; Gee and Gawthorpe, 2006, 2007;  
393 Gamboa et al. 2010; Jones et al. 2012; Oluboyo et al. 2014).

394

### 395 ***Background deposits***

396 This depositional element dominates the stratigraphic fill of all minibasins, encasing the  
397 depositional elements described above. This depositional element is characterized by parallel,  
398 continuous, high-frequency, low-to-moderate amplitude reflections, although subtle  
399 variations in amplitude and sweetness occur (SF2; Tables 2 and 3). Borehole data indicate  
400 these seismic facies consists of fine-grained lithologies (i.e. mudstone and marlstone, e.g.,  
401 unit 5; Fig. 3). Based on the seismic stratigraphy and the integration with borehole data we

402 interpret this depositional element as fine-grained slope deposits emplaced by dilute turbidity  
403 currents or suspension setting (cf. Hadler-Jacobson et al. 2007; Oluboyo et al. 2014).

404

## 405 **6. Tectono-stratigraphic development of intraslope minibasins**

406 The key seismic stratigraphic units defined within the post-salt succession document the  
407 tectono-stratigraphic development of the intraslope minibasins in central deep-water Santos  
408 Basin (Fig. 4). Here, we interpret the isochron-derived thickness variations and depositional  
409 elements occurring within each unit; this allows us to understand minibasin filling history and,  
410 more specifically, to assess how syndepositional, salt-induced seafloor relief controlled deep-  
411 water sediment dispersal and sediment architecture. Based on previous regional studies (e.g.,  
412 Modica and Brush, 2004; Guerra and Underhill, 2012), we infer that the dominate sediment  
413 transport direction was from N-S and NW-SE, although we recognise local diversions from this  
414 within minibasins due to syndepositional deformation.

### 415 **6.1 Unit 1: Albian - Cenomanian**

416 The Unit 1 isochron indicates this unit is extensive and displays significant thickness variations  
417 (Figs. 6a). Overall, we observe a central thinner wedge or ‘tongue’ of relatively thin strata,  
418 which is surrounded by areas of thicker strata (up to 350 ms, TWT) (Fig. 6a). Seismic  
419 stratigraphic and attribute analysis provide no evidence for at least seismic-scale deep-water  
420 depositional systems within Unit 1.

421 Based on seismic reflection and borehole data (Fig. 5), we interpret that Unit 1 represents the  
422 distal expression of the Albian-Cenomanian carbonate platform (Fig. 4c-e, 5). Thickness

423 variations across the study area possibly reflects differences in the timing and style of salt  
424 tectonics (e.g., Jackson et al. 2015b).

425

## 426 **6.2 Unit 2: Turonian to Mid-Campanian**

427 Unit 2 is less extensive than Unit 1, with the main depocenters focused within proximal  
428 minibasins presently encircled by salt walls (minibasins A, C; Fig. 6b). Locally, a thick  
429 succession is observed, however, occurring landward of a salt roller within minibasin B  
430 (depocenter B1; Figs. 6b, 7a). In contrast, within the Inner Fold Belt and more distal  
431 minibasins, thinner successions occur (e.g. minibasins F-M; Fig. 6b).

432 In unit 2, deep-water depositional elements, such as channels and lobes, occur only within  
433 proximal thick minibasins (Fig. 7b). Low sinuosity (<1.5), narrow (<1 km wide) submarine  
434 channels enter from the north of, and are vertically stacked within, minibasin A (Fig. 7b).  
435 Channels of similar dimensions and sinuosities trend WNW in the proximal part of minibasin  
436 B and N in minibasin C, changing to NNE towards the south where they encounter the salt  
437 wall bounding the minibasins eastern margin (Fig. 7b). At the downdip mouths of some of the  
438 channels we identify lobes, with these being particularly well-developed within depocenter  
439 C1 where they correlate with SF1 in borehole 329D and are interpreted to be sandstone-rich  
440 (Fig. 7b; Table 2).

441 The distribution of deep-water sediments within Unit 2 was clearly controlled by salt-related  
442 deformation, with isochron, seismic attribute and borehole data indicating Turonian to Mid-  
443 Campanian, relatively coarse-grained channels only extended downdip into and were at least  
444 partly ponded within, proximal minibasins (minibasins A and northern part of minibasin B). In

445 addition, we interpret that channels within minibasin C are now separated from their updip  
446 counterparts in depocenter B1 by a large salt wall that pierces the stratigraphic interval within  
447 which they are developed (Fig. 7)

448

### 449 **6.3 Unit 3: Mid-Campanian to Paleocene**

450 Overall, Unit 3 is more extensive than Unit 2, with major intraslope depocenters still present  
451 in actively subsiding proximal minibasins (minibasins A-C; Fig. 6c). More specifically, local  
452 increases in sediment thickness occur next to intra-minibasin salt rollers and thin-skinned  
453 normal faults, and along minibasin flanks associated with growing salt walls (Figs. 8a, b; 9).  
454 However, in contrast to Unit 2, significant thicknesses of strata are now preserved in downdip  
455 minibasins, especially in synclines flanking folds, above salt-cored faults, and along minibasin  
456 flanks (minibasins D-M; Fig. 6c).

457 Deep-water depositional systems are widespread in unit 3 (Figs. 8 c-e; 9c). Minibasins A-C are  
458 still dominated by relatively low sinuosity (<1.5), narrow (<1 km wide) submarine channels.  
459 However, these channels extend further downdip than those in Unit 2. For example, channels  
460 in minibasin A are no longer restricted to the northern part of the depocenter, now extending  
461 c. 10 km further south to the junction between minibasins A and B, where they appear to pass  
462 downslope into a lobe (Figs. 8c,d). Likewise, channels and lobes initially ponded in  
463 depocenters B1-B2 extend further downslope along minibasin B, depositing lobes in  
464 depocenter B3 (Fig. 8d). Some of the channels entering minibasin B in Unit 3 extend  
465 downslope towards minibasin C, although channels along the western flank of the minibasin  
466 appear to be diverted towards depocenter B3 at their southern end (Figs. 8d; 9 a,b). During

467 deposition of unit 3, lobes are also deposited against the salt wall bounding the SE margin of  
468 the minibasin (depocenters C2, Figs. 8d; 9c). Continued filling of minibasin C was accompanied  
469 by the shifting of depocenters C2 to C3 related to deposition of SE-trending submarine  
470 channels, which apparently terminate abruptly against the salt wall defining the southern  
471 limit of minibasin C; however, further downslope, on the other side of this structure, channels  
472 of similar dimensions, orientation and morphology occur in minibasin D and E (Figs. 8e; 9d).

473 In distal regions, N-trending, slightly sinuous channels occur within and trend parallel to the  
474 long axes of several broadly N-trending minibasins (channels 1, 2 and 3 in minibasins I-K; Fig.  
475 10). Channels that trend at a relatively high angle ( $>30^\circ$ ) to bounding salt walls and salt-cored  
476 anticlines change course within the minibasins, becoming parallel to the minibasin axis and  
477 bounding salt walls (channels 4, 5; Fig. 10). Locally, channel bends also occur next to salt-  
478 cored folds, in some cases leading to the deposition of LAPs (channel 2; Figs. 10, 11a,b). Within  
479 distal minibasins, lobes are confined to minibasin flanks and within fold-bounded synclines,  
480 downlapping onto the lows and onlapping and converging towards salt-cored highs (Figs. 12a-  
481 f).

482 Channel continuity between adjacent minibasins across bounding salt walls is observed  
483 downslope in distal minibasins (e.g. channel 5 across minibasins L and M; Fig. 10). However,  
484 changes in channel geometry are evident between, for example, minibasin L to M. In  
485 minibasin L, we identify an erosional channel, up to 1 km wide and, 50 m thick (Fig. 10, 13).  
486 The channel trends NW and is flanked by levees and overlying an intra-minibasin MTC  
487 (channel 5 in Figs. 13 a-d). Within minibasin M, this channel increases in reflectively, width (to  
488 5 km) and thickness (to 200 m), in addition to bending to trend NE, sub-parallel to the

489 minibasin axis (Figs. 13a,b,e). The asymmetric levees flanking channel 5 onlap onto and are  
490 seemingly rotated on the limbs of, the western salt-cored anticline (Fig. 14).

491 During deposition of Unit 3, the locus of subsidence in minibasin A shifted towards the center  
492 and eastern margin of the depocenter possibly due to welding (depocenters A1 to A3; Figs.  
493 8b-d). In addition, the cessation of activity on landward-dipping listric faults at the northern  
494 updip end of minibasin B meant that channels were able to spill southwards and flow axially  
495 along minibasin B (depocenters B1 to B3; Figs. 8b,d and 9a,b). Continued deposition drove  
496 welding of minibasin C and shifting of the main depocenter within minibasin C, leading to  
497 eventual inversion of the minibasin stratigraphy and the formation of a turtle anticline  
498 (depocenters C2 to C3; Figs. 8a,b and 9c). Eventual filling of minibasin C resulted in sediment  
499 spilling downslope to the SE into minibasin D and E (Figs. 8e, 9d). Based on similar trends and  
500 morphology, we suggest channels presently contained in minibasins D and E, and now  
501 separated by a large diapir, were previously part of a through-going, continuous system that  
502 extended across the diapir (Figs. 8e, 9d). Likewise, we suggest that at least the northern part  
503 of the salt wall currently dividing minibasins B and C did not represent a barrier to channels  
504 flowing between these depocenters, but that subsequent growth of the diapir initially  
505 underlying the channels, subsequently dissected these depositional systems (Figs. 8c,d).  
506 Furthermore, we interpret that channels flowing across the ISPFB and the distal minibasins  
507 probably spilled over from proximal minibasins west of minibasin A, which are not imaged in  
508 the seismic dataset. Towards the distal minibasins, structurally-induced changes in channel  
509 sinuosity occurred due to coeval salt-cored highs on the paleoseafloor (Figs. 10-14). LAPs are  
510 only developed when channels are unconfined or only weakly confined, recording lateral  
511 channel migration to towards the minibasin centers (Figs. 10,11). In addition, levees and lobes



512 are deposited confined within minibasins or in the intra-minibasin fold- and thrust-bounded  
513 synclines associated with shortening of salt and its overburden (Fig. 12-14).

514

#### 515 **6.4 Unit 4: Paleocene to Mid-Oligocene**

516 Deposition within Unit 4 extends further east than in unit 3 (Fig. 6d). Thickness changes in  
517 Unit 4 indicate proximal thick minibasins were still actively subsiding, although deposition was  
518 now also occurring above bounding salt walls (e.g., minibasin D; Fig. 6d).

519 Rather than containing relatively abundant channel-levee systems and lobes like units 2 and  
520 3, Unit 4, more specifically sub-units 4a and 4b within the proximal thick minibasins, are  
521 dominated by MTCs (Figs. 9a,b and 15a). MTCs within unit 4a contain relatively angular  
522 megaclasts that are up to 5 km long and 1 km wide overlying sub-continuous to chaotic  
523 seismic facies (Fig. 9b). In contrast, MTC blocks within unit 4b are less angular and smaller (1  
524 km long by 500 m wide; Figs. 9a,b; 15b). In the Inner Fold Belt and within the downdip  
525 elongated minibasins, at least 200 km long, N- and NW-trending linear, sub-parallel grooves  
526 are developed along a single seismic event at the base of unit 4 (Fig. 16). These grooves are  
527 overlain by blocks that are smaller (200 m long by 100 m wide) than those observed in the  
528 proximal thick minibasins (section A-A' in Fig. 16).

529 During deposition of Unit 4, some of the proximal and distal minibasins continue to actively  
530 subside into salt (Fig. 6d). However, unit 4 marks a significant change in the style of clastic  
531 sediment deposition within the basin. More specifically, we see a cessation of coarse-grained  
532 clastic deposition within channels and lobes, and the initiation of widespread MTC  
533 emplacement (Fig. 15). It is not possible to constrain the source of MTCs contained within the

534 proximal thick minibasins, and it is thus unknown if they were derived from collapse of the  
535 distal shelf-edge or slope, or if they were locally sourced from the uplifted and rotated  
536 minibasin margins flanking the bounding diapirs. However, thrusts within unit 4a within the  
537 proximal minibasins may indicate MTCs were sourced from the NE (Fig. 9a). In contrast, the  
538 regionally extensive grooves capping the distal minibasins and ISPFB suggest MTC  
539 emplacement from the NNW (Fig. 16).

540

## 541 **6.5 Unit 5: Mid-Oligocene to Pleistocene**

542 Unit 5 is more extensive than underlying units, with the main minibasin depocenters still  
543 occurring in the NW of the study area (e.g., minibasin D; Fig. 6e). We identify at least three  
544 MTC-bearing sub-intervals within Unit 5, all of which are contained within a single minibasin  
545 in the W of the study area (Figs. 6e; 17). In contrast to the regionally developed, Paleocene  
546 MTC identified within Unit 3, these younger MTCs are confined by salt-cored diapirs. The  
547 lowermost MTCs are dominated by highly chaotic seismic facies and lack megaclasts, whereas  
548 the shallower MTC contains abundant megaclasts within a chaotic matrix (Fig. 17; see also  
549 Jackson et al., 2011).

550 Because these MTCs extend to the NW outside of the seismic dataset, their source is  
551 unknown. However, regional considerations suggest they were sourced from large shelf-edge  
552 and slope failures north or north-west of the study area (Contreras et al., 2010; Jackson,  
553 2011). Therefore, Unit 5 records Neogene emplacement of several MTCs in response to  
554 repeated collapse of the north-western basin margin shelf-edge and/or slope.

555

556

## 557 **7. Discussion**

558 We used 3D seismic reflection and borehole data to illustrate the spatial and temporal  
559 variations in the size and type of salt-influenced deep-water depositional systems, Santos  
560 Basin, offshore Brazil. We here discuss regional salt-tectonic controls on minibasin  
561 development, and the key local controls on paleo-seafloor relief and how this influenced  
562 deep-water stratigraphic architecture.

563

### 564 **7.1. Salt-related controls on the tectono-stratigraphic evolution of** 565 **the Santos Basin**

566 We show that the initial phase (Turonian to Mid Campanian; unit 2) of coarse clastic  
567 deposition was restricted to the north, with submarine channels and lobes confined within  
568 proximal minibasin depocenters (minibasins A and C, Fig. 7 a, b). Intra-minibasin relief was  
569 generated by salt diapirs and landward-dipping, salt-detached listric faults (Fig. 9 a, b). The  
570 main phase of clastic deposition occurred during the Maastrichtian to Paleocene (unit 3),  
571 during which time salt- and fault-related accommodation in the proximal minibasins was filled  
572 or 'healed', allowing deep-water sediment to bypass the now-filled proximal minibasins and  
573 to be deposited further downslope (minibasins C, D and E; Figs. 8e 9). Furthermore, eventual  
574 welding of proximal led to the formation of a turtle anticline and a lateral shift of the related  
575 depocenters from the minibasin centre towards the immediate flanks of the bounding diapirs  
576 (minibasin C, Fig. 8b, 9c). During the third and final phase of clastic deposition (unit 4;

577 Paleocene to mid-Oligocene), MTCs dominated, being sourced from either the flanks of  
578 intraslope minibasins, or the shelf-edge and/or slope. Channels and lobes are very rare in this  
579 stratigraphic interval, suggesting a regionally significant change in sediment supply occurred  
580 between the Paleocene (late Unit 3) and Eocene (early Unit 4) (Figs. 15, 16). This abrupt  
581 change in deep-water deposition may have been driven by river capture and diversion of  
582 sediment supply towards the northern Santos and the Campos Basin, a process that has been  
583 attributed to the uplift of the onshore coastal mountain range (e.g. Cobbold et al. 2001).  
584 Localised salt flow and minibasin subsidence continued during a fifth and final phase (unit 5;  
585 mid-Oligocene to present-day). Deposition at this time was dominated by suspension settling  
586 of relatively fine-grained deposits, although MTCs provide evidence for continued failure of  
587 the shelf-edge and/or slope (Fig. 17).

588 Previous regional studies in the Santos Basin assume that most coarse clastic sediment was  
589 trapped behind a large (4 km thick, 200 km long, 10 km wide), salt-controlled, intra-slope  
590 depocenter (i.e., the Albian Gap; e.g. Ge et al., 1997; Modica and Brush, 2004; Guerra and  
591 Underhill, 2012; Jackson et al., 2015a). However, our study provides conclusive evidence that  
592 relatively coarse-grained deep-water depositional elements were deposited up to 200 km  
593 from the Late Cretaceous shelf margin, clearly indicating that not all coarse-grained sediment  
594 was trapped landward of the Albian Gap (cf. Modica and Brush, 2004; Guerra and Underhill,  
595 2012).

## 596 **7.2. Beyond the ‘fill and spill’ model**

597 The two initial phases of sediment deposition, first in proximal locations (Unit 2) and then  
598 reaching further downslope along a healed slope (Unit 3), indicate progressive basinward

599 filling or 'healing' of this salt-influenced slope (Fig 18). The stratigraphic development of the  
600 deep-water central Santos Basin thus displays many of the characteristics captured in the 'fill  
601 and spill' model (e.g. Winker, 1996; Prather et al., 1998). Furthermore, our results show that  
602 spilling between minibasins tends to occur in locations where salt-cored structures trend  
603 perpendicular to sediment transport, with long-distance confinement characterising locations  
604 where salt walls are oriented parallel or at a low angle to sediment transport (e.g., Booth et  
605 al., 2003; Oluboyo et al., 2014). More specifically, we document local sediment spilling due to  
606 minibasin welding and the associated formation of turtle anticlines; these two processes  
607 together cause diversion of deep-water channels towards the downslope minibasin (e.g.; Fig.  
608 8b, Fig 18).

609 A key result of this work is that post-depositional growth of salt diapirs can cause dissection  
610 of previously through-going depositional systems, resulting in 'pseudo-onlap' onto the diapir  
611 flanks (e.g., salt wall between D and E, Figs. 8e, 9d, 18). This process has perhaps been  
612 overlooked in previous studies focusing on relatively young (i.e. Neogene-Quaternary), near-  
613 seabed stratigraphy because in these cases, despite being influenced by syn-depositional salt  
614 movement, the deposition systems of interest presently still overlie or occur on the flanks of  
615 large salt bodies (e.g. Pirmez et al., 2000; Fonnesu, 2003; Gee and Gawthorpe, 2006, 2007).  
616 This highlights an important, perhaps ignored aspect of the fill-and-spill model, namely that  
617 the depositional substrate, be it salt or mudstone, is not static (e.g. Winker, 1996; Prather et  
618 al., 1998); instead, this substrate is highly mobile, with related structures continuing to grow  
619 post-deposition of any one stratigraphic interval. This has obvious implications for the  
620 formation of hydrocarbon traps (see below).

621 Finally, this study illustrates that the pattern of minibasin filling is influenced by the formation  
622 and growth of intra-minibasin salt-cored faults and salt rollers (Fig. 8 a; 9 a,b; 18). More  
623 specifically, growing intra-minibasin structures can lead to somewhat counterintuitive  
624 depositional patterns; for example, deepwater systems may be diverted away from proximal  
625 minibasins, meaning that distal minibasins are filled first, contrary to the classical ‘fill and spill’  
626 model (Fig 18; e.g. Booth et al., 2003; Hudec et al., 2009; Jackson et al., 2010; Albertão et al.,  
627 2011; Oluboyo et al., 2014).

628

### 629 **7.3. Impact of salt-induced seafloor relief on reservoir distribution** 630 **and architecture**

631 Having discussed the regional controls on basin-scale deep-water stratigraphic architecture,  
632 we now consider the local controls on syndepositional seafloor relief and sediment dispersal  
633 and architecture. In addition, we discuss the implications of our findings for the overall salt-  
634 tectonic evolution of the Santos Basin. Local seafloor relief can lead to lateral confinement,  
635 frontal confinement or blocking), deflection and diversion of deep-water depositional  
636 systems; thus, directly impacting reservoir distribution and architecture along slopes (e.g.  
637 Booth et al., 2003; Adeogba et al., 2005; Gee and Gawthorpe, 2006; Deptuck et al., 2007;  
638 Clark and Cartwright 2009; Hubbard et al., 2009; Callec et al., 2010; Mayall et al., 2010;  
639 Oluboyo et al., 2014; Sychala et al., 2017; Doughty-Jones et al., 2017).

640 In the salt-influenced Santos Basin, we observe the following end-member styles of salt-  
641 sediment interaction: (i) local *diversion* of channels by pre-existing seafloor relief, which also  
642 results in a change in channel sinuosity (e.g., Figs. 13, 18) (cf. Oluboyo et al., 2014, Doughty-

643 Jones et al., 2017); (ii) *deflection* of channels towards syn-depositional structural lows, leading  
644 to channel lateral migration from and stacking adjacent to, emerging salt-cored highs (e.g.,  
645 Figs. 11a, 12, 18); (iii) *confinement* of channels by adjacent salt-cored highs resulting in  
646 channel stacking and levee growth, and lobe deposition in parts of the system that are  
647 frontally confined (e.g., Figs. 12); (iv) *blocking* of channels by intra-minibasin salt rollers and  
648 salt-detached faults, preventing deposition downslope (e.g.; Figs. 7, 8, 18) (cf. Clark and  
649 Cartwright 2009; 2011). Two key questions we address below are; (i) were salt-cored highs  
650 static or actively growing *during* the entire life-cycle of the depositional elements?; and (ii)  
651 did the structures continue to grow *after* the channels and lobes were deposited?

652 Local channel *deflection* is evident in the south of the study area, occurring next to emerging  
653 shortening-related, salt-cored buckle folds and thrust-cored folds (Figs. 10; 11a; 12; 18).  
654 Likewise, channel *diversion* also occurs to in the south of the study area, next to a salt wall  
655 (minibasin M, Fig. 13), as well as within the proximal minibasins (minibasins B, C, Fig. 8 d). The  
656 salt-cored highs next to which channel *deflection* and *diversion* are observed are oriented  
657 nearly-perpendicular to the depositional slope. The structurally-induced sinuous geometry of  
658 the channels adjacent to these highs clearly suggest the latter grew *before* Late  
659 Maastrichtian/Paleocene submarine channels propagated downslope and across the São  
660 Paulo Plateau. Syndepositional growth of salt-cored highs is supported by the following  
661 evidence: (i) onlap and thinning towards the coeval highs (Figs. 12, 14); (ii) local  
662 stacking/ponding in the thrust-cored syncline (minibasin J; Figs. 12e, 18); and (iii) uplift, tilting  
663 and rotation of levee towards the channel axis (sensu Clark and Cartwright, 2009; minibasin  
664 M; Fig. 14). Salt structure growth may have also continued *after* deposition, as indicated by  
665 the channel tilting and uplift (Fig. 14).

666 Our data provide evidence for channel *blocking* and *confinement* (e.g., within proximal  
667 minibasins B, Figs. 9 a,b; 18). For example, channels and lobes initially confined north of  
668 minibasin B (depocenters B1, B2) or diverted towards minibasin C, eventually extended along  
669 minibasin B before being frontally confined against a salt wall at the southern end of the  
670 minibasin (depocenters B3; Fig. 8d). We suggest local increases in accommodation during  
671 minibasin confinement leads to: (i) an increase in channel width and thickness along the  
672 minibasin axis, with a corresponding increase in seismic amplitude also suggesting a  
673 downslope increase in sandstone deposition (e.g., Fig. 14) (cf. Gee and Gawthorpe, 2006); (ii)  
674 preferential deposition of levees where accommodation locally increases (minibasins L, M,  
675 Figs. 13, 14); (iii) preferential deposition of (confined) lobes (and healing of syn-depositional  
676 relief) in synclines between intra-minibasin salt-cored anticlines (Figs. 12, 18). We suggest  
677 syndimentary growth of the salt-cored structures bounding the folded minibasins in the  
678 contractional domain provided confined accommodation, causing channels to aggrade and  
679 triggering deposition of related levees and lobes.

680 These observations have implications for the salt-related structural evolution of the central  
681 deep-water Santos Basin. We propose that the seafloor salt-cored folds were the expression  
682 of Late Cretaceous-to-Paleocene, syndimentary, thin-skinned shortening, resulting from  
683 downslope flow of salt and its overburden, possibly related to the formation of the Albian  
684 Gap (Jackson et al. 2015a; Pichel et al. 2018). The distribution and architecture of  
685 synkinematic channels and levees systems provide a stratigraphic record of this structural  
686 growth (Fig. 18).

687



## 688 **7.4 Exploration significance**

689 We propose that the salt-related controls observed in the central deep-water Santos Basin  
690 led to changes in the geometry, distribution and potential structural and stratigraphic  
691 trapping of reservoir-prone units. As such, post-salt sequences in this part of the Santos Basin  
692 may be prospective (see Fainstein et al., 2001). In particular, we have illustrated the presence  
693 of: (i) fault-block traps (e.g., Figs. 9 a,b); (ii) turtle anticlines (minibasin C, Fig. 9 c); (iii)  
694 stratigraphic traps related to the pinch-out of channels and lobes towards salt-cored highs  
695 (e.g., Figs. 9 a,b; 14). Potential reservoir-prone units include channel-fill, lobes and, possibly,  
696 levees, whereas 'background' deposits, such as slope mudstone, and salt represent the main  
697 seals (Table 3). Mudstone-rich MTCs may also form lateral and vertical seals (e.g., minibasin  
698 L, Fig. 15). The seismic stratigraphic geometry and distribution of the more proximal reservoir-  
699 prone intervals of stacked submarine channels and fans or sheet-sand reservoirs illustrated  
700 in this study are strikingly similar to reservoir-prone units being currently produced in the Gulf  
701 of Mexico (i.e., Auger Basin, Booth et al., 2003; Jackson and Hudec, 2017; Fig. 9 a, b).

702 The deep-water depositional systems we have identified in the Santos Basin could be distal  
703 analogues of the unconfined turbidites in the Merluza (Turonian) (e.g., Enciso and Tisi, 1998),  
704 and Roncador fields (Campanian-Maastrichtian), Campos Basin (e.g., Bruhn et al., 2003;  
705 Hongquan et al., 2018). Unlike those further north, the distal deep-water depositional  
706 systems in the Santos Basin have been confined axially for more than 150 km and because of  
707 this confinement, it is possible the associated reservoirs are thicker than those developed in  
708 the Campos Basin (cf. Gulf of Mexico; e.g., Booth et al., 2003). Furthermore, the play fairway,  
709 in terms of reservoir distribution, will likely be narrower due to syn-depositional confinement  
710 of the deep-water depositional systems. A key exploration risk for the whole Santos Basin is

711 migration, principally due to the presence of thick, likely very low-permeability salt between  
712 sub-salt source rocks and supra-salt reservoirs. This is a particular risk in distal areas, where  
713 thick allochthonous salt remains, whereas in proximal areas salt welds may facilitate the  
714 vertical migration of hydrocarbon. Even if hydrocarbons migrate through weld, the  
715 mudstone-dominated nature of many of the minibasin may still pose a migration risk.

716 Shallowly buried MTCs may represent drilling hazards due to unpredictable pore pressures  
717 and hole conditions. In addition, syn-emplacement erosion at the base of salt diapir-flank  
718 MTCs may have locally removed underlying submarine channel reservoirs and compromise  
719 reservoir continuity (e.g., minibasin K; Fig. 13c).

720

## 721 **8 Conclusions**

722 Our 3D seismic reflection and borehole-based analysis illustrates a long timescale (ca. 60  
723 Myrs) record of salt-sediment interaction in more than ten minibasins covering an area of c.  
724 20,122 km<sup>2</sup>; thus, documents the post-salt tectonostratigraphic evolution of the central deep-  
725 water Santos Basin from the initial minibasin development in the Turonian up to present-day:

726 1. Overall, we recognise three minibasin types, from proximal updip to distal  
727 location downdip; i.e. (i) proximal thick minibasins, apparently welded, (ii) medial shallow  
728 minibasins, overlying thick salt, and (iii) distal elongated minibasins deformed by shortening-  
729 related folds and thrusts

730                   2. Four main types of deep-water sediment depositional elements were  
731 deposited within the minibasins in central deep-water Santos Basin: channels, levees, lobes,  
732 MTCs and background deposits.

733                   3. Borehole information indicates that the minibasin-confined channel-levee  
734 systems are composed of interbedded sandstone, siltstone and mudstone. Whereas distal  
735 boreholes suggest siltstone rich channel-fill and lobes.

736                   4. Sedimentation in central deep-water Santos Basin occurred during three main  
737 phases of minibasin subsidence:

738                   • Phase I: Turonian to the Mid-Campanian: sand-rich channel systems and lobes  
739 were confined within proximal updip minibasins and to the hangingwalls of landward-dipping,  
740 salt-detached listric faults.

741                   • Phase II-Mid-Campanian to the Paleocene: sand-rich channels and lobes  
742 eventually filled and bypassed proximal updip minibasins, with coarse clastic deposition then  
743 occurring further downslope in distal minibasins, >100 km from the coeval shelf margin.

744                   • Phase III and IV: Paleocene-to-middle Oligocene: continued rise of proximal  
745 salt walls dissected previously deposited deep-water systems, with deposition from diapir-  
746 and shelf-edge sourced MTCs becoming increasingly important

747                   5. Syndepositional seafloor relief, driven by passive and active diapirism, and salt-  
748 detached thrusting and folding, caused changes in the geometry, architecture and  
749 distribution of deep-water depositional systems:

750                   i)       channel deflection and diversion around salt-cored highs

- 751           ii)     channel and levee uplift and rotation on the flanks of rising salt-cored  
752                   anticlines and diapirs
- 753           iii)    progressive lateral channel migration, expressed in the form of lateral  
754                   accretion packages (LAPs)
- 755           iv)     Lateral and frontal confinement of channel, levees and lobes.
- 756           v)     channel width and thickness increase due to lateral confinement

757           6. The deep-water depositional elements identified have important implications  
758 for post-salt hydrocarbon prospectivity in the central, deep-water Santos Basin, with a range  
759 of reservoir types and trapping styles being developed in this previously underexplored  
760 interval

## 761 **ACKNOWLEDGEMENTS**

762 We would like to thank CGG for providing access to the 3D seismic data and for granting  
763 permission to publish the results of this study. We also thank Statoil and ANP Brazil for  
764 providing access to the borehole data. Schlumberger WesternGeco is also gratefully  
765 acknowledged for providing 2D seismic regional data, partial funding and support of this work.  
766 We thank reviewers David Hodgson, Jory Pacht and Ian Clark and editor Barry Katz for their  
767 suggestions which have significantly improved the quality of this manuscript. We also  
768 acknowledge Rachelle Kernan for her insightful suggestions.

769

## 770 **FIGURE CAPTIONS**

771 **FIGURE 1:** (a) Offshore Brazil sedimentary basins; (b) Santos Basin topography and  
772 bathymetry map highlighting the location of study area and dataset. 3D seismic reflection

773 data courtesy of CGG and public Brazilian boreholes; (c) Geoseismic profile across the study  
774 area based on interpretation of 2D seismic data courtesy of WesternGeco, Schlumberger. See  
775 location in b; (d) Seismic stratigraphic framework. After Modica and Brush (2004); Moreira et  
776 al. (2007); Jackson (2012).

777 **FIGURE 2:** Central deepwater Santos Basin paleogeography highlighting sedimentation  
778 trapped or ponded landwards of the Albian Gap with limited deposition in the area of study.  
779 Modified after Modica and Brush, 2004. (a) Late Campanian paleogeography; (b) Middle  
780 Eocene paleogeography; (c) Late Eocene paleogeography.

781 **FIGURE 3:** Intra-minibasin seismic-well correlation. Key seismic horizons and units are  
782 indicated and defining a turtle anticline due to inversion of the minibasin stratigraphy.  
783 Seismic attributes response highlights vertical variations in seismic facies within the  
784 minibasin. See also Table 2 for a description of SF1, SF2, and SF3. Dominant frequency and  
785 vertical seismic resolution decreases with depth, as indicated in the last three columns and in  
786 Table 1. Borehole location is shown in Figure 4a

787 **FIGURE 4:** 4a) Postsalt isopach (Seabed to top salt depth thickness map) illustrating sediment  
788 thickness variations across the study area. Depth thickness map estimated using the depth-  
789 converted seafloor depth structural map and the top salt structural map also in depth. 4b)  
790 Top salt structural map illustrating the main minibasin types in the study area. Proximal  
791 minibasins (A-E); shallow minibasins (F-H) and distal elongated minibasins (I-M). 4c)  
792 Geoseismic profile across the proximal thick minibasins A to E. 4d) Geoseismic profile across  
793 shallow minibasins F-H. 4e) Geoseismic profile across part of the inner fold belt and across  
794 some of the distal elongated minibasins (K-M). See Figure 4b for location of geoseismic  
795 profiles.

796 **FIGURE 5:** Intra-minibasin seismic-well tie showing the presence of reservoir-prone  
797 sandstones in distal locations, i.e., > 50 km from the coeval shelf margin. (a) Borehole 369a  
798 penetrates a medial shallow minibasin. See Figure 4a for location. (b) Borehole 723C  
799 penetrates the flank of a downdip distal minibasin. See Figure 4a for location.

800 **FIGURE 6:** Regional isochrons illustrating deposition and salt-related deformation in the post-  
801 salt of central deep-water Santos Basin. 6a) Albian-Cenomanian unit 1 twt thickness map; 6b)  
802 Turonian to Mid-Campanian Unit 2 twt thickness map; 6c) Mid-Campanian to Paleocene Unit  
803 3 twt thickness map; 6d) Paleocene to Mid Oligocene Unit 4 twt thickness map; 6e) Mid-  
804 Oligocene to present-day Unit 5 twt thickness map.

805 **FIGURE 7:** Detailed thickness maps and attributes of the proximal minibasins (A-C) illustrating  
806 local intra-minibasins depocenters and shifting of depocenters during minibasin  
807 development. (a) Unit 2 thickness map highlighting initial depocenters A1, B1 and C1 within  
808 updip proximal minibasins A, B and C. Present-day Top Salt is shown in pink. (b) Unit 2b  
809 seismic attributes blending (interval is shown on section in Figure 9c). Present-day Top Salt  
810 structure map is shown in pink. Attributes visually blended correspond to Variance and  
811 Sweetness (described in the Methods section). Purple colours correspond to more  
812 transparent background facies. Yellow to red colours highlight deep-water depositional  
813 elements interpreted in the accompanying map. Depocenters A1, B1 and C1 are interpreted  
814 based on thickness map in Figure 7a.

815

816 **FIGURE 8:** Detailed thickness maps and attributes of the proximal minibasins (A-C) illustrating  
817 local intra-minibasins depocenters and shifting of depocenters during minibasin

818 development. Visually blended seismic attributes correspond to Variance and Sweetness  
819 described in the Methods section. Purple and dark blue colours correspond to more  
820 transparent background facies. Yellow to red colours highlight deep-water depositional  
821 systems interpreted in the accompanying map. Depocenters are interpreted based on the  
822 isochrons. (a) Proximal thick minibasins - Sub-Unit 3a isochron highlighting shifting of  
823 depocenters A1, B1, C1 (Fig. 7a) to new depocenters A2, B2 and C2. Present-day Top Salt is  
824 shown in pink. (b) Proximal thick minibasins - Sub-Unit 3b isochron highlighting shifting of  
825 depocenters A2, B2 and C2 (Fig 8a) to new depocenters A3, B3 and C3. (c) Sub-unit 3a seismic  
826 attributes blending and interpretation. Sub-unit 3a is shown on sections in Figures 9a, b and  
827 c. (Fig. 8a). (d) Sub-unit 3b seismic attributes blending and interpretation. Sub-unit 3b is  
828 shown on sections in Figures 9a, b and c. (e) Unit 3b sweetness and variance attribute visual  
829 blending illustrating the post-depositional dissection of submarine clastic systems caused by  
830 the rise of the salt wall presently bounding minibasins B and C, C and D and D and E.

831 **FIGURE 9:** Seismic profiles along and across the updip/proximal minibasins illustrating the key  
832 horizons and units mapped and the thickness and seismic facies variations defining the  
833 minibasin stratigraphy. Highly-reflective intervals correspond to interpreted depositional  
834 elements highlighted with seismic attributes in Figure 8. The locations of the seismic sections  
835 are also shown on Figure 8. (a) Seismic section along Minibasin B. Insets illustrate potential  
836 sandstone-rich depositional elements with an amplitude- and frequency-based seismic  
837 attribute (Sweetness). (b) Laterally and frontally confined deep-water depositional elements  
838 along minibasin B based on seismic stratigraphic interpretation and seismic attribute analysis.  
839 (c) Seismic profile across Minibasin C illustrating the main units interpreted. Initial  
840 confinement is illustrated by thinning and onlapping of minibasin stratigraphy towards the

841   downdip (SE) salt wall (units 2a, 2b and 3a). Minibasin filling and welding led to inversion of  
842   the minibasin stratigraphy (units 2a, 2b, and 3a), and spilling and shifting of the initial  
843   depocenters from Minibasin B towards the SE and downdip minibasins (units 3b and 4). See  
844   location of seismic profile in Figure 8

845   **FIGURE 10:** Deep-water depositional systems and distal downdip minibasins (I, M) in the Inner  
846   São Paulo Fold Belt and the São Paulo Plateau. Updip, channel systems are relatively linear  
847   and unconfined. Local variations in architecture are controlled by salt-cored folds and  
848   anticlines and salt walls. Lateral and frontal confinements is observed downdip. See area  
849   location in Figure 6c. Interpretation is based on seismic stratigraphy, geomorphology, seismic  
850   attributes and thickness maps. Detailed isochrons, attribute maps, and seismic sections are  
851   shown in Figures 11-14.

852   **FIGURE 11:** (a) Sweetness and variance blending illustrating local increase in channel sinuosity  
853   and lateral accretion packages described in Table 3. See channel 2 location and associated  
854   structural elements in Figure 10. (b) Seismic section illustrating channel bend and high-  
855   amplitude lateral accretion packages. See Figure 11a for location of seismic section.

856   **FIGURE 12:** Isochron (a) and seismic attribute blending (b) for unit 3 covering minibasins I and  
857   J illustrating salt-related controls on coeval deep-water depositional systems. Increase in  
858   thickness occurs around salt-cored folds and associated to lobes deposition where frontally  
859   confined. Deflection of submarine channel 2 (ch2) occurs around a salt-cored fold in Minibasin  
860   J and this is highlighted in the amplitude contrast attribute in the inset. See interpretation and  
861   location in Figure 10. (c) and (d): Seismic sections across the distal part of minibasin I,  
862   illustrating lobes deposition and confinement. (e) and (f) Seismic sections across and along



863 minibasin J. illustrating salt-related controls on deposition. Location of seismic sections are  
864 highlighted in Figures 12 a and b

865 **FIGURE 13:** Isochron (a) and seismic attribute blending (b) for unit 3 covering minibasin L and  
866 M illustrating deep-water submarine channels across present-day minibasins and salt-related  
867 controls. Channel 5 (ch5) is oriented SE and relatively thinner along Minibasin L but gets  
868 diverted and laterally confined and wider along Minibasin M due to the bounding salt-wall  
869 oriented nearly-perpendicular to the slope. See location and interpretation in Figure 10. (c) A  
870 local MTC underlies submarine channel 5 within Minibasin L. Seismic sections in (d) and (e)  
871 highlight bounding salt walls and salt-cored anticline, channel 5 and associated levees in  
872 minibasins L and M. See location of seismic sections in Figures 13 a and b.

873 **FIGURE 14:** Submarine channel and levee geometry variations along Minibasin M. Isochron  
874 and section A-A' illustrate wing-shaped levees developed adjacent to the channel. Seismic  
875 attribute and sections illustrate that high-amplitudes are restricted to the channel axis,  
876 whereas the levees are characterized by medium to low amplitudes. Channel onlaps and its  
877 apparently tilted and rotated where it gets diverted and closer to the bounding salt wall  
878 (section B-B'). Intra-levee reflections are rotated towards the channel axis (sections C-C' and  
879 D-D') indicating salt movement during deposition

880 **FIGURE 15:** Seismic attributes sweetness and variance blending and interpretation of intra-  
881 minibasin clasts characterizing MTCs in proximal updip minibasins during deposition of Unit  
882 4. See location of minibasins A, B and C in regional map Figure 6c and seismic and geoseismic  
883 sections in Figures 9a and 9b.

884 **FIGURE 16:** Seismic attributes and seismic sections illustrating linear grooves characterizing  
885 regional-scale MTCs across the São Paulo inner fold-belt and the São Paulo plateau and  
886 highlighting a drastic change in the evolution of the central deep-water Santos Basin during  
887 deposition of Unit 4. See location of minibasins J, K, L, and M in regional map in Figure 6c.

888 **FIGURE 17:** Seismic expression of MTCs within Unit 5. a) Amplitude contrast attribute of intra-  
889 Unit 5 horizon highlighting clasts and a chaotic matrix; b) seismic section across the minibasin;  
890 c) seismic section along the minibasin.

891 **FIGURE 18:** a) Block diagram summarizing sedimentation within proximal minibasins: Ponding occurs  
892 within proximal, updip, intra-minibasin depocenters prior to spilling and deposition along the  
893 minibasins (1). Filling of minibasins and subsequent welding of minibasin floor led to spilling towards  
894 downdip minibasins (2). Channel systems are post-depositionally dissected by rising salt walls  
895 bounding the present-day minibasins (3). Subsequent spilling from updip depocenters and diversion  
896 by rising salt walls led to deposition in downdip depocenters (4). b) Block diagram summarizing salt-  
897 related controls in deep-water sedimentation across part of the São Paulo inner fold-belt and the  
898 distal minibasins in the São Paulo plateau. Channel systems spilling from the proximal  
899 minibasins are relatively linear updip and away from salt-cored structures (1). Local controls  
900 in channel system architecture (2) and sediment distribution (3) are observed. Present-day  
901 salt walls dissected channel systems similarly to what it is observed in the updip minibasins  
902 (4). The architecture of channel systems varies between adjacent minibasins controlled by  
903 the presence of intra-minibasin MTCs and confinement (5 and 6).

#### 904 **TABLE CAPTIONS**

905 **Table 1:** Vertical seismic resolution of key intervals in different structural domains

906 **Table 2:** Table 2: Seismic facies interpretation and seismic attributes calibration with lithology from  
907 borehole 329D, minibasin C. See Figure 4a for location

908 **Table 3:** Seismic facies and depositional elements identified within the post-salt in central  
909 deep-water Santos Basin. Depositional elements are defined based on the integration of  
910 seismic stratigraphy and seismic geomorphology.

911

912

### 913 REFERENCES

914 Abreu, V., M. Sullivan, C. Pirmez, and D. Mohrig, 2003, Lateral accretion packages (LAPs): an  
915 important reservoir element in deep water sinuous channels: *Marine and Petroleum*  
916 *Geology*, v. 20, p. 631-648.

917 Adeogba, A.A., McHargue, T.R. and Graham, S.A., 2005. Transient fan architecture and  
918 depositional controls from near-surface 3-D seismic data, Niger Delta continental  
919 slope. *AAPG bulletin*, 89(5), pp.627-643.

920 Albertão, G. A., T. Mulder, and R. Eschard, 2011, Impact of salt-related palaeotopography on  
921 the distribution of turbidite reservoirs: Evidence from well-seismic analyzes and  
922 structural restorations in the Brazilian offshore: *Marine and Petroleum Geology*, v. 28,  
923 p. 1023-1046.

924 Alves, T. M., J. Cartwright, and R. J. Davies, 2009, Faulting of salt-withdrawal basins during  
925 early halokinesis: Effects on the Paleogene Rio Doce Canyon system (Espírito Santo  
926 Basin, Brazil): *AAPG Bulletin*, v. 93, p. 617-652.

927 Anderson, J. E., J. Cartwright, S. J. Drysdall, and N. Vivian, 2000, Controls on turbidite sand  
928 deposition during gravity-driven extension of a passive margin: examples from  
929 Miocene sediments in Block 4, Angola: *Marine and Petroleum Geology*, v. 17, p. 1165-  
930 1203.

- 931 Argent, J.D., Stewart, S.A. and Underhill, J.R., 2000. Controls on the Lower Cretaceous Punt  
932 Sandstone Member, a massive deep-water clastic deposystem, Inner Moray Firth, UK  
933 North Sea. *Petroleum Geoscience*, 6(3), pp.275-285.
- 934 Arnott, R.W.C., 2007. Stratal architecture and origin of lateral accretion deposits (LADs) and  
935 conterminuous inner-bank levee deposits in a base-of-slope sinuous channel, lower  
936 Isaac Formation (Neoproterozoic), East-Central British Columbia, Canada. *Marine and  
937 Petroleum Geology*, 24(6-9), pp.515-528.
- 938 Bacocoli, G., R. G. Morales, and P. J. M. De Castro, 1979, Oil Exploration in Campos Basin,  
939 Brazil; Model for Exploration in Atlantic-Type Basins: ABSTRACT, 412-412 p.
- 940 Bacocoli, G., R. G. Morales, and O. A. Campos, 1980, The Namorado oil field: A major oil  
941 discovery in the Campos basin, Brazil.
- 942 Badalini, G., Kneller, B. and Winker, C.D., 2000, Architecture and processes in the late  
943 Pleistocene Brazos-Trinity turbidite system, Gulf of Mexico continental slope. In *Deep-  
944 Water Reservoirs of the World: SEPM, Gulf Coast Section, 20th Annual Research  
945 Conference*, pp. 16-34.
- 946 Beaubouef, R.T. and Friedmann, S.J., 2000, December. High resolution seismic/sequence  
947 stratigraphic framework for the evolution of Pleistocene intra slope basins, western  
948 Gulf of Mexico: depositional models and reservoir analogs. In *Deep-water reservoirs  
949 of the world: Gulf Coast Section SEPM 20th Annual Research Conference* (pp. 40-60).
- 950 Babonneau, N., Savoye, B., Cremer, M. and Bez, M., 2010. Sedimentary architecture in  
951 meanders of a submarine channel: detailed study of the present Congo turbidite  
952 channel (Zaiango project). *Journal of Sedimentary Research*, 80(10), pp.852-866.
- 953 Booth, J. R., M. C. Dean, A. E. DuVernay, and M. J. Styzen, 2003, Paleo-bathymetric controls  
954 on the stratigraphic architecture and reservoir development of confined fans in the  
955 Auger Basin: central Gulf of Mexico slope: *Marine and Petroleum Geology*, v. 20, p.  
956 563-586.
- 957 Broucke, O., F. Temple, D. Rouby, C. Robin, S. Calassou, T. Nalpas, and F. Guillocheau, 2004,  
958 The role of deformation processes on the geometry of mud-dominated turbiditic  
959 systems, Oligocene and Lower–Middle Miocene of the Lower Congo basin (West  
960 African Margin): *Marine and Petroleum Geology*, v. 21, p. 327-348.

- 961 Bruhn, C. H., and R. G. Walker, 1995, High-resolution stratigraphy and sedimentary evolution  
962 of coarse-grained canyon-filling turbidites from the Upper Cretaceous transgressive  
963 megasequence, Campos Basin, offshore Brazil: *Journal of Sedimentary Research*, v. 65.
- 964 Bruhn, C. H., J. A. T. Gomes, C. Del Lucchese Jr, and P. R. Johann, 2003, Campos basin:  
965 reservoir characterization and management-Historical overview and future  
966 challenges: *Offshore Technology Conference*.
- 967 Brun, J.-P., and X. Fort, 2004, Compressional salt tectonics (Angolan margin): *Tectonophysics*,  
968 v. 382, p. 129-150.
- 969 Callec, Y., Deville, E., Desaubliaux, G., Griboulard, R., Huyghe, P., Mascle, A., Mascle, G., Noble,  
970 M., Padron de Carillo, C. and Schmitz, J., 2010. The Orinoco turbidite system: Tectonic  
971 controls on sea-floor morphology and sedimentation. *AAPG bulletin*, 94(6), pp.869-  
972 887.
- 973 Candido, A., and C. A. Cora, 1992, The Marlstoneim and Albacora Giant Fields, Campos Basin,  
974 Offshore Brazil: Chapter 8.
- 975 Clark, I. R., and J. A. Cartwright, 2009, Interactions between submarine channel systems and  
976 deformation in deep-water fold belts: Examples from the Levant Basin, Eastern  
977 Mediterranean Sea: *Marine and Petroleum Geology*, v. 26, p. 1465-1482.
- 978 Clark, I. R., and J. A. Cartwright, 2011, Key controls on submarine channel development in  
979 structurally active settings: *Marine and Petroleum Geology*, v. 28, p. 1333-1349.
- 980 Cobbold, P. R., K. E. Meisling, and V. S. Mount, 2001, Reactivation of an Obliquely Rifted  
981 Margin, Campos and Santos Basins, Southeastern Brazil: *AAPG Bulletin*, v. 85, p. 1925-  
982 1944.
- 983 Contreras, J., R. Zühlke, S. Bowman, and T. Bechstädt, 2010, Seismic stratigraphy and  
984 subsidence analysis of the southern Brazilian margin (Campos, Santos and Pelotas  
985 basins): *Marine and Petroleum Geology*, v. 27, p. 1952-1980.
- 986 Davison, I., 2007, *Geology and tectonics of the South Atlantic Brazilian salt basins*: Geological  
987 Society, London, Special Publications, v. 272, p. 345-359.
- 988 Davison, I., L. Anderson, and P. Nuttall, 2012, Salt deposition, loading and gravity drainage in  
989 the Campos and Santos salt basins: Geological Society, London, Special Publications,  
990 v. 363, p. 159-174.

- 991 Deptuck, M.E., Sylvester, Z., Pirmez, C. and O'Byrne, C., 2007. Migration–aggradation history  
992 and 3-D seismic geomorphology of submarine channels in the Pleistocene Benin-major  
993 Canyon, western Niger Delta slope. *Marine and Petroleum Geology*, 24(6-9), pp.406-  
994 433.
- 995 De Gasperi, A., and O. Catuneanu, 2014, Sequence stratigraphy of the Eocene turbidite  
996 reservoirs in Albacora field, Campos Basin, offshore Brazil: *AAPG bulletin*, v. 98, p. 279-  
997 313.
- 998 Doughty-Jones, G., Mayall, M. and Lonergan, L., 2017. Stratigraphy, facies and evolution of  
999 deep-water lobe complexes within a salt-controlled intra-slope minibasin. *AAPG*  
1000 *Bulletin*, (20,170,215).
- 1001 Duval, B., Cramez, C. and Jackson, M.P.A., 1992. Raft tectonics in the Kwanza basin, Angola.  
1002 *Marine and Petroleum Geology*, 9(4), pp.389-404.
- 1003 Dykstra, M. and Kneller, B., 2009. Lateral accretion in a deep-marine channel complex:  
1004 implications for channellized flow processes in turbidity  
1005 currents. *Sedimentology*, 56(5), pp.1411-1432.
- 1006 Fainstein, R., Jamieson, G., Hannan, A., Biles, N., Krueger, A. and Shelander, D., 2001, October.  
1007 Offshore Brazil Santos Basin exploration potential from recently acquired seismic data.  
1008 In 7th International Congress of the Brazilian Geophysical Society.
- 1009 Fiduk, J. C., and M. G. Rowan, 2012, Analysis of folding and deformation within layered  
1010 evaporites in Blocks BM-S-8 & -9, Santos Basin, Brazil: Geological Society, London,  
1011 Special Publications, v. 363, p. 471-487.
- 1012 Figueiredo, A., M. Pereira, W. Mohriak, P. Gaglianone, and L. Trindade, 1985, Salt Tectonics  
1013 and Oil Accumulation in Campos Basin, Offshore Brazil: ABSTRACT: *AAPG Bulletin*, v.  
1014 69, p. 255-255.
- 1015 Fonnesu, F., 2003, 3D seismic images of a low-sinuosity slope channel and related  
1016 depositional lobe (West Africa deep-offshore): *Marine and Petroleum Geology*, v. 20,  
1017 p. 615-629.
- 1018 Fort, X., J.-P. Brun, and F. Chauvel, 2004, Salt tectonics on the Angolan margin,  
1019 synsedimentary deformation processes: *AAPG Bulletin*, v. 88, p. 1523-1544.

- 1020 Gamboa, D., T. Alves, J. Cartwright, and P. Terrinha, 2010, MTD distribution on a  
1021 'passive' continental margin: the Espírito Santo Basin (SE Brazil) during the Palaeogene:  
1022 Marine and Petroleum Geology, v. 27, p. 1311-1324.
- 1023 Gambôa, L. A. P., M. A. P. Machado, D. P. Silveira, J. T. R. De Freitas, and S. R. P. Da Silva, 2008,  
1024 Evaporitos estratificados no Atlantico Sul: Interpretacao sismica e controle tectono-  
1025 estratigrafico na Bacia de Santos.: In Mohriak, W., Szatmari, P. & Anjos, S.M.C. Sal:  
1026 Geologia e Tectonica, Exemplos nas Basicas Brasileiras., v. Beca Edicoes Ltda, Sao  
1027 Paulo, Brasil, p. 340-359.
- 1028 Ge, H., Jackson, M.P. and Vendeville, B.C., 1997. Kinematics and dynamics of salt tectonics  
1029 driven by progradation. AAPG bulletin, 81(3), pp.398-423.
- 1030 Gee, M., and R. Gawthorpe, 2006, Submarine channels controlled by salt tectonics: Examples  
1031 from 3D seismic data offshore Angola: Marine and Petroleum Geology, v. 23, p. 443-  
1032 458.
- 1033 Gee, M., and R. Gawthorpe, 2007, Early evolution of submarine channels offshore Angola  
1034 revealed by three-dimensional seismic data: Geological Society, London, Special  
1035 Publications, v. 277, p. 223-235.
- 1036 Gee, M., R. Gawthorpe, and S. Friedmann, 2006, Triggering and evolution of a giant submarine  
1037 landslide, offshore Angola, revealed by 3D seismic stratigraphy and geomorphology:  
1038 Journal of Sedimentary Research, v. 76, p. 9-19.
- 1039 Giles, K. A., and M. G. Rowan, 2012, Concepts in halokinetic-sequence deformation and  
1040 stratigraphy: Geological Society, London, Special Publications, v. 363, p. 7-31.
- 1041 Goteti, R., S. J. Ings, and C. Beaumont, 2012, Development of salt minibasins initiated by  
1042 sedimentary topographic relief: Earth and Planetary Science Letters, v. 339, p. 103-  
1043 116.
- 1044 Guardado, L. R., L. A. Gamboa, and C. F. Lucchesi, 1989, Petroleum Geology of the Campos  
1045 Basin, Brazil, a Model for a producing atlantic type basin: part 1. Guardado, L., A.  
1046 Spadini, J. Brandão, and M. Mello, 2000, AAPG Memoir 73, Chapter 22: Petroleum  
1047 System of the Campos Basin, Brazil.
- 1048 Guerra, M. C. M., and J. R. Underhill, 2012, Role of halokinesis in controlling structural styles  
1049 and sediment dispersal in the Santos Basin, offshore Brazil: Geological Society,  
1050 London, Special Publications, v. 363, p. 175-206.

- 1051 Hadler-Jacobsen, F., M. H. Gardner, and J. M. Borer, 2007, Seismic stratigraphic and  
1052 geomorphic analysis of deep-marine deposition along the West African continental  
1053 margin: Geological Society, London, Special Publications, v. 277, p. 47-84.
- 1054 Hansen, L., Janocko, M., Kane, I. and Kneller, B., 2017. Submarine channel evolution, terrace  
1055 development, and preservation of intra-channel thin-bedded turbidites: Mahin and  
1056 Avon channels, offshore Nigeria. *Marine Geology*, 383, pp.146-167.
- 1057 Hart, B., 2008, Stratigraphically significant attributes: The Leading Edge, v. 27, p. 320-324.
- 1058 Hearon IV, T. E., M. G. Rowan, K. A. Giles, and W. H. Hart, 2014, Halokinetic deformation  
1059 adjacent to the deep-water Auger diapir, Garden Banks 470, northern Gulf of Mexico:  
1060 Testing the applicability of an outcrop-based model using subsurface data:  
1061 Interpretation, v. 2, p. SM57-SM76.
- 1062 Hongquan, K.A.N.G., Jinluo, M.E.N.G., Cheng, T., Huaicun, J.I.A., Bo, B.A.I. and Minggang, L.I.,  
1063 2018. Characteristics of deep water depositional system in Campos basin, Brazil.  
1064 *Petroleum Exploration and Development*, 45(1), pp.99-110.
- 1065 Horschutz, P. M. C., L. Freitas, C. V. Stank, A. d. S. Barroso, W. Cruz, and M. Halbouty, 1978,  
1066 The Linguado, Carapeba, Vermelho and Marimbá Giant Fields, Campos Basin, Offshore  
1067 Brazil: Giant oil and gas fields of the decade, v. 1988, p. 137-153.
- 1068 Hubbard, S.M., de Ruig, M.J. and Graham, S.A., 2009. Confined channel-levee complex  
1069 development in an elongate depo-center: deep-water Tertiary strata of the Austrian  
1070 Molasse basin. *Marine and Petroleum Geology*, 26(1), pp.85-112.
- 1071 Hudec, M. R., M. P. Jackson, and D. D. Schultz-Ela, 2005, A Compressional Origin for Minibasins  
1072 near the Sigsbee Scarp, Gulf of Mexico.
- 1073 Hudec, M. R., and M. P. A. Jackson, 2007, Terra infirma: Understanding salt tectonics: Earth-  
1074 Science Reviews, v. 82, p. 1-28.
- 1075 Hudec, M. R., M. P. A. Jackson, and D. D. Schultz-Ela, 2009, The paradox of minibasin  
1076 subsidence into salt: Clues to the evolution of crustal basins: Geological Society of  
1077 America Bulletin, v. 121, p. 201-221.
- 1078 Jackson, C.A., Kane, K.E. and Larsen, E., 2010. Structural evolution of minibasins on the Utsira  
1079 High, northern North Sea; implications for Jurassic sediment dispersal and reservoir  
1080 distribution. *Petroleum Geoscience*, 16(2), pp.105-120.



- 1081 Jackson, C. A.-L., M. P. Jackson, and M. R. Hudec, 2015a, Understanding the kinematics of salt-  
1082 bearing passive margins: A critical test of competing hypotheses for the origin of the  
1083 Albian Gap, Santos Basin, offshore Brazil: Geological Society of America Bulletin, v.  
1084 127, p. 1730-1751.
- 1085 Jackson, C. A.-L., M. P. A. Jackson, M. R. Hudec, and C. Rodriguez, 2014 (a), Internal structure,  
1086 kinematics, and growth of a salt wall: Insights from 3-D seismic data: *Geology*, v. 42,  
1087 p. 307-310.
- 1088 Jackson, C. A.-L., K. E. Kane, and E. Larsen, 2010, Structural evolution of minibasins on the  
1089 Utsira High, northern North Sea; implications for Jurassic sediment dispersal and  
1090 reservoir distribution: *Petroleum Geoscience*, v. 16, p. 105-120.
- 1091 Jackson, C.A., 2011, Three-dimensional seismic analysis of megaclast deformation within a  
1092 mass transport deposit; implications for debris flow kinematics. *Geology*, 39(3),  
1093 pp.203-206.
- 1094 Jackson, C. A. L., 2012, The initiation of submarine slope failure and the emplacement of mass  
1095 transport complexes in salt-related minibasins: A three-dimensional seismic-reflection  
1096 case study from the Santos Basin, offshore Brazil: Geological Society of America  
1097 Bulletin, v. 124, p. 746-761.
- 1098 Jackson, C. A. L., M. P. A. Jackson, M. R. Hudec, and C. R. Rodriguez, 2015b, Enigmatic  
1099 structures within salt walls of the Santos Basin—Part 1: Geometry and kinematics from  
1100 3D seismic reflection and well data: *Journal of Structural Geology*, v. 75, p. 135-162.
- 1101 Jackson, C.A.L., Rodriguez, C.R., Rotevatn, A. and Bell, R.E., 2014 (b). Geological and  
1102 geophysical expression of a primary salt weld: An example from the Santos Basin,  
1103 Brazil. *Interpretation*, 2(4), pp.SM77-SM89.
- 1104 Jackson, M.P.A. and Cramez, C., 1989, December. Seismic recognition of salt welds in salt  
1105 tectonics regimes. In *Gulf of Mexico salt tectonics, associated processes and*  
1106 *exploration potential: Gulf Coast Section SEPM Foundation 10th Annual Research*  
1107 *Conference* (pp. 66-71).
- 1108 Jackson, M.P. and Hudec, M.R., 2017. *Salt Tectonics: Principles and Practice*. Cambridge  
1109 University Press.
- 1110 Jackson, M., and C. J. Talbot, 1991, *A glossary of salt tectonics*, Bureau of Economic Geology,  
1111 University of Texas at Austin.

- 1112 Janocko, M., W. Nemeč, S. Henriksen, and M. Warchoř, 2013, The diversity of deep-water  
1113 sinuous channel belts and slope valley-fill complexes: *Marine and Petroleum Geology*,  
1114 v. 41, p. 7-34.
- 1115 Jones, G., M. Mayall, and L. Lonergan, 2012, Contrasting depositional styles on a slope system  
1116 and their control by salt tectonics: through-going channels, ponded fans, and mass  
1117 transport complexes: Rosen, NC, Weimer, P., Coutes dos Anjos SM, Henrickson, S.,  
1118 Marques, E., Mayall, M., Fillon, p. 40-60.
- 1119 Karner, G. D., and L. A. P. Gambôa, 2007, Timing and origin of the South Atlantic pre-salt sag  
1120 basins and their capping evaporites: Geological Society, London, Special Publications,  
1121 v. 285, p. 15-35.
- 1122 Kolla, V., and J. Urruty, 2000, Ph. Bourges 'Evolution of a deep-water Tertiary sinuous channel  
1123 offshore Angola (Africa) and implications to reservoir architecture': *AAPG Bulletin*, p.  
1124 1373.
- 1125 Lin, C., Liu, J., Eriksson, K., Yang, H., Cai, Z., Li, H., Yang, Z. and Rui, Z., 2014. Late Ordovician,  
1126 deep-water gravity-flow deposits, palaeogeography and tectonic setting, Tarim Basin,  
1127 Northwest China. *Basin Research*, 26(2), pp.297-319.
- 1128 Lopes, M., C. Bruhn, R. Santos, C. Corá, M. Becker, R. Alves, and D. Sarzenski, 1999,  
1129 Architecture of Sand-Rich, Turbidite Reservoirs from Deep Water Campos Basin,  
1130 Brazil: 1999 AAPG Conference & Exhibition, San Antonio, Texas.
- 1131 Macedo, J., L. A. P. Gamboa, J. A. Ricci, L. F. G. Caddah, and W. Winter, 1998, Stratigraphic  
1132 comparisons between the post-rift section of the Campos and Santos Basins,  
1133 Southeast Brazilian margin: Extended Abstracts, AAPG: ABGP/AAPG International  
1134 Conference and Exhibition, Rio de Janeiro.
- 1135 Machado, L. C. R., R. O. Kowsmann, W. Almeida-Jr, C. Y. Murakami, S. Schreiner, D. J. Miller,  
1136 and P. Piauilino, 2004, Geometria da porção proximal do sistema deposicional  
1137 turbidítico moderno da Formação Carapebus, Bacia de Campos: modelo para  
1138 heterogeneidades de reservatório: *Boletim de Geociências da Petrobras*, v. 12, p. 287-  
1139 315.
- 1140 Mayall, M., and I. Stewart, 2000, The architecture of turbidite slope channels: Deep-Water  
1141 Reservoirs of the World: SEPM, Gulf Coast Section, 20th Annual Research Conference,  
1142 p. 586.

- 1143 Mayall, M. and O'Byrne, C., 2002, January. Reservoir prediction and development challenges  
1144 in turbidite slope channels. In *Offshore Technology Conference*. Offshore Technology  
1145 Conference.
- 1146 Mayall, M., L. Lonergan, A. Bowman, S. James, K. Mills, T. Primmer, D. Pope, L. Rogers, and R.  
1147 Skeene, 2010, The response of turbidite slope channels to growth-induced seafloor  
1148 topography: AAPG bulletin, v. 94, p. 1011-1030.
- 1149 McArthur, A.D., Claussmann, B., Bailleul, J., McCaffrey, W. and Clare, A., 2019. Variation in  
1150 syn-subduction sedimentation patterns from inner to outer portions of deep-water  
1151 fold and thrust belts: examples from the Hikurangi subduction margin of New Zealand.  
1152 Geological Society, London, Special Publications, 490, pp.SP490-2018.
- 1153 Meisling, K. E., P. R. Cobbold, and V. S. Mount, 2001, Segmentation of an Obliquely Rifted  
1154 Margin, Campos and Santos Basins, Southeastern Brazil: AAPG Bulletin, v. 85, p. 1903-  
1155 1924.
- 1156 Modica, C. J., and E. R. Brush, 2004, Postrift sequence stratigraphy, paleogeography, and fill  
1157 history of the deep-water Santos Basin, offshore southeast Brazil: AAPG Bulletin, v.  
1158 88, p. 923-945.
- 1159 Mohriak, W., M. Mello, J. Dewey, and J. Maxwell, 1990, Petroleum geology of the Campos  
1160 Basin, offshore Brazil: Geological Society, London, Special Publications, v. 50, p. 119-  
1161 141.
- 1162 Moraes, M. A., 1989, Diagenetic evolution of Cretaceous-Tertiary turbidite reservoirs,  
1163 Campos Basin, Brazil: AAPG Bulletin, v. 73, p. 598-612.
- 1164 Moraes, M. A., P. R. Blaskovski, and P. Joseph, 2004, The Grès d'Annot as an analogue for  
1165 Brazilian Cretaceous sandstone reservoirs: comparing convergent to passive-margin  
1166 confined turbidites: Geological Society, London, Special Publications, v. 221, p. 419-  
1167 437.
- 1168 Moreira, J. L. P., C. Madeira, J. A. Gil, and M. A. P. Machado, 2007, Bacia de Santos: Bulletin  
1169 Geociencias Petrobras, v. 15, p. 531-549.
- 1170 Morley, C.K., 2003. Mobile shale related deformation in large deltas developed on passive  
1171 and active margins. Geological Society, London, Special Publications, 216(1), pp.335-  
1172 357.

- 1173 Oluboyo, A., R. Gawthorpe, K. Bakke, and F. Hadler-Jacobsen, 2014, Salt tectonic controls on  
1174 deep-water turbidite depositional systems: Miocene, southwestern Lower Congo  
1175 Basin, offshore Angola: *Basin Research*, v. 26, p. 597-620.
- 1176 Ortiz-Karppf, A., Hodgson, D.M. and McCaffrey, W.D., 2015. The role of mass-transport  
1177 complexes in controlling channel avulsion and the subsequent sediment dispersal  
1178 patterns on an active margin: the Magdalena Fan, offshore Colombia. *Marine and*  
1179 *Petroleum Geology*, 64, pp.58-75.
- 1180 Pessoa, J., C. C. Martins, J. Heinerici, R. J. Jahnert, A. B. França, L. Trindade, and C. Francisco,  
1181 1999, *Petroleum System And Seismic Expression In The Campos Basin: 6th*  
1182 *International Congress of the Brazilian Geophysical Society*.
- 1183 Pichel, L.M., Jackson, C.A.L., Peel, F. and Dooley, T., 2018. Effects of Pre-salt Relief on Salt  
1184 Tectonics on the S o Paulo Plateau and Implications for the Albian Gap.
- 1185 Pirmez, C., Beaubouef, R.T., Friedmann, S.J., Mohrig, D.C. and Weimer, P., 2000, December.  
1186 Equilibrium profile and baselevel in submarine channels: examples from Late  
1187 Pleistocene systems and implications for the architecture of deepwater reservoirs. In  
1188 *Global deep-water reservoirs: Gulf Coast Section SEPM Foundation 20th Annual Bob*  
1189 *F. Perkins Research Conference* (pp. 782-805).
- 1190 Posamentier, H. W., and V. Kolla, 2003, Seismic geomorphology and stratigraphy of  
1191 depositional elements in deep-water settings: *Journal of Sedimentary Research*, v. 73,  
1192 p. 367-388.
- 1193 Prather, B.E., 2003. Controls on reservoir distribution, architecture and stratigraphic trapping  
1194 in slope settings. *Marine and Petroleum Geology*, 20(6-8), pp.529-545.
- 1195 Prather, B.E., Booth, J.R., Steffens, G.S. and Craig, P.A., 1998. Classification, lithologic  
1196 calibration, and stratigraphic succession of seismic facies of intraslope basins, deep-  
1197 water Gulf of Mexico. *AAPG bulletin*, 82(5), pp.701-728.
- 1198 Prélat, A., Covault, J.A., Hodgson, D.M., Fildani, A. and Flint, S.S., 2010. Intrinsic controls on  
1199 the range of volumes, morphologies, and dimensions of submarine lobes.  
1200 *Sedimentary Geology*, 232(1), pp.66-76.
- 1201 Rodriguez, C.R., Jackson, C.L., Rotevatn, A., Bell, R.E. and Francis, M., 2018. Dual tectonic-  
1202 climatic controls on salt giant deposition in the Santos Basin, offshore Brazil.  
1203 *Geosphere*, 14(1), pp.215-242.

- 1204 Rowan, M. G., F. J. Peel, and B. C. Vendeville, 2004, Gravity-driven fold belts on passive  
1205 margins, in K. R. McClay, ed., Thrust tectonics and hydrocarbon systems: AAPG  
1206 Memoir 82, p.157-182.
- 1207 Rowan, M.G. and Weimer, P., 1998, Salt-sediment interaction, northern Green Canyon and  
1208 Ewing bank (offshore Louisiana), northern Gulf of Mexico. AAPG bulletin, 82(5),  
1209 pp.1055-1082.
- 1210 Saller, A., Werner, K., Sugiawan, F., Cebastian, A., May, R., Glenn, D. and Barker, C., 2008.  
1211 Characteristics of Pleistocene deep-water fan lobes and their application to an upper  
1212 Miocene reservoir model, offshore East Kalimantan, Indonesia. AAPG bulletin, 92(7),  
1213 pp.919-949.
- 1214 Schlumberger, 2012, Interpreter's guide to seismic attribute, 4<sup>th</sup> edition, p. 112-114.
- 1215 Sinclair, H.D. and Tomasso, M., 2002, Depositional evolution of confined turbidite basins.  
1216 Journal of Sedimentary Research, 72(4), pp.451-456.
- 1217 Spychala, Y.T., Hodgson, D.M., Flint, S.S. and Mountney, N.P., 2015. Constraining the  
1218 sedimentology and stratigraphy of submarine intraslope lobe deposits using exhumed  
1219 examples from the Karoo Basin, South Africa. Sedimentary Geology, 322, pp.67-81.
- 1220 Spychala, Y.T., Hodgson, D.M., Stevenson, C.J. and Flint, S.S., 2017. Aggradational lobe fringes:  
1221 The influence of subtle intrabasinal seabed topography on sediment gravity flow  
1222 processes and lobe stacking patterns. Sedimentology, 64(2), pp.582-608.
- 1223 Stewart, S. A., 2007, Salt tectonics in the North Sea Basin: a structural style template for  
1224 seismic interpreters: Geological Society, London, Special Publications, v. 272, p. 361-  
1225 396.
- 1226 Stewart, S. A., and J. A. Clark, 1999, Impact of salt on the structure of the Central North Sea  
1227 hydrocarbon fairways: Geological Society, London, Petroleum Geology Conference  
1228 series, v. 5, p. 179-200.
- 1229 Sylvester, Z., Cantelli, A. and Pirmez, C., 2015. Stratigraphic evolution of intraslope minibasins:  
1230 Insights from surface-based model. AAPG Bulletin, 99(6), pp.1099-1129.
- 1231 Trusheim, F., 1960. Mechanism of salt migration in northern Germany. AAPG Bulletin, 44(9),  
1232 pp.1519-1540.

- 1233 Viana, A., Figueiredo, A., Faugeres, J.C., Lima, A., Gonthier, E., Brehme, I. and Zaragosi, S.,  
1234 2003. The Sao Tomé deep-sea turbidite system (southern Brazil Basin): Cenozoic  
1235 seismic stratigraphy and sedimentary processes. AAPG bulletin, 87(5), pp.873-894.
- 1236 Waisman, G., 2008, Tectonica de sal da Bacia de Campos: Sal: Geologia e Tectônica. Editora  
1237 Beca, Sao Paulo. Editora Beca, Sao Paulo, p. 314-339.
- 1238 Wang, X., Luthi, S.M., Hodgson, D.M., Sokoutis, D., Willingshofer, E. and Groenenberg, R.M.,  
1239 2017. Turbidite stacking patterns in salt-controlled minibasins: Insights from  
1240 integrated analogue models and numerical fluid flow simulations. Sedimentology,  
1241 64(2), pp.530-552.
- 1242 Winker, C.D., 1996, January. High-resolution seismic stratigraphy of a late Pleistocene  
1243 submarine fan ponded by salt-withdrawal mini-basins on the Gulf of Mexico  
1244 continental slope. In Offshore Technology Conference. Offshore Technology  
1245 Conference.
- 1246 Winter, W., R. Jahnert, and A. França, 2007, Bacia de Campos: Boletim de Geociências da  
1247 PETROBRAS, v. 15, p. 511-529.
- 1248
- 1249

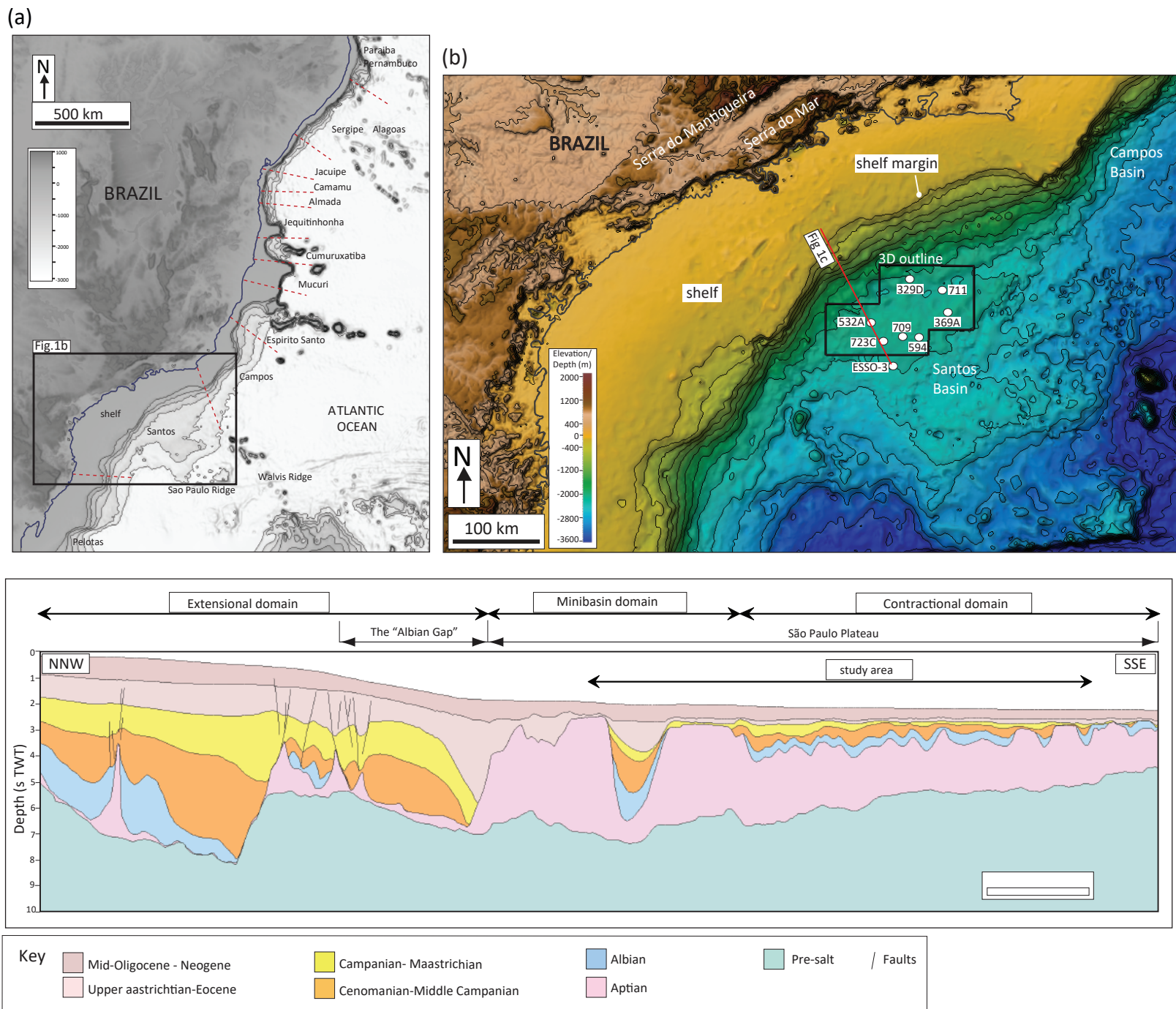
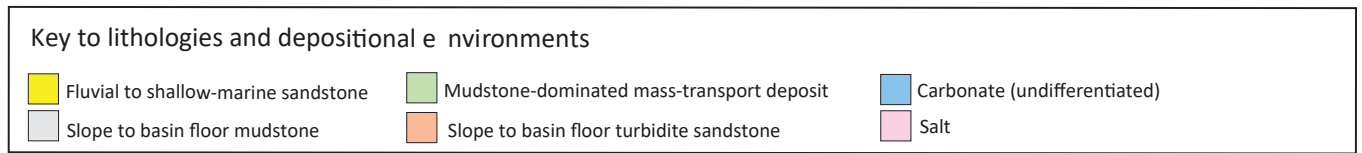
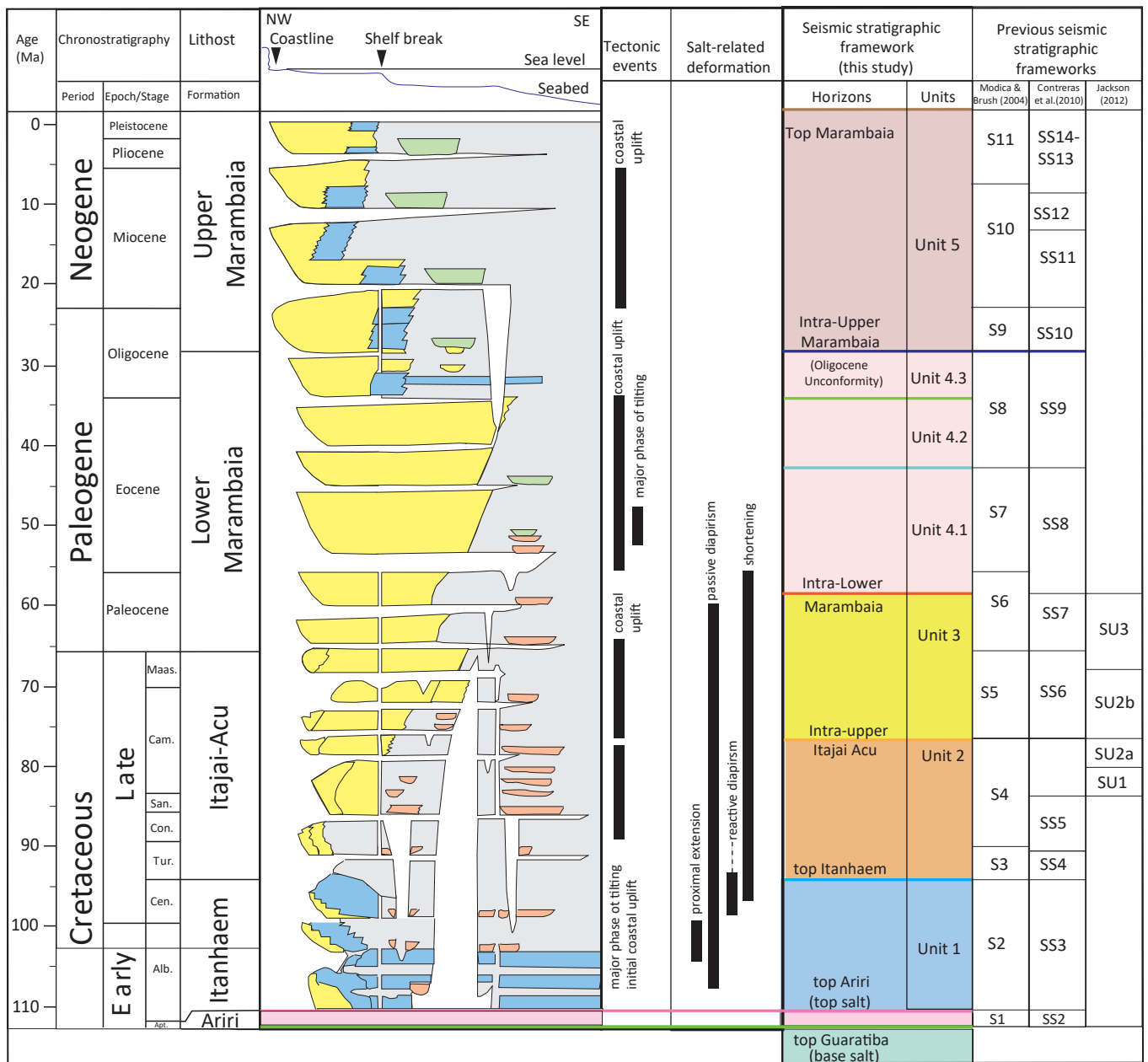


FIGURE 1: (a) Offshore eastern Brazil sedimentary basins; (b) Santos Basin topography and bathymetry map highlighting the location of study area and dataset. 3D seismic reflection data courtesy of CGG and public Brazilian boreholes; (c) Geoseismic profile across the study area based on interpretation of 2D seismic data courtesy of WesternGeco, Schlumberger. See location in b; (d) Seismic stratigraphic framework. After Modica and Brush (2004); Moreira et al. (2007); Jackson (2012).

(d)





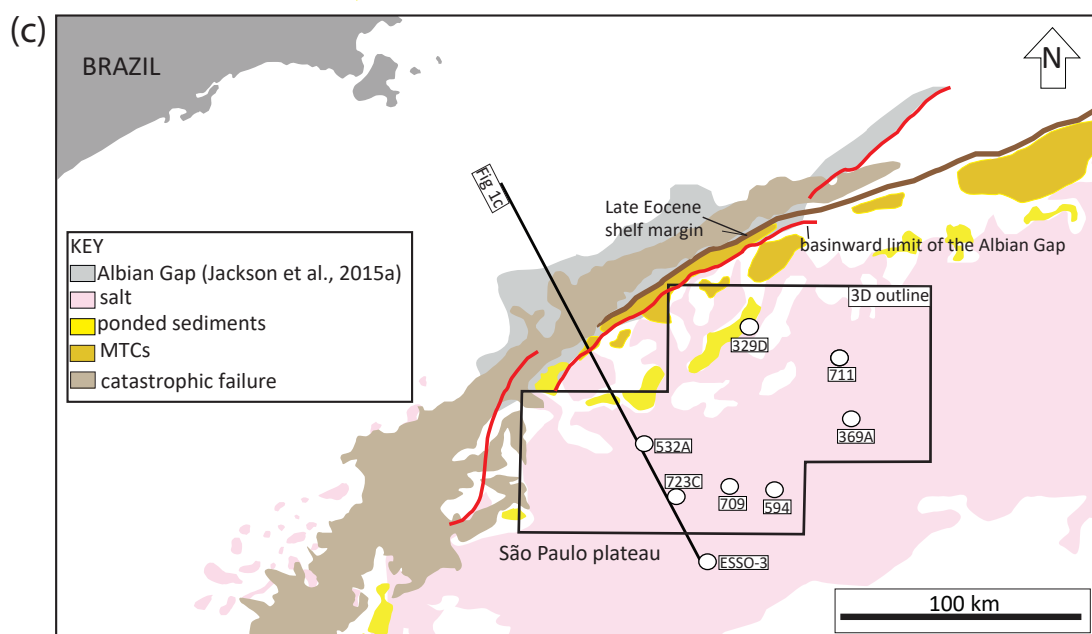
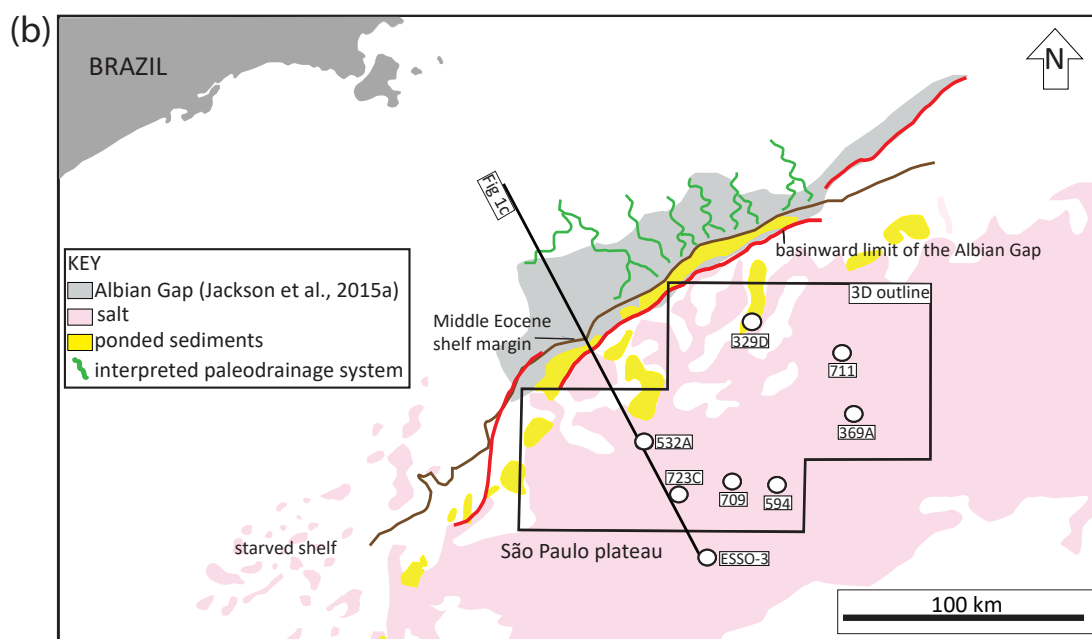
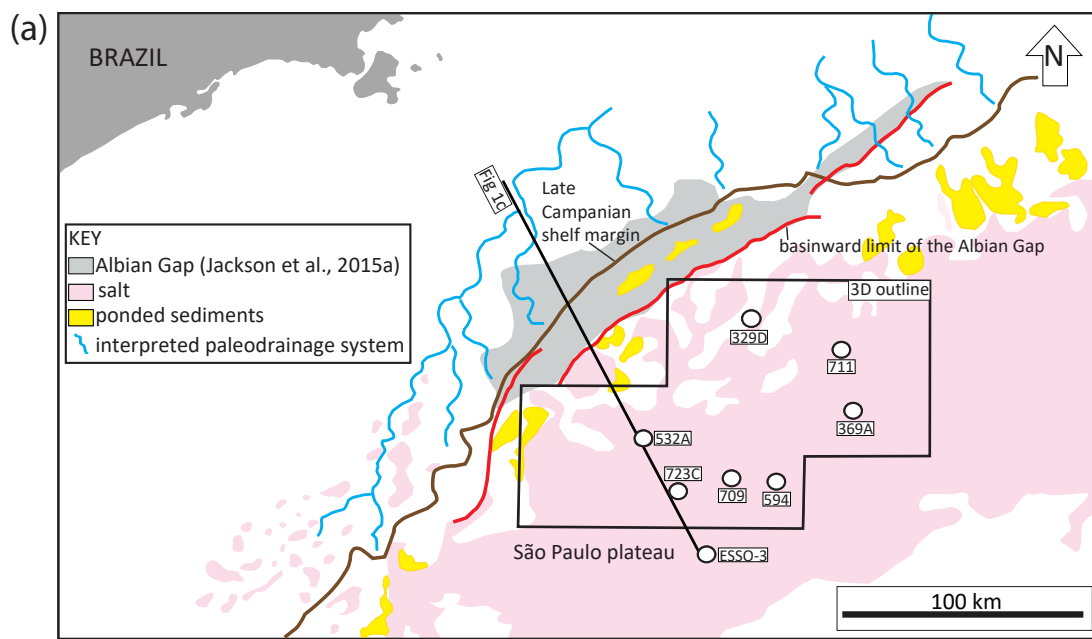


Figure 2: Central deepwater Santos Basin paleogeography highlighting sedimentation trapped or ponded landwards of the Albian Gap with limited deposition in the area of study. Modified after Modica and Brush, 2004. (a) Late Campanian paleogeography; (b) Middle Eocene paleogeography; (c) Late Eocene paleogeography.

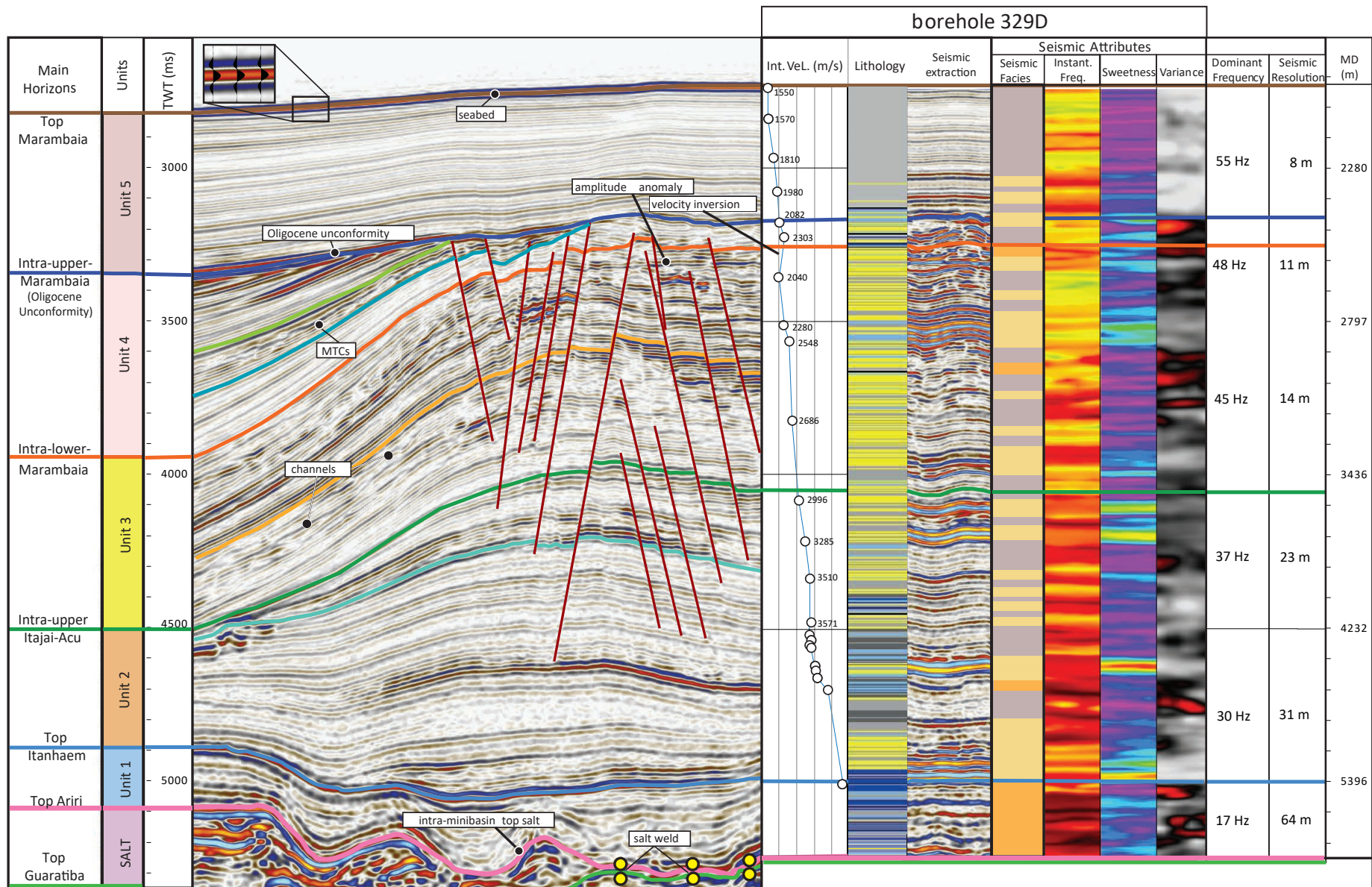
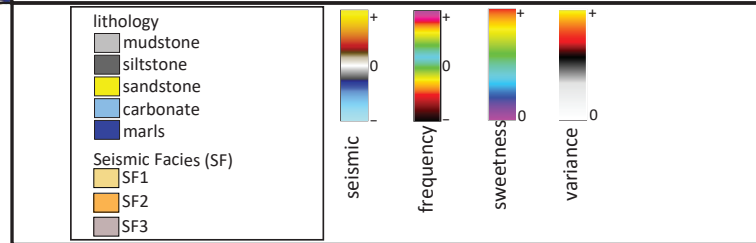


FIGURE 3: Intra-minibasin seismic-well correlation. Key seismic horizons and units are indicated and defining a turtle anticline due to inversion of the minibasin stratigraphy. Seismic attributes response highlights vertical variations in seismic facies within the minibasin. See also Table 2 for a description of SF1, SF2, and SF3. Dominant frequency and vertical seismic resolution decrease with depth, as indicated in the last three columns and in Table 1. Borehole location is shown in Figure 4a



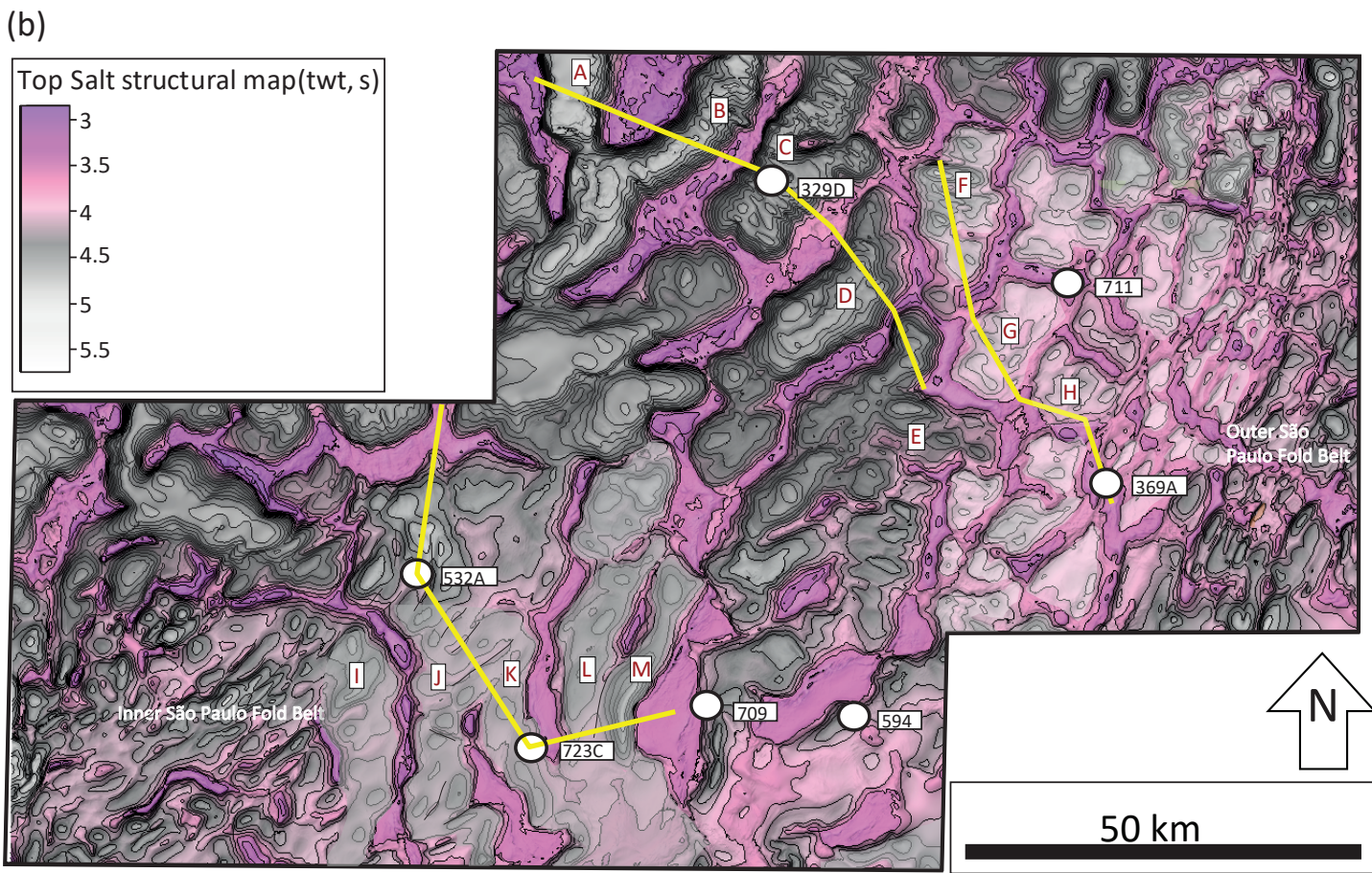
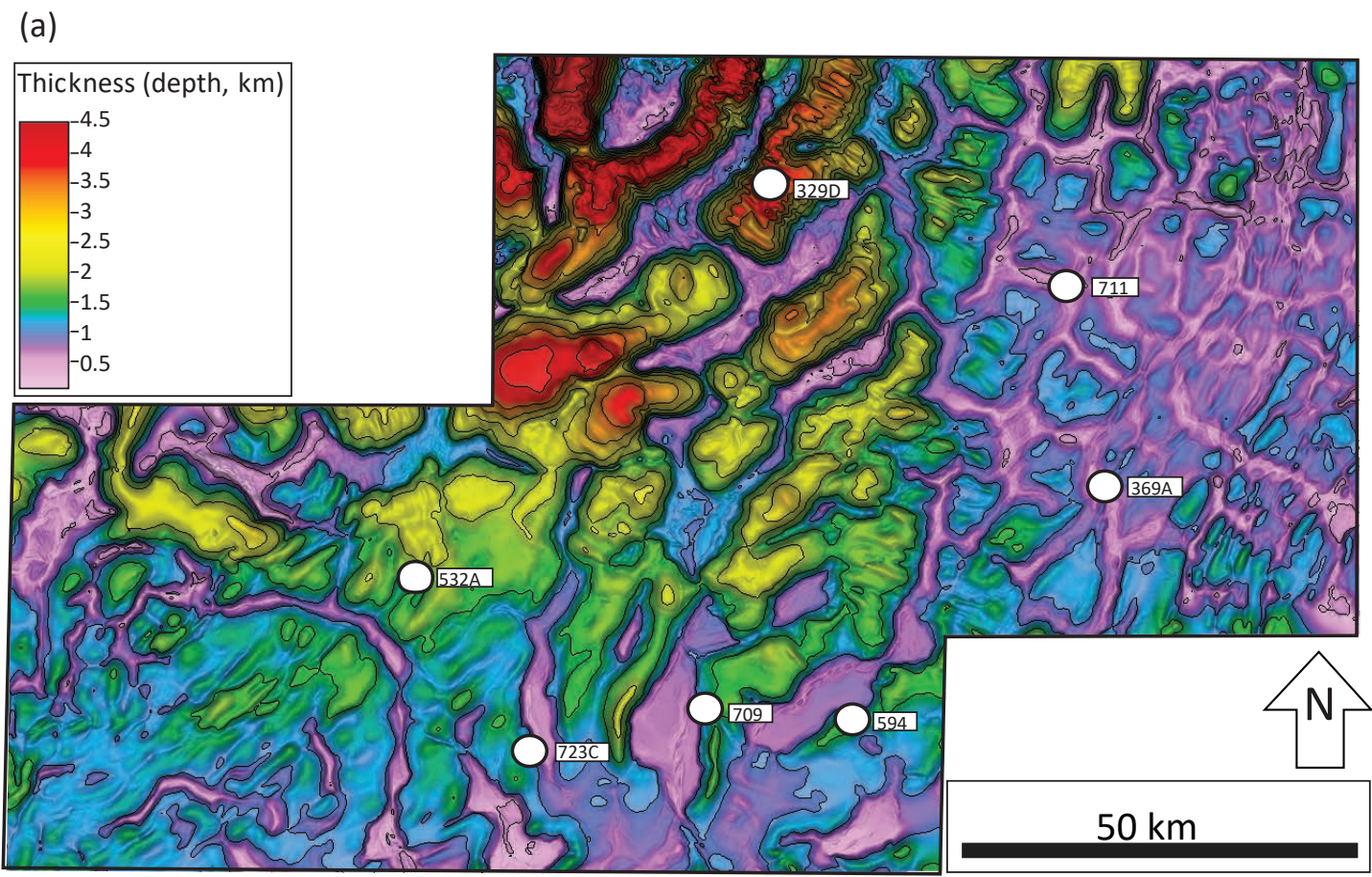
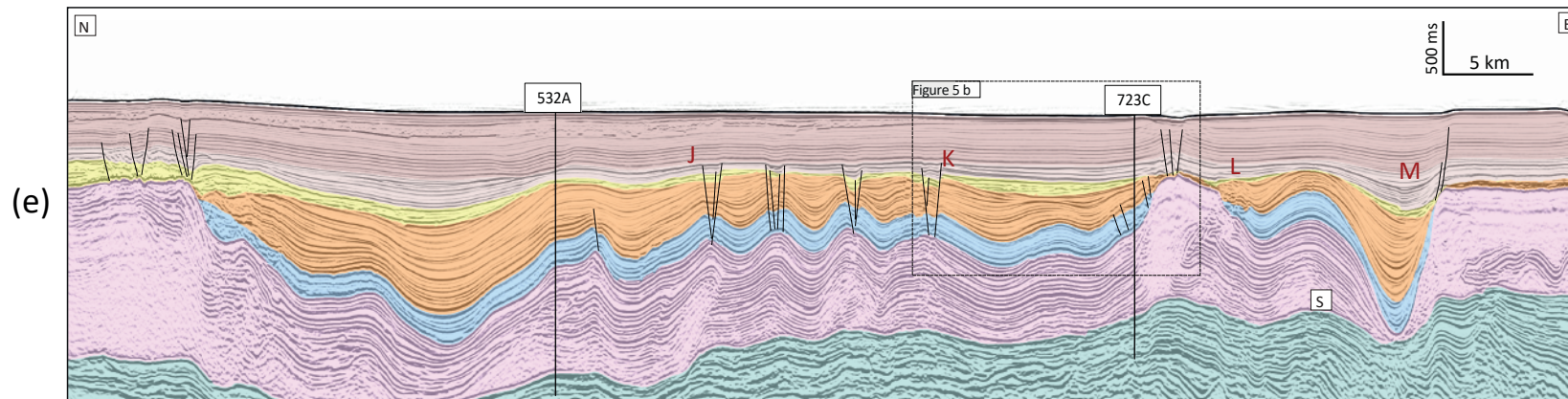
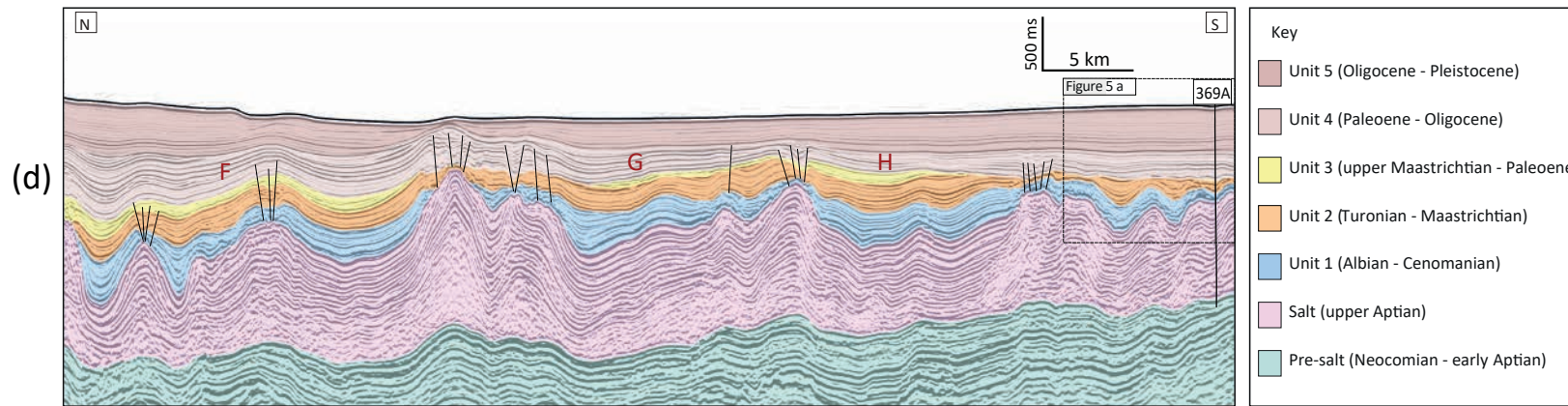
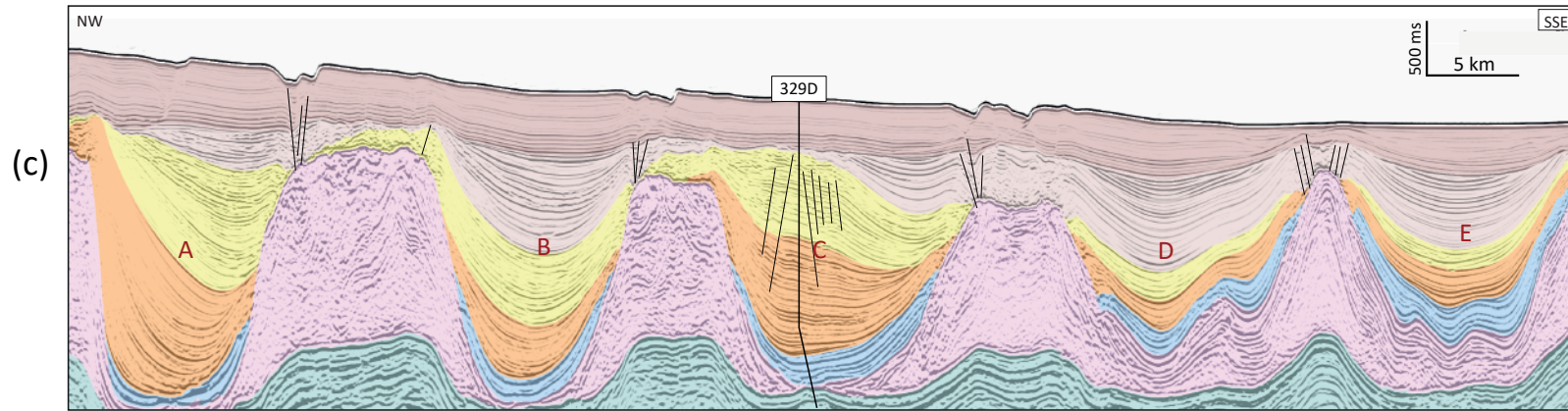


FIGURE 4: (a) Postsalt isopach (Seabed to top salt depth thickness map) illustrating sediment thickness variations across the study area. Depth thickness map estimated using the depth-converted seafloor depth structural map and the top salt structural map also in depth; (b) Top Salt structural map highlighting present-day salt structures bounding the minibasins of interest, i.e. updip proximal thick minibasins (A-E), shallow minibasins (F-H), and downdip distal minibasins (I-M) ; (c) Geoseismic section across the updip proximal thick minibasins; (d) Geoseismic section across the medial shallow minibasins; (e) Geoseismic section across the downdip distal elongated minibasins. See Figure 4b for location of geoseismic profiles.



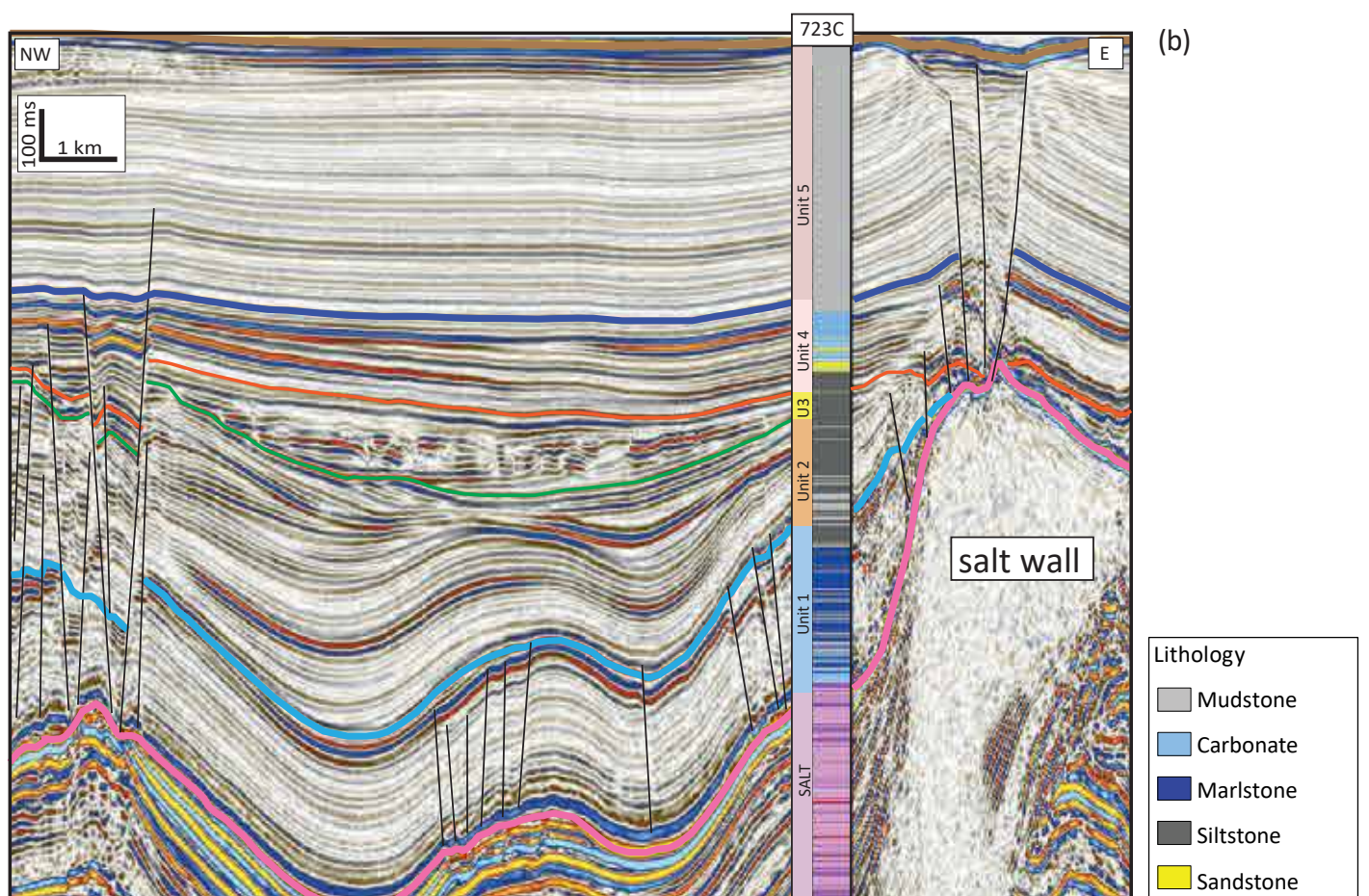
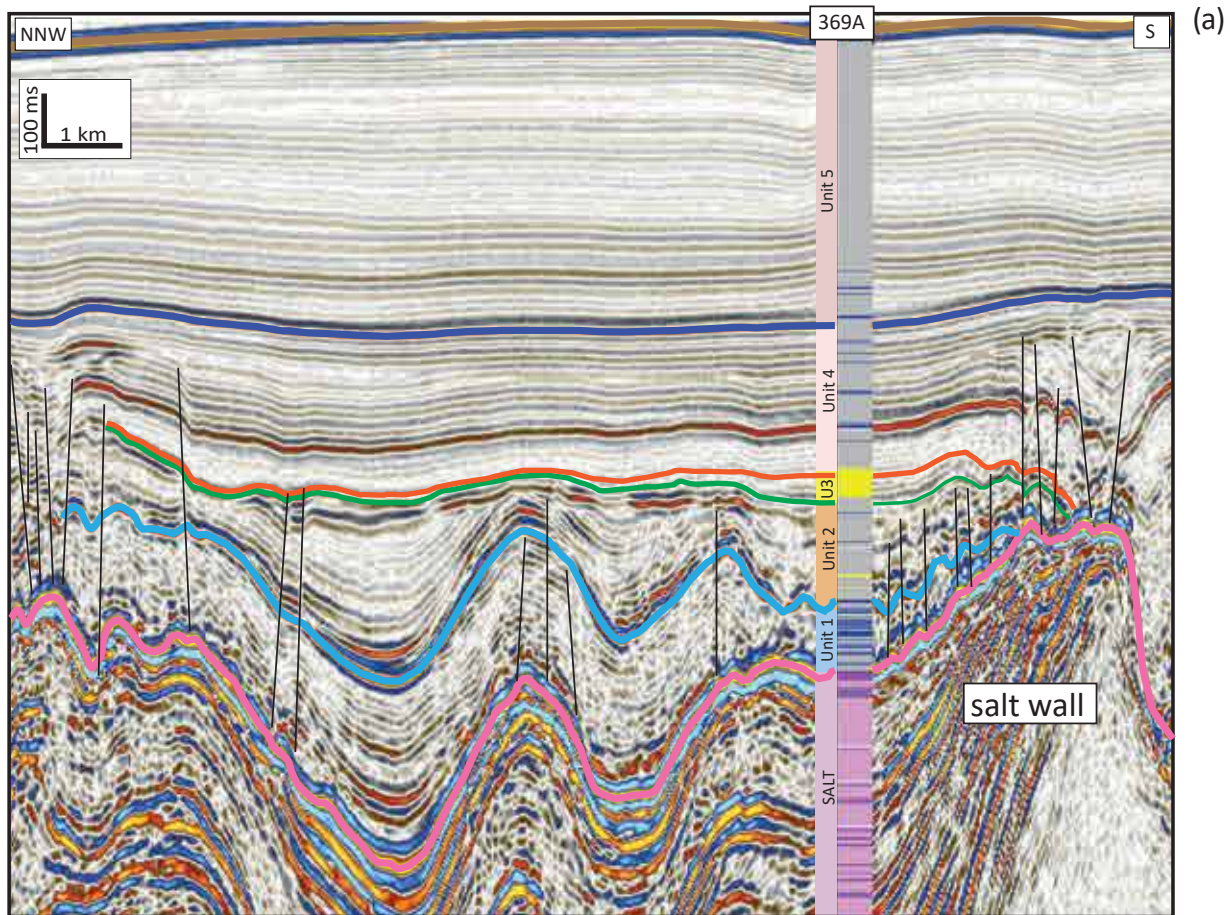


FIGURE 5: Intra-minibasin seismic-well tie showing the presence of reservoir-prone sandstones in distal locations, i.e., > 50 km from the coeval shelf margin. (a) Borehole 369a penetrates a medial shallow minibasin. See Figure 4a for location. (b) Borehole 723C penetrates the flank of a downdip distal minibasin. See Figure 4a for location.

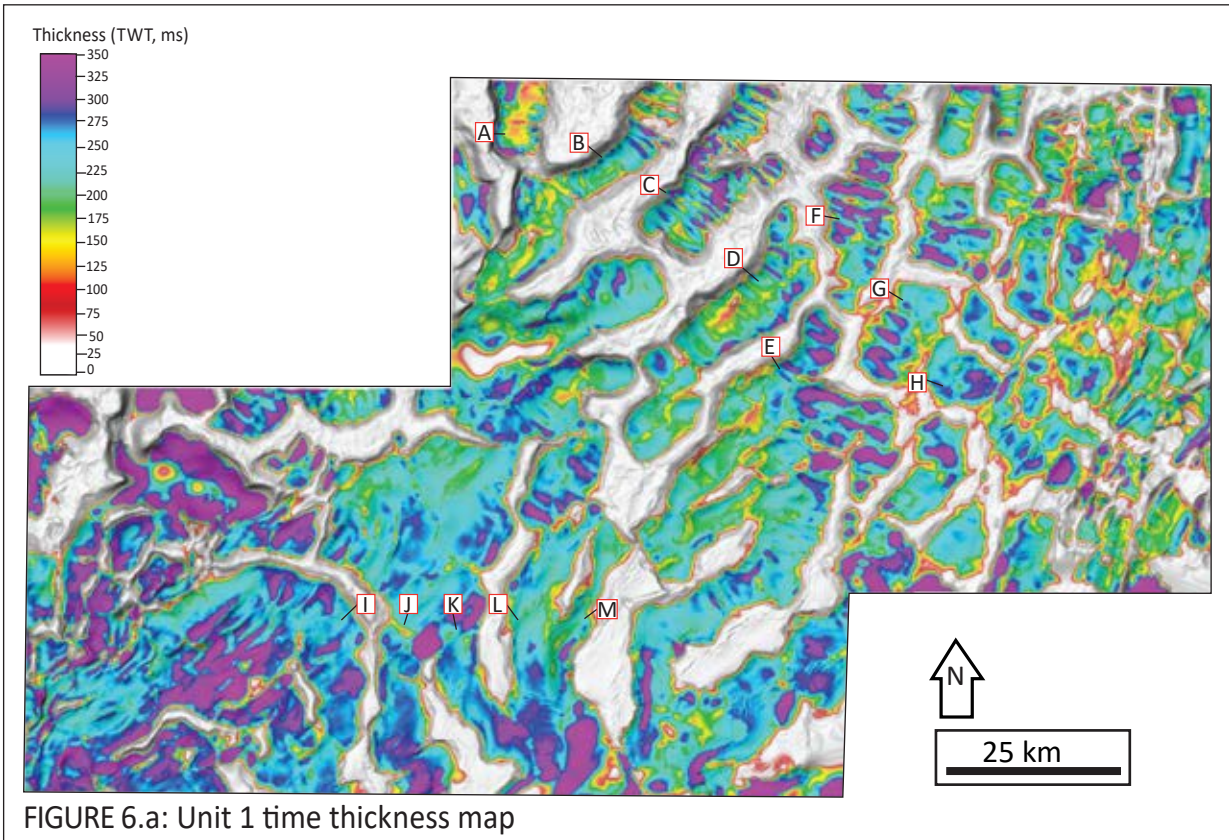
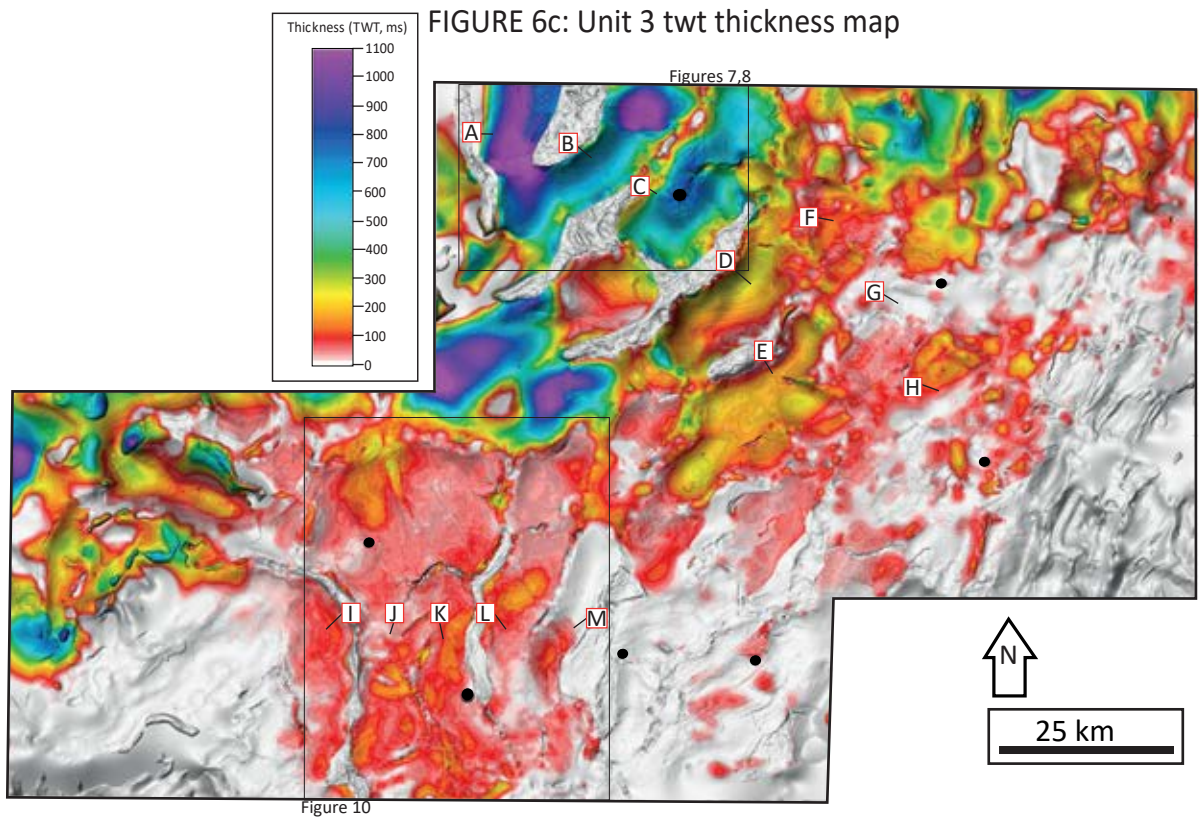
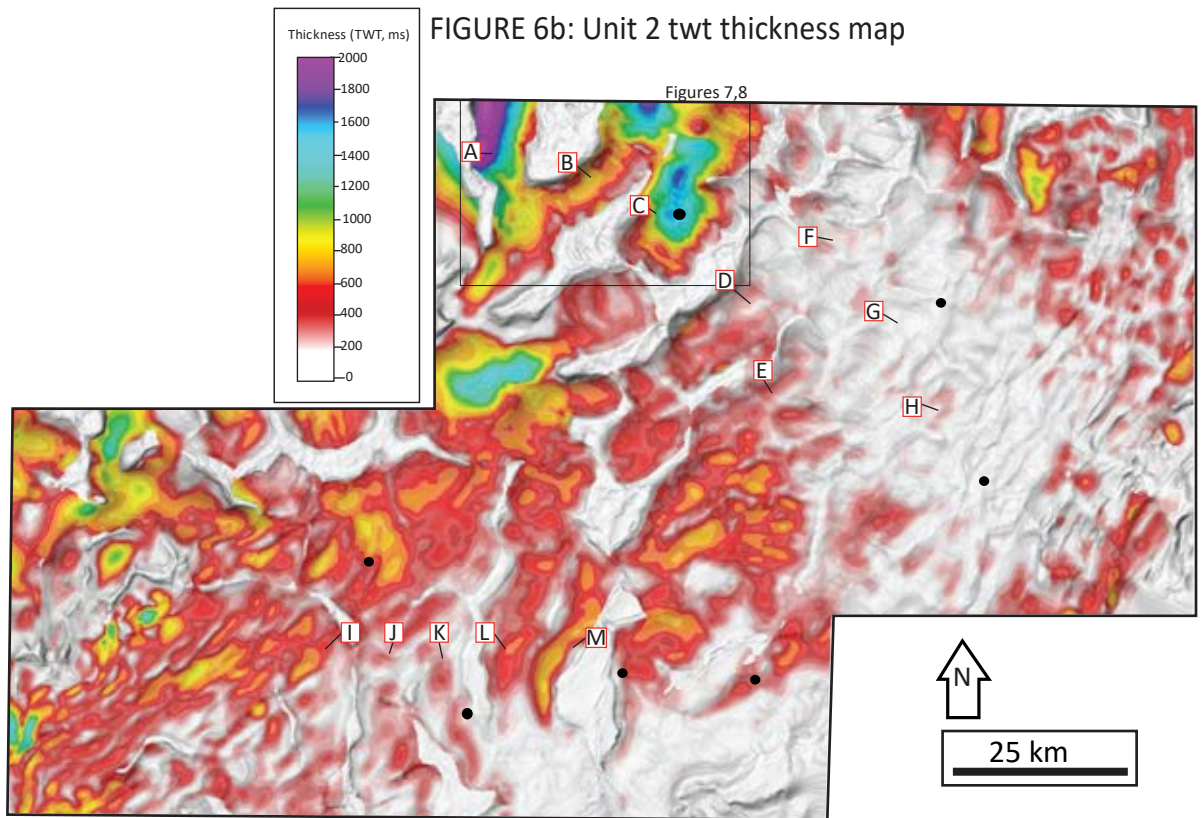


FIGURE 6: Regional isochrons illustrating deposition and salt-related deformation in the post-salt of central deep-water Santos Basin. (a) Albian-Cenomanian unit 1 twt thickness map; (b) Turonian to Mid-Campanian Unit 2 twt thickness map; (c) Campanian to Paleocene Unit 3 twt thickness map; (d) Paleocene to Mid Oligocene Unit 4 twt thickness map; (e) Mid-Oligocene to present-day Unit 5 twt thickness map.



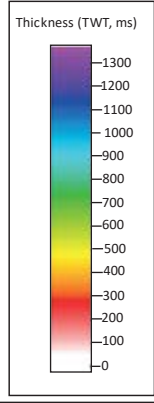


FIGURE 6d: Unit 4 twt thickness map

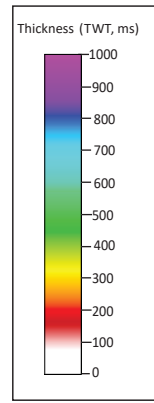
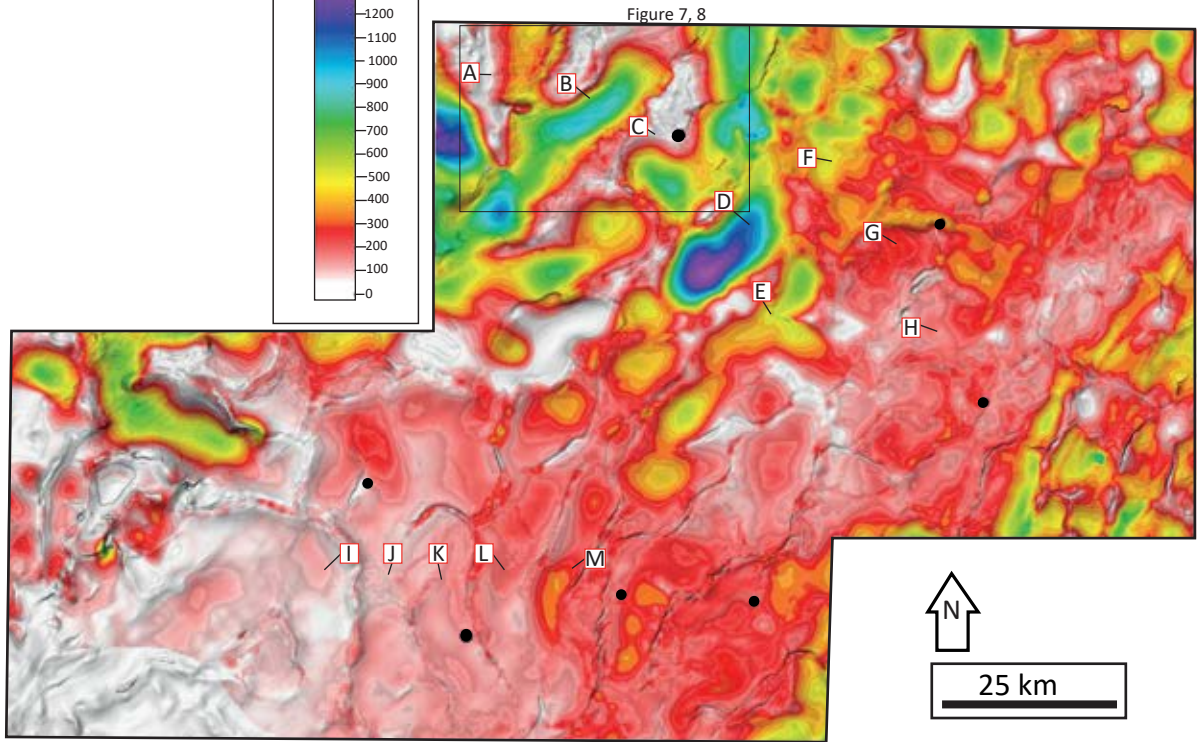
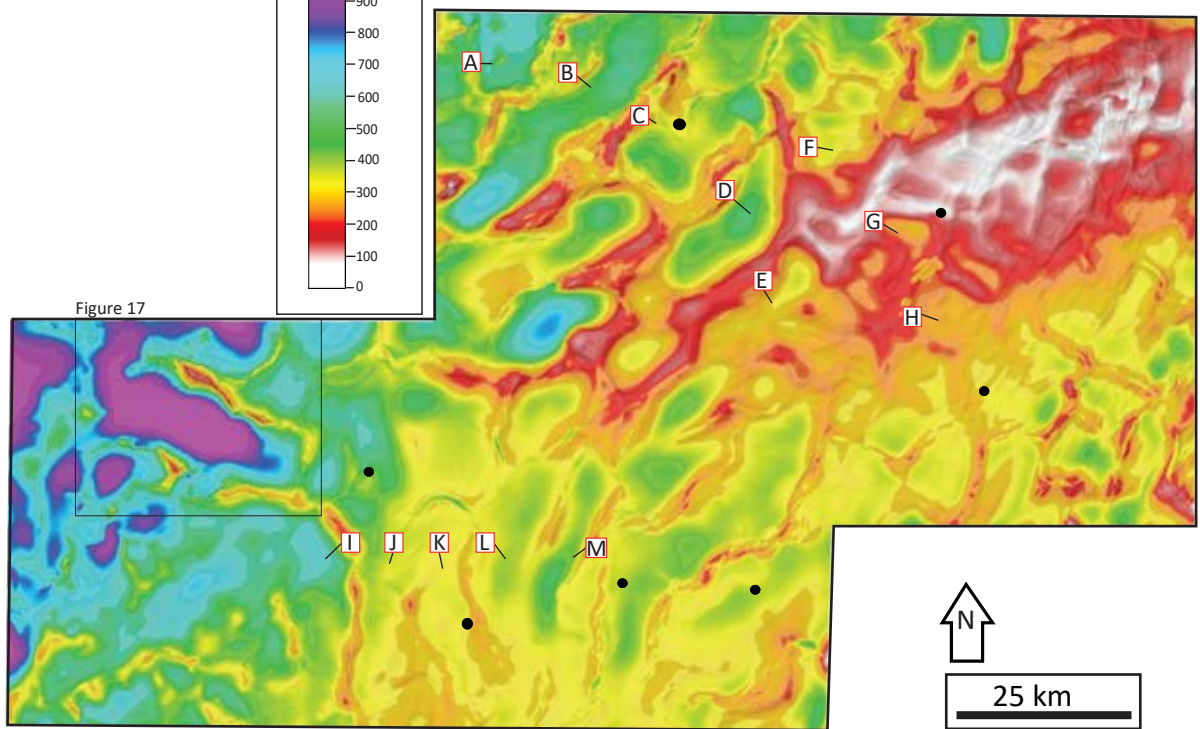


FIGURE 6e: Unit 5 twt thickness map





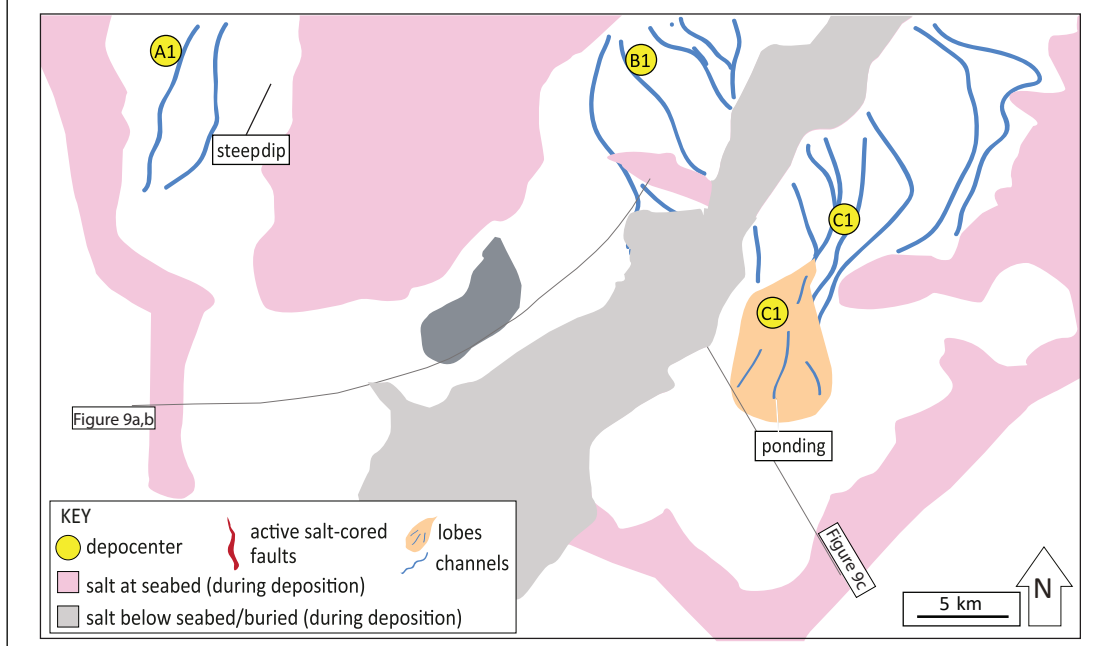
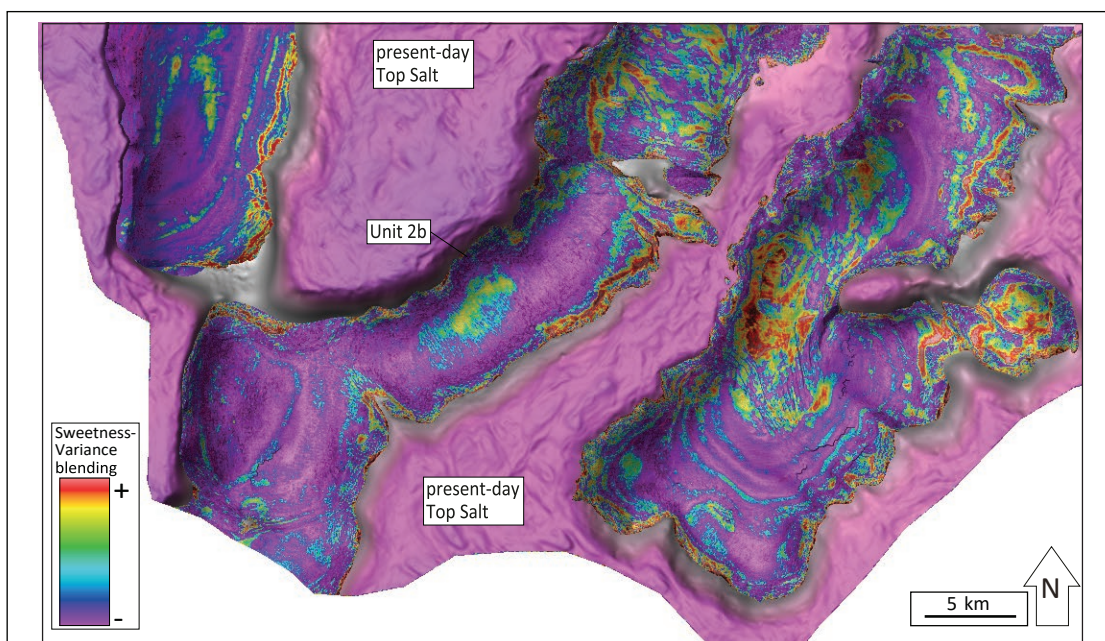
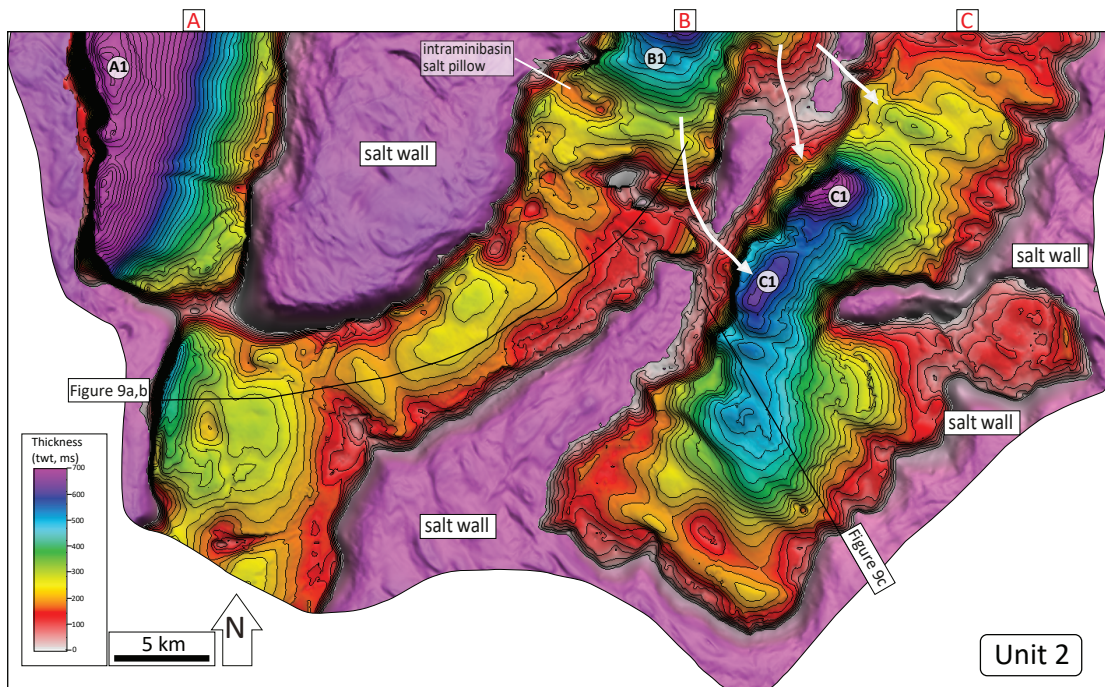


FIGURE 7: (a) Unit 2 thickness map highlighting initial depocenters A1, B1 and C1 within updip proximal minibasins A, B and C. Present-day Top Salt is shown in pink. (b) Unit 2b seismic attributes blending (interval is shown on section in Figure 9c). Present-day Top Salt structure map is shown in pink. Attributes visually blended correspond to Variance and Sweetness (described in the Methods section). Purple colours correspond to more transparent background facies. Yellow to red colours highlight deep-water depositional elements interpreted in the accompanying map. Depocenters A1, B1 and C1 are interpreted based on thickness map in Figure 7a.

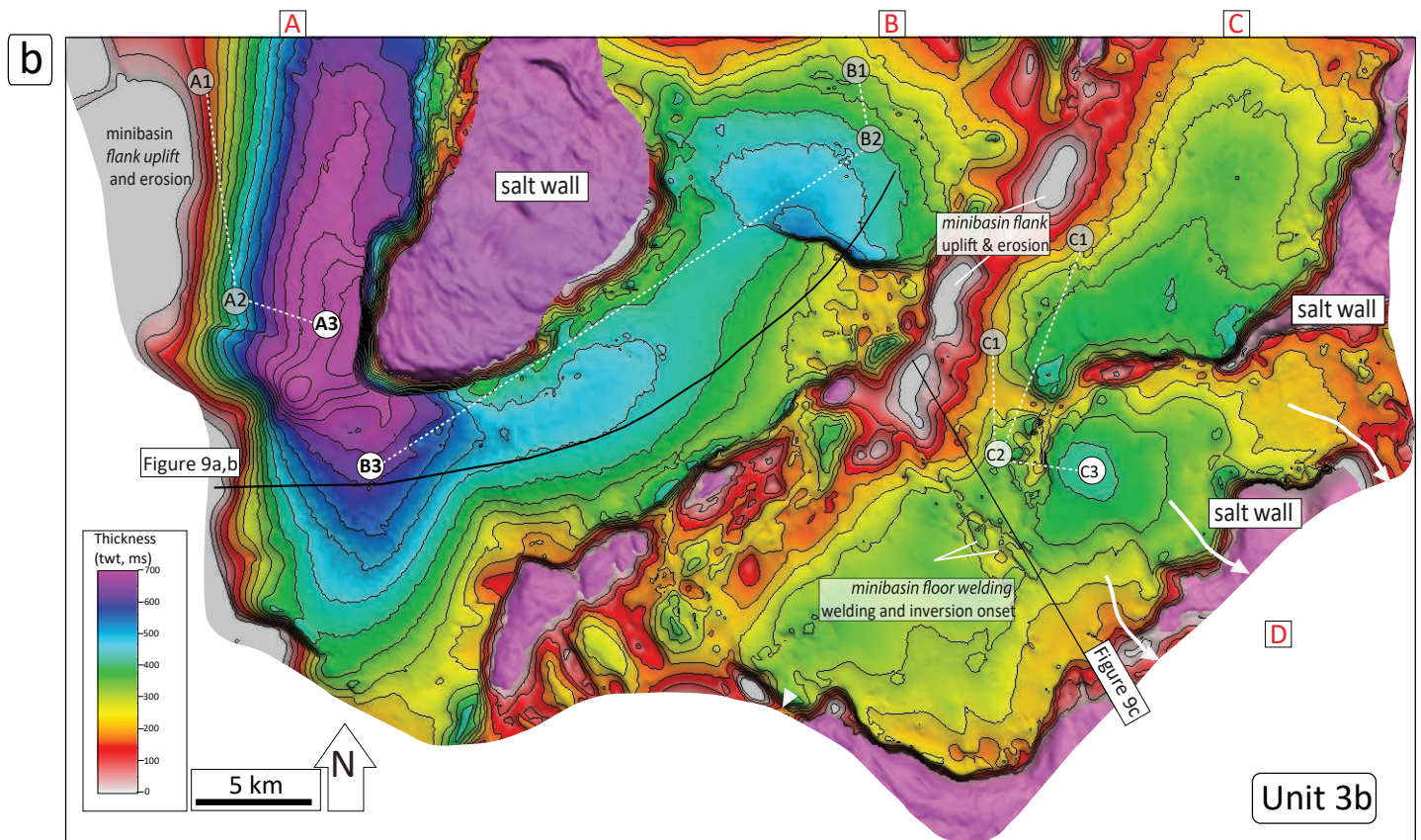
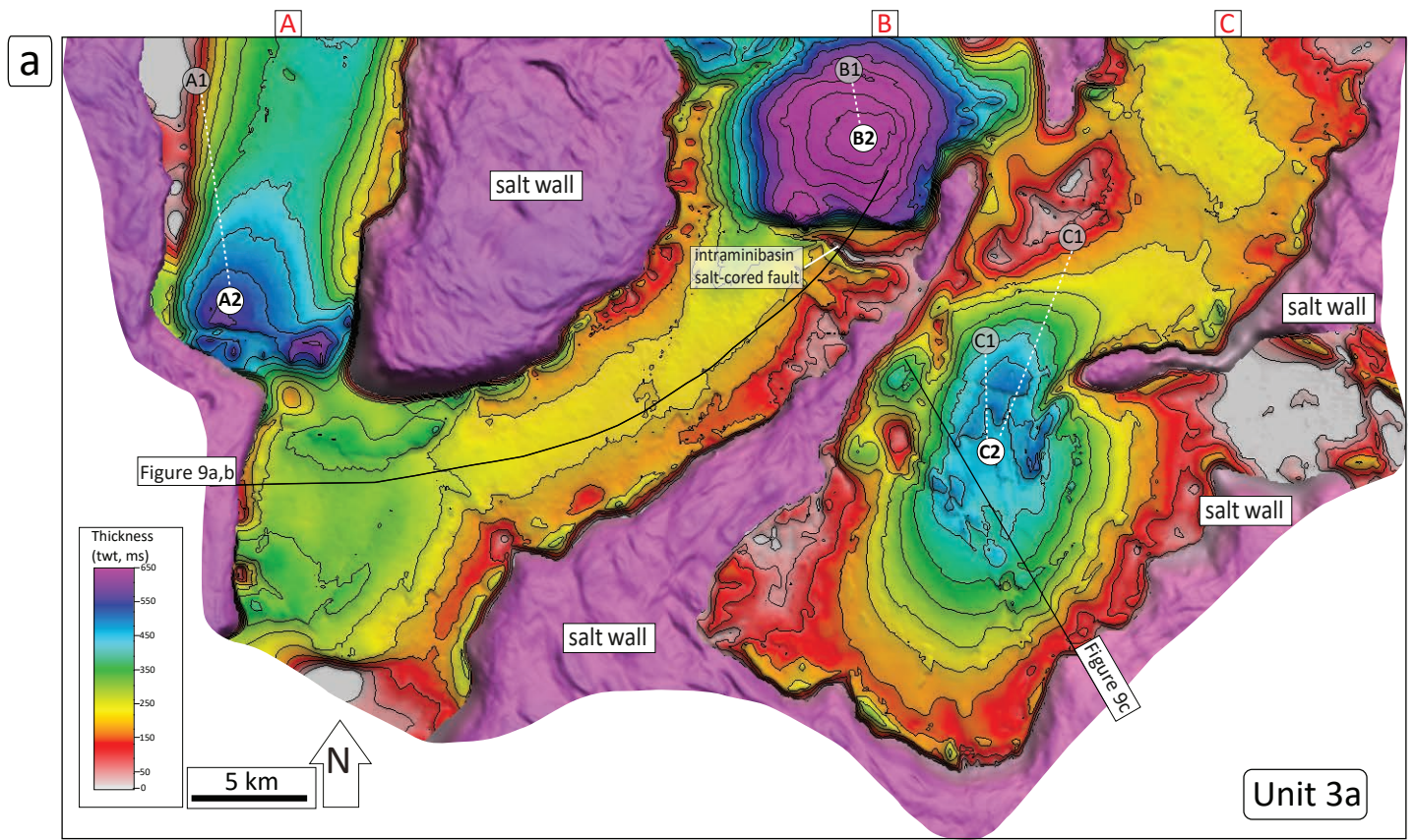
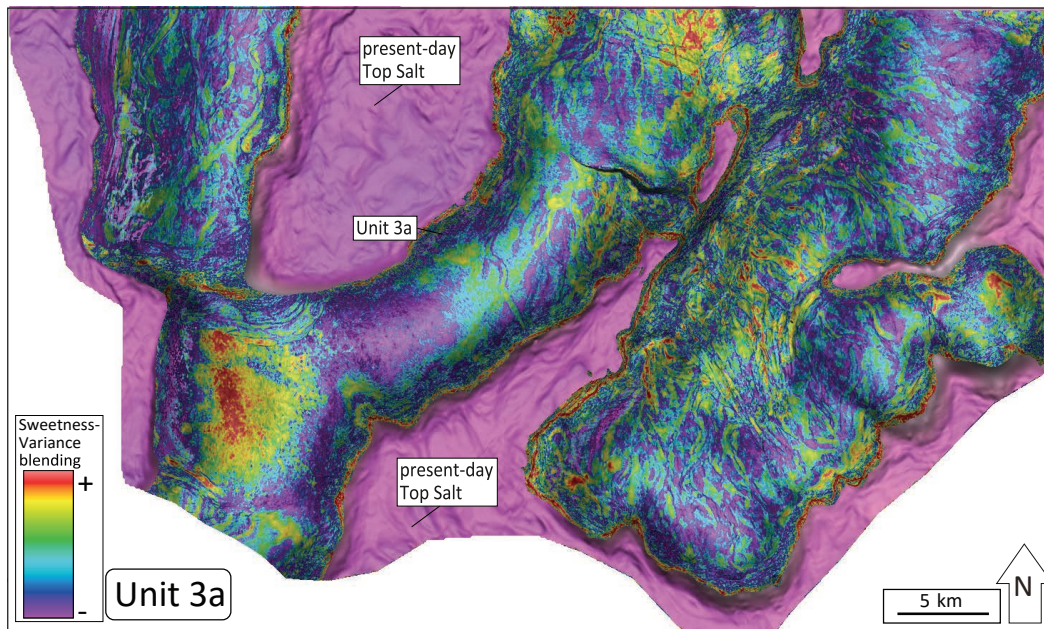
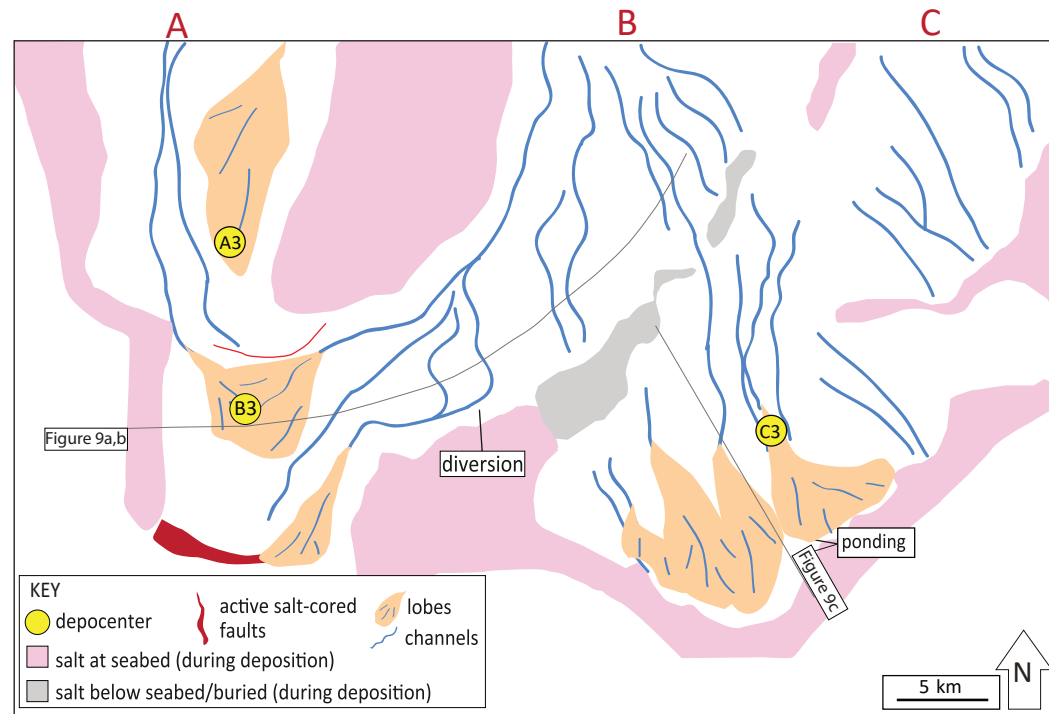
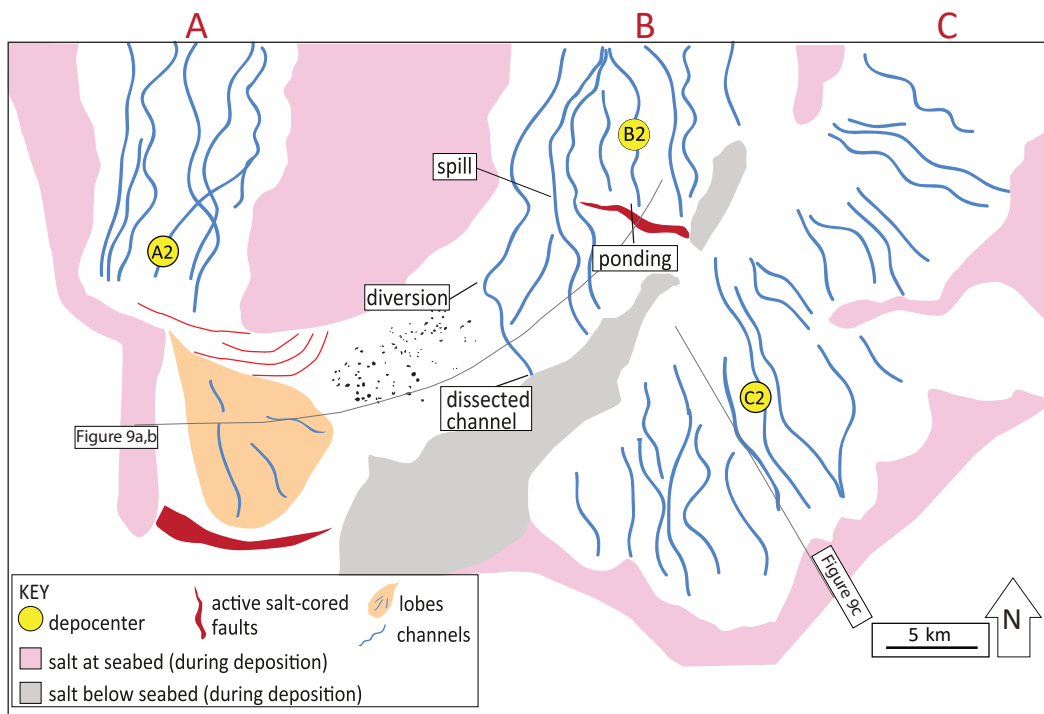
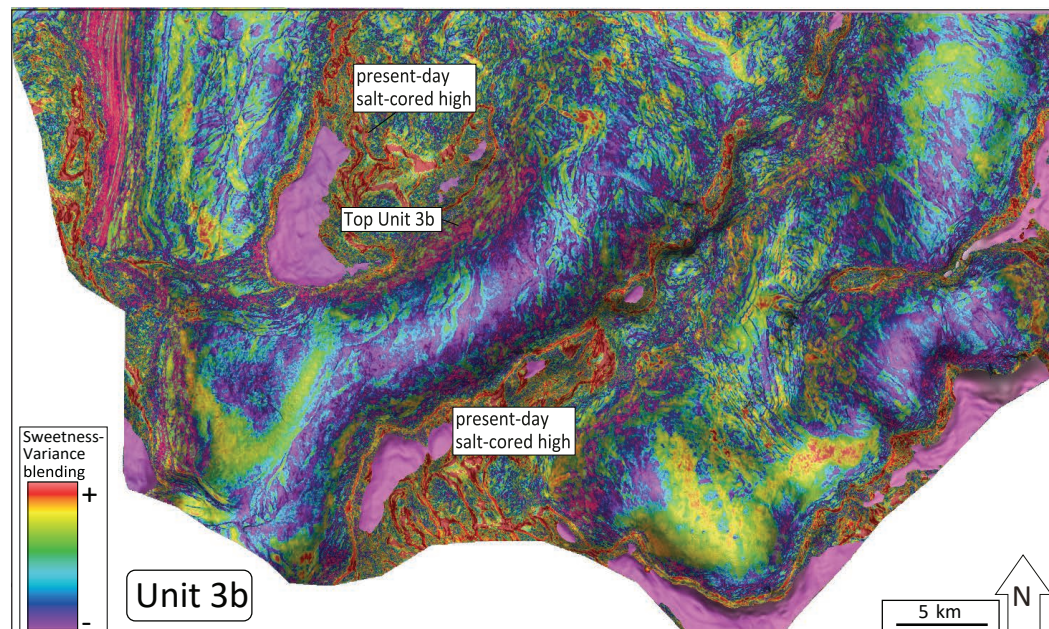


FIGURE 8: (a) Proximal thick minibasins - Sub-Unit 3a isochron highlighting shifting of depocenters A1, B1, C1 (Fig. 7a) to new depocenters A2, B2 and C2. Present-day Top Salt is shown in pink. (b) Proximal thick minibasins - Sub-Unit 3b isochron highlighting shifting of depocenters A2, B2 and C2 (Fig 8a) to new depocenters A3, B3 and C3. (c) Sub-unit 3a seismic attributes blending and interpretation. Sub-unit 3a is shown on sections in Figures 9a, b and c. Visually blended seismic attributes correspond to Variance and Sweetness described in the Methods section. Purple and dark blue colours correspond to more transparent background facies. Yellow to red colours highlight deep-water depositional systems interpreted in the accompanying map. Depocenters are interpreted based on the isochron (Fig. 8a). (d) Sub-unit 3b seismic attributes blending and interpretation. Sub-unit 3b is shown on sections in Figures 9a, b and c. Visually blended attributes correspond to Variance and Sweetness. Purple and dark blue colours correspond to more transparent background facies. Yellow to red colours highlight depositional elements interpreted in the accompanying map. Depocenters are interpreted based on the isochron (Fig. 8b).

**c****d**

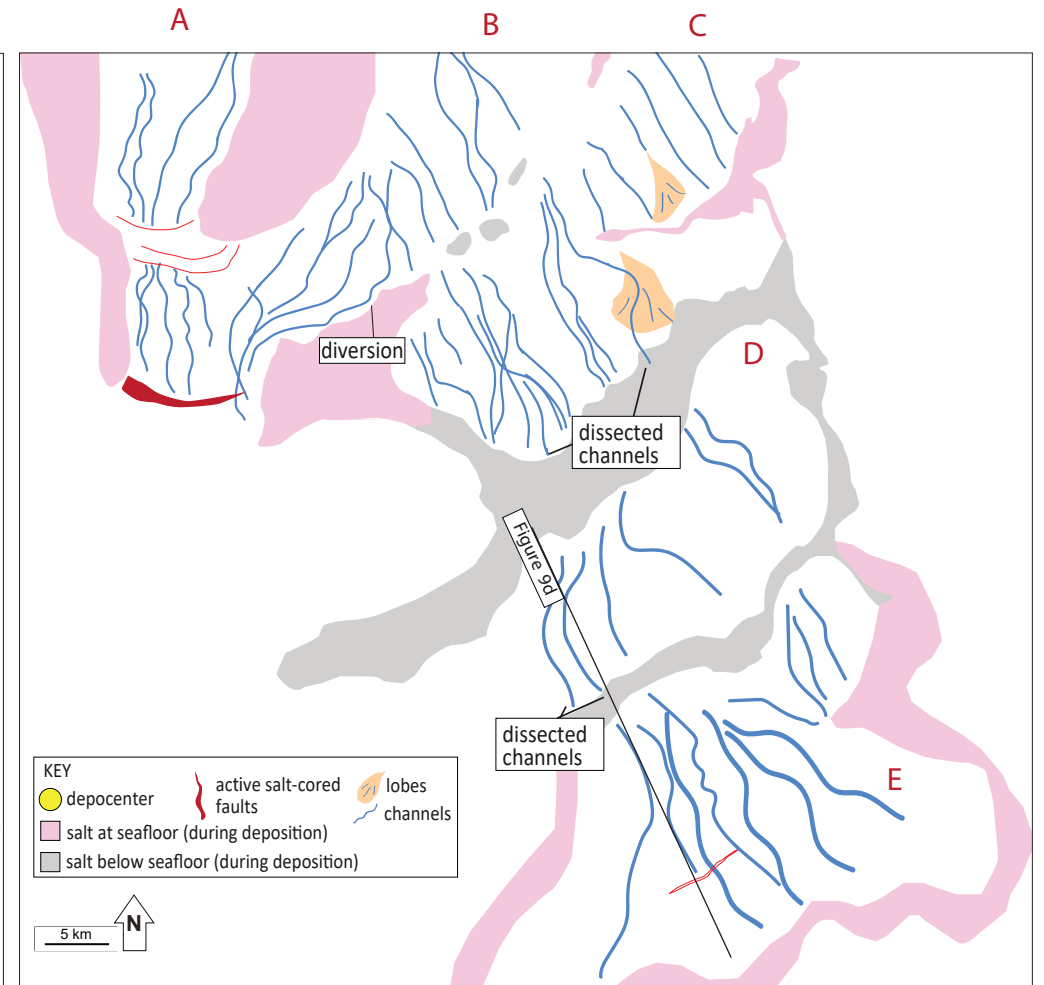
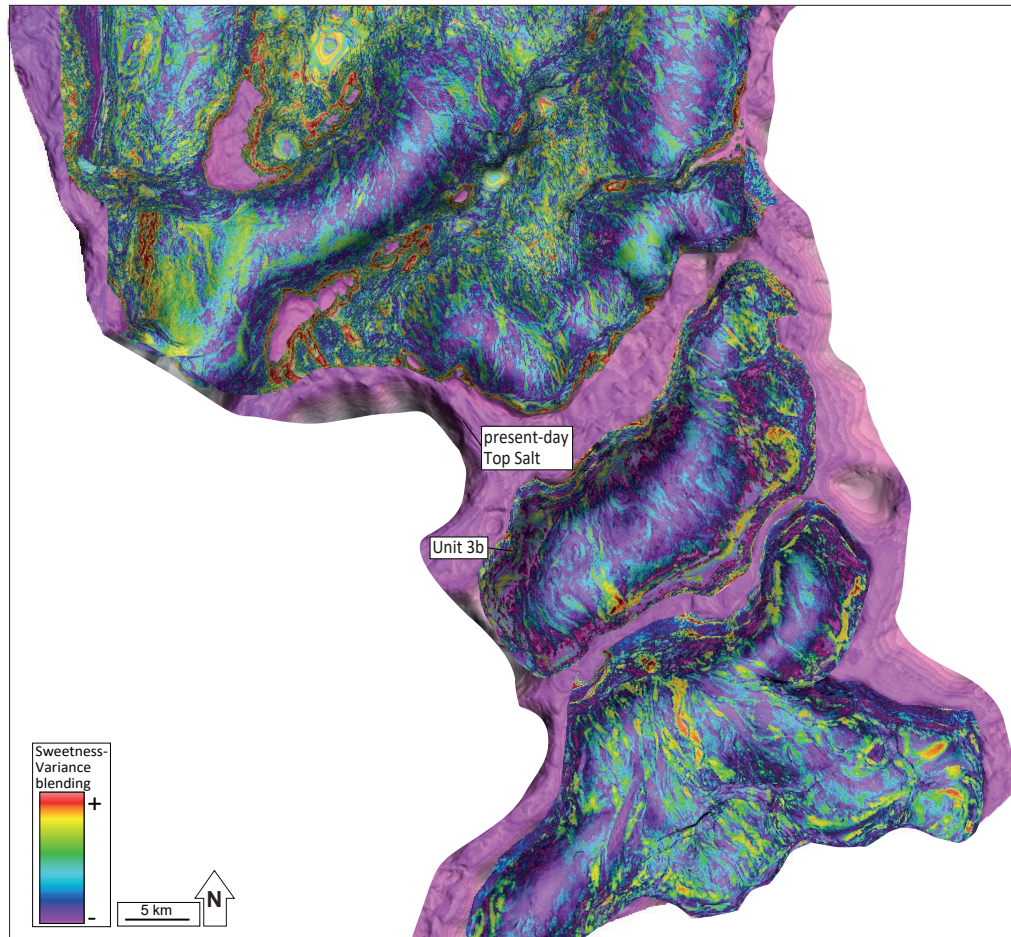


Figure 8e: Unit 3b sweetness and variance attribute visual blending illustrating the post-depositional dissection of submarine clastic systems caused by the rise of the salt wall presently bounding minibasins B and C, C and D and D and E.

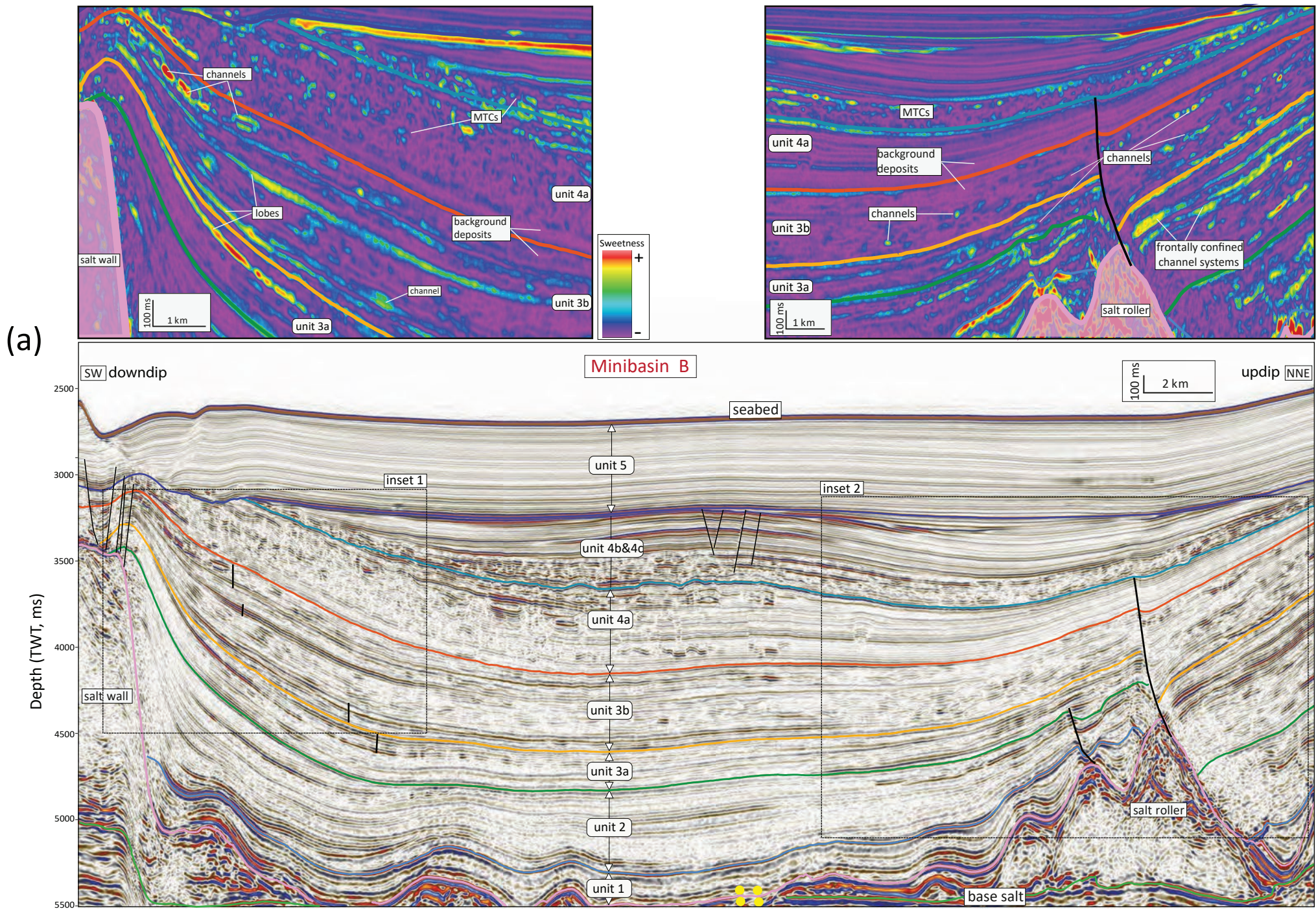


Figure 9: Seismic profiles along and across the updip/proximal minibasins illustrating the key horizons and units mapped and the thickness and seismic facies variations defining the minibasin stratigraphy. Highly-reflective intervals correspond to interpreted depositional elements highlighted with seismic attributes in Figure 8. The locations of the seismic sections are also shown on Figure 8. (a) Seismic section along Minibasin B. Insets illustrate potential sandstone-rich depositional elements with an amplitude- and frequency-based seismic attribute (Sweetnes).

(b)

Minibasin B

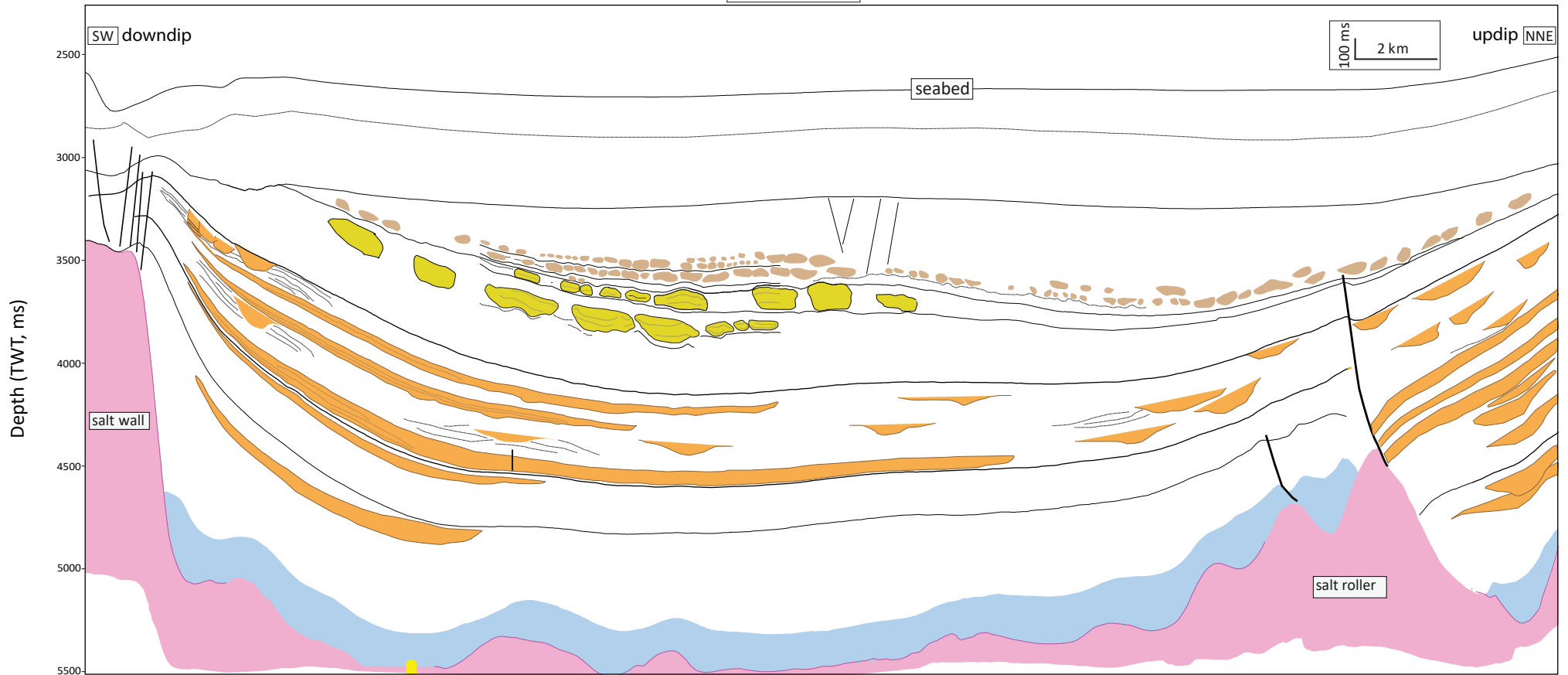
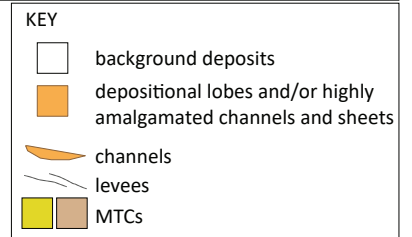


Figure 9 (cont.): (b) Laterally and frontally confined deep-water depositional elements along minibasin B based on seismic stratigraphic interpretation and seismic attribute analysis.



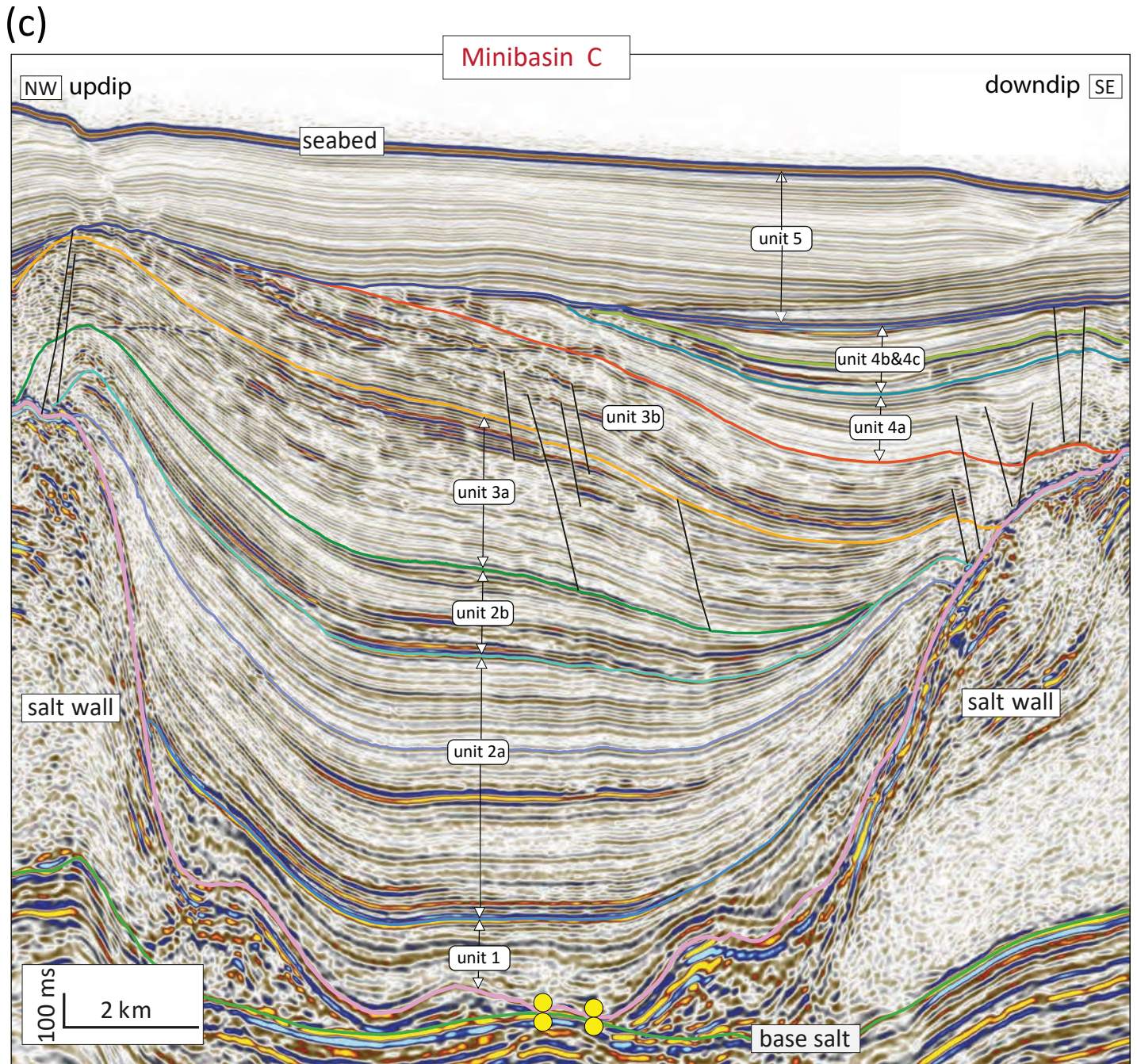


Figure 9 (cont.): (c) Seismic profile across Minibasin C illustrating the main units interpreted. Initial confinement is illustrated by thinning and onlapping of minibasin stratigraphy towards the downdip (SE) salt wall (units 2a, 2b and 3a). Minibasin filling and welding led to inversion of the minibasin stratigraphy (units 2a, 2b, and 3a), and spilling and shifting of the initial depocenters from Minibasin B towards the SE and downdip minibasins (units 3b and 4). See location of seismic profile in Figure 8

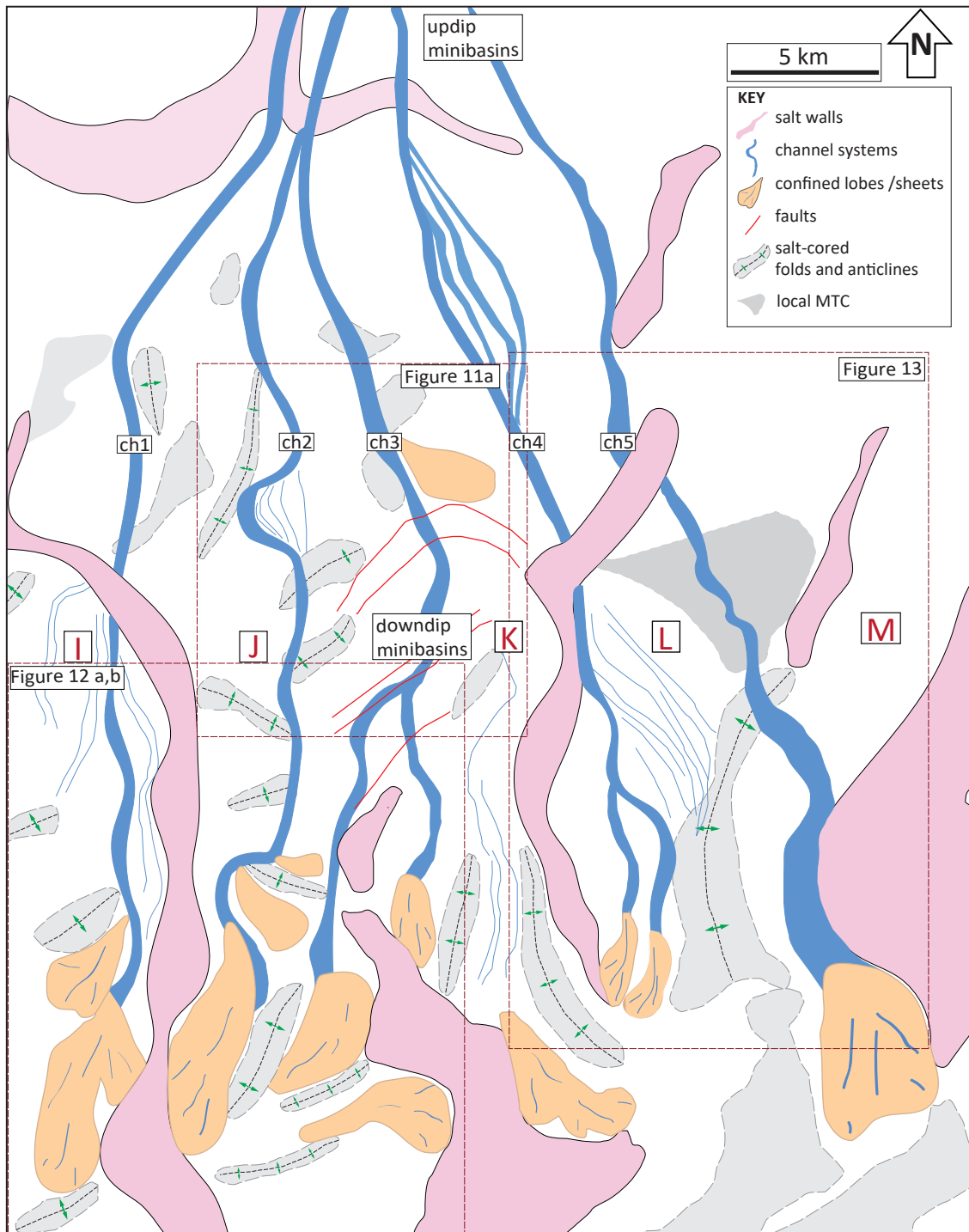


FIGURE 10: Deep-water depositional systems and distal downdip minibasins (I, M) in the Inner São Paulo Fold Belt and the São Paulo Plateau. Updip, channel systems are relatively linear and unconfined. Local variations in architecture are controlled by salt-cored folds and anticlines and salt walls. Lateral and frontal confinements is observed downdip. See area location in Figure 6c. Interpretation is based on seismic stratigraphy, geomorphology, seismic attributes and thickness maps. Detailed isochrons, attribute maps, and seismic sections are shown in Figures 11-14.



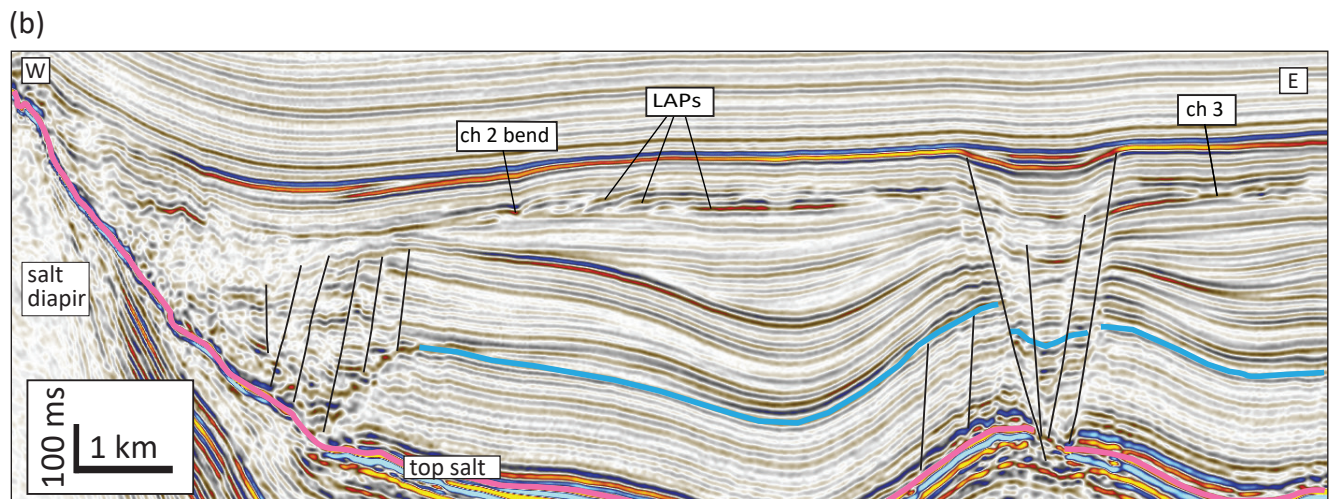
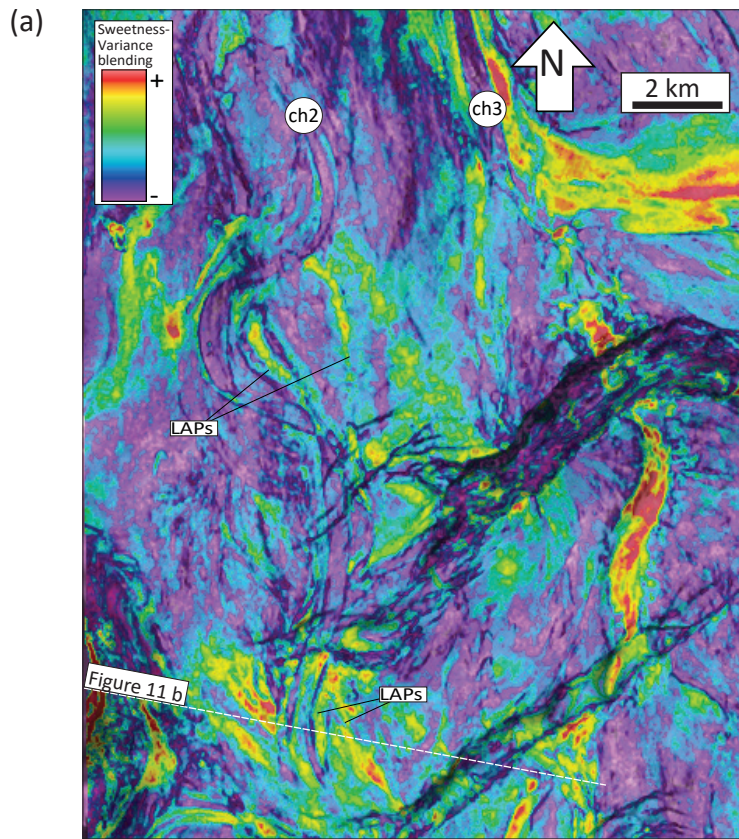


FIGURE 11: (a) Sweetness and variance blending illustrating local increase in channel sinuosity and lateral accretion packages described in Table 3. See channel 2 location and associated structural elements in Figure 10. (b) Seismic section illustrating channel bend and high-amplitude lateral accretion packages. See Figure 11a for location of seismic section.

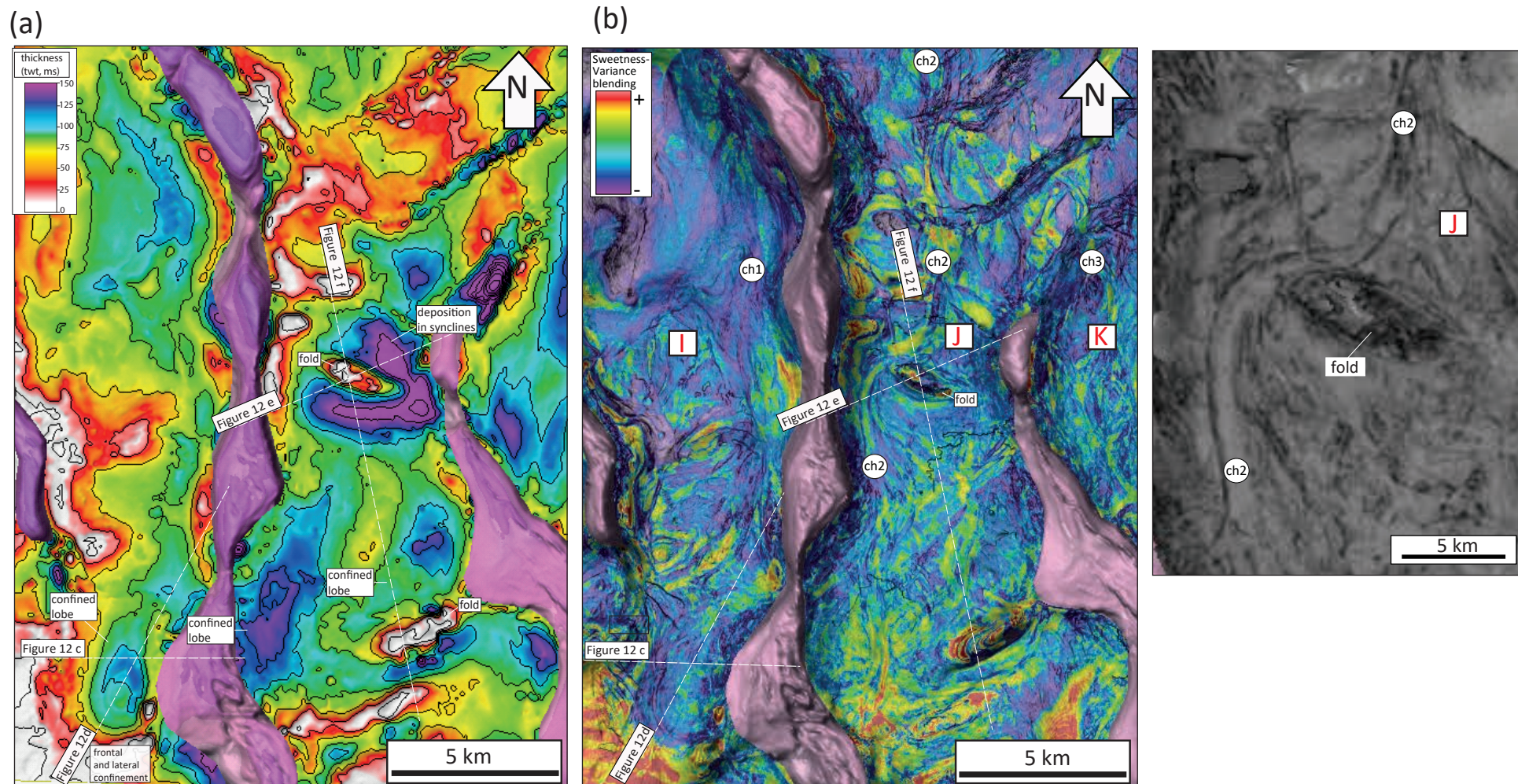
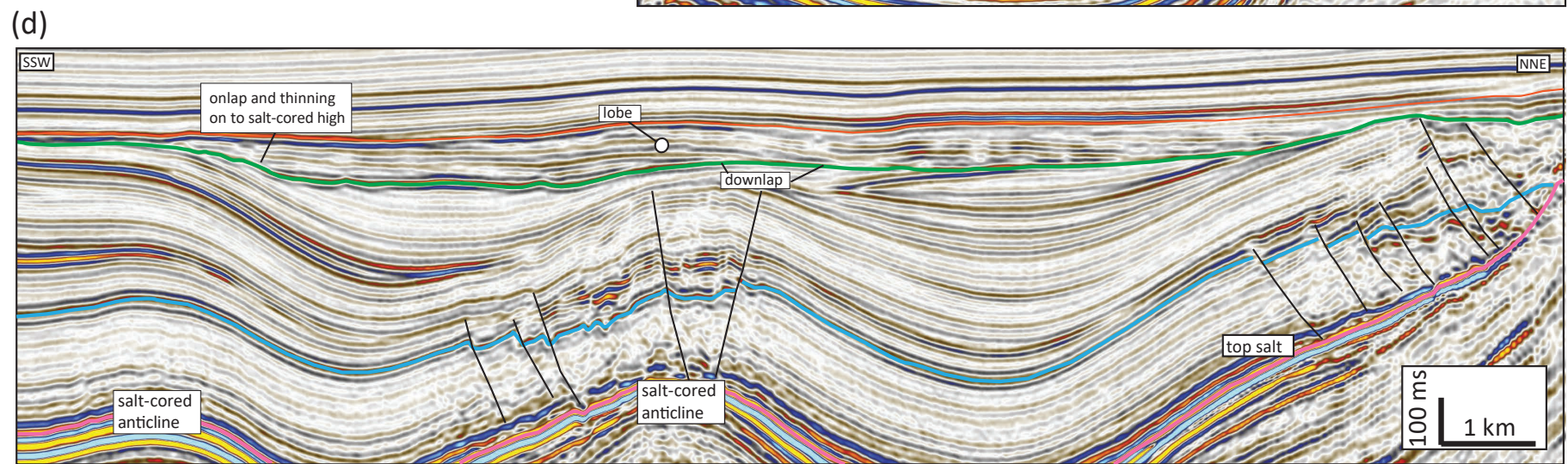
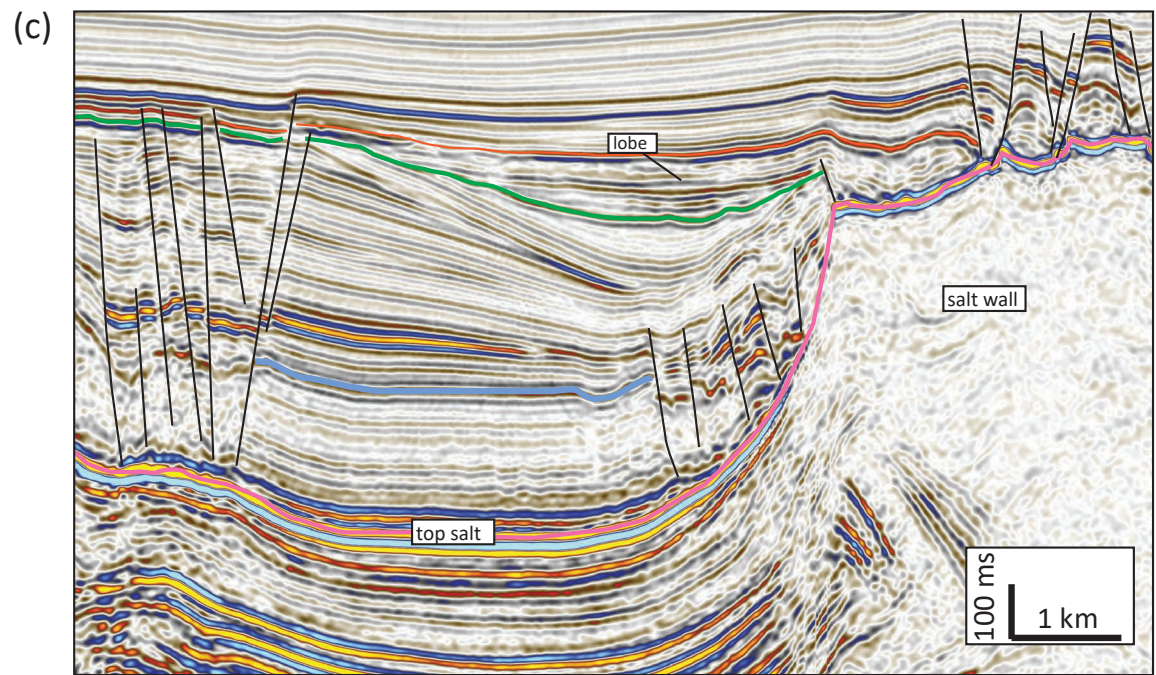


FIGURE 12: Isochron (a) and seismic attribute blending (b) for unit 3 covering minibasins I and J illustrating salt-related controls on coeval deep-water depositional systems. Increase in thickness occurs around salt-cored folds and associated to lobes deposition where frontally confined. Deflection of submarine channel 2 (ch2) occurs around a salt-cored fold in Minibasin J and this is highlighted in the amplitude contrast attribute in the inset. See interpretation and location in Figure 10. (c) and (d): Seismic sections across the distal part of minibasin I, illustrating lobes deposition and confinement. (e) and (f) Seismic sections across and along minibasin J, illustrating salt-related controls on deposition. Location of seismic sections are highlighted in Figures 12 a and b

FIGURE 12

Minibasin I



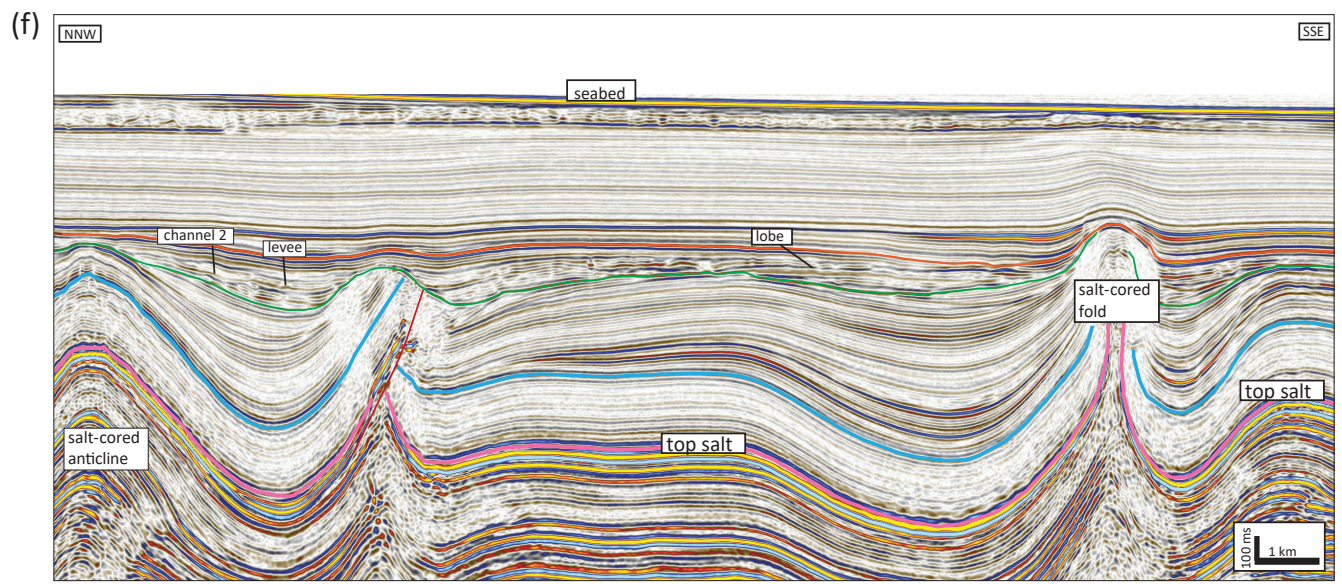
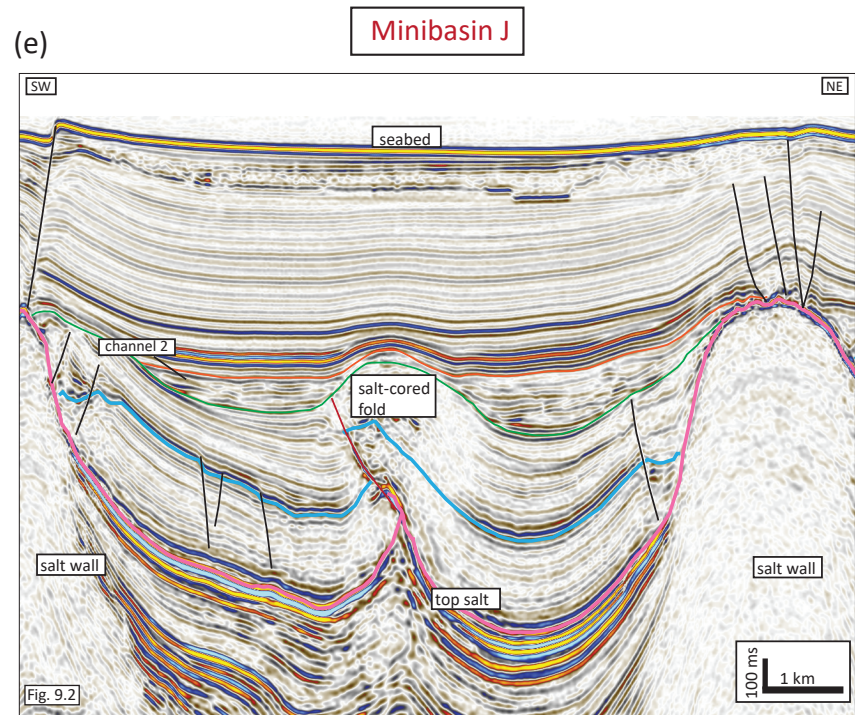


FIGURE 12

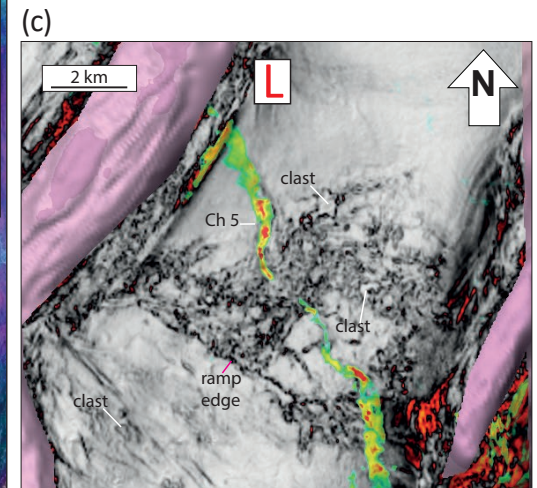
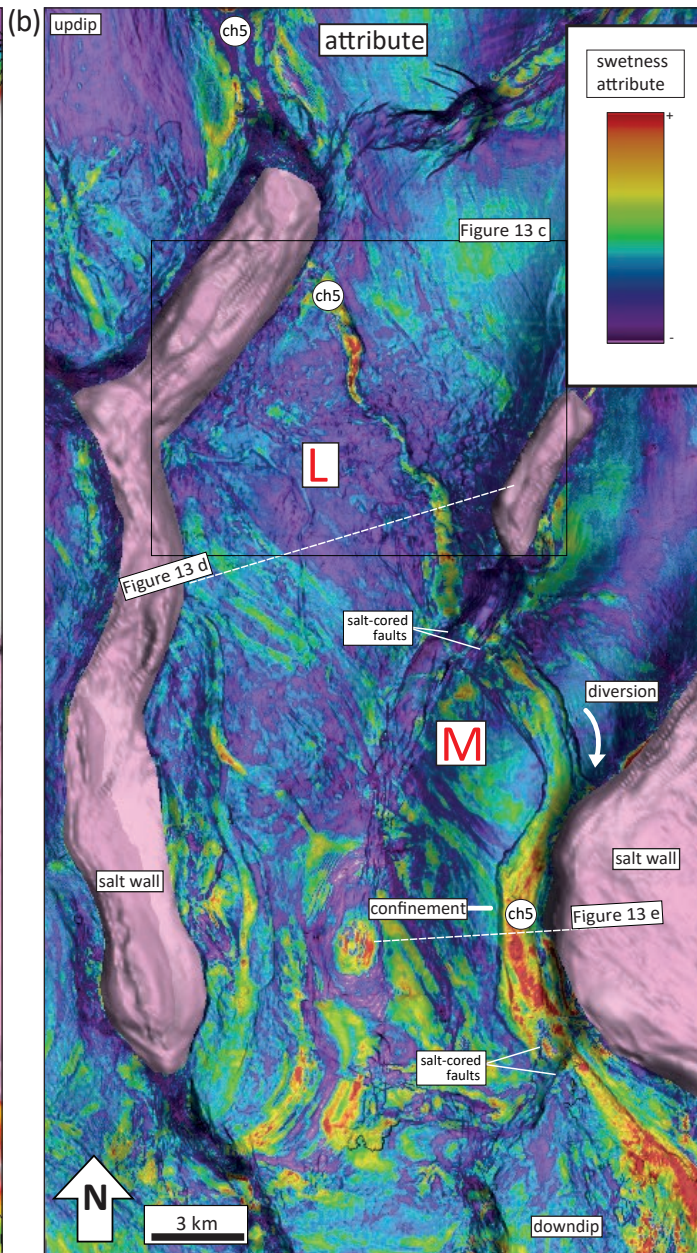
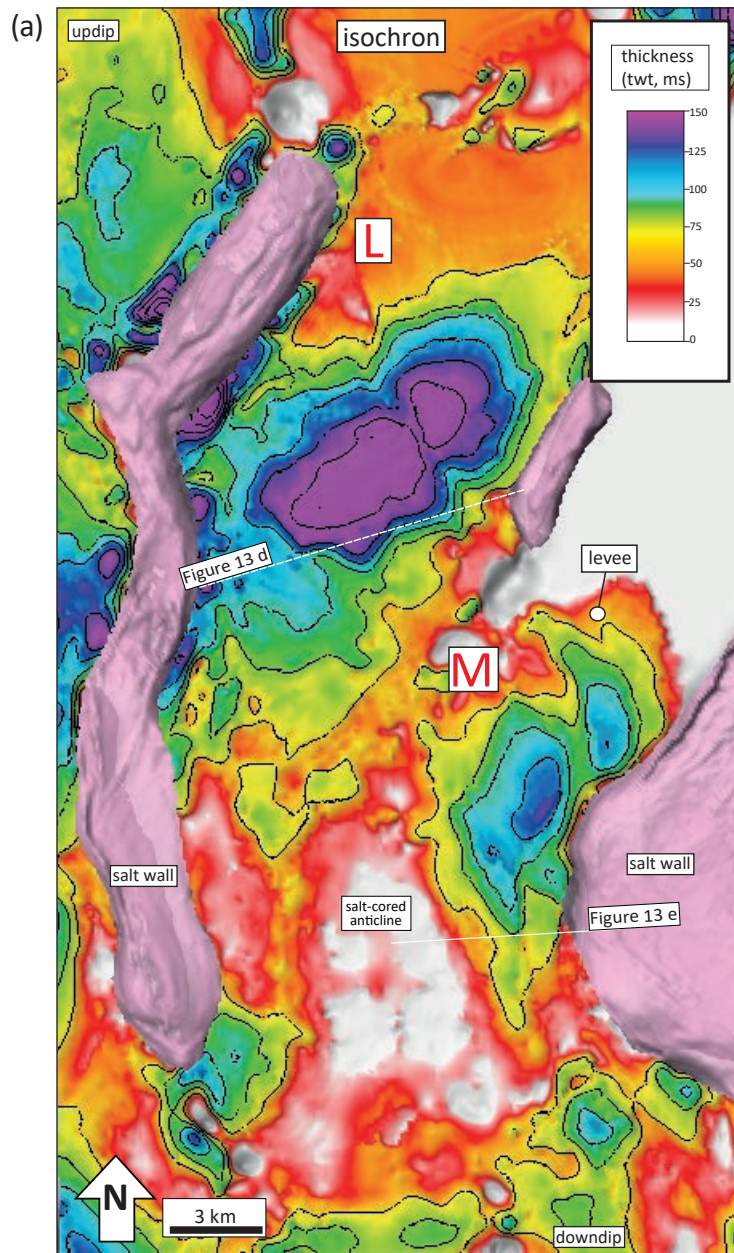
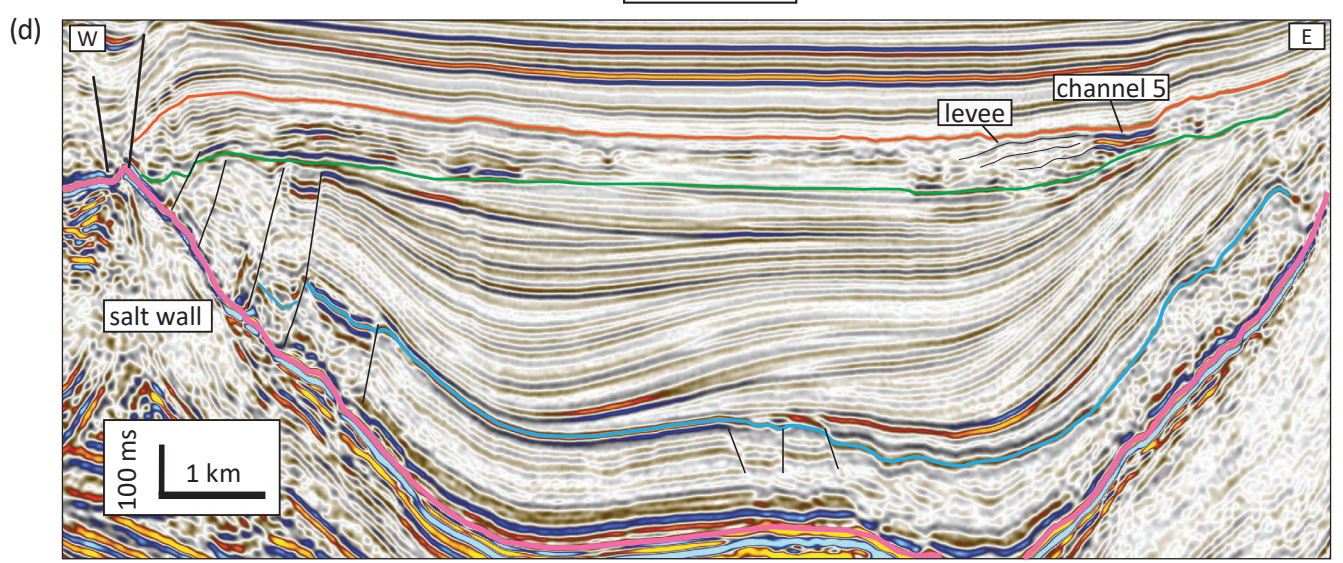


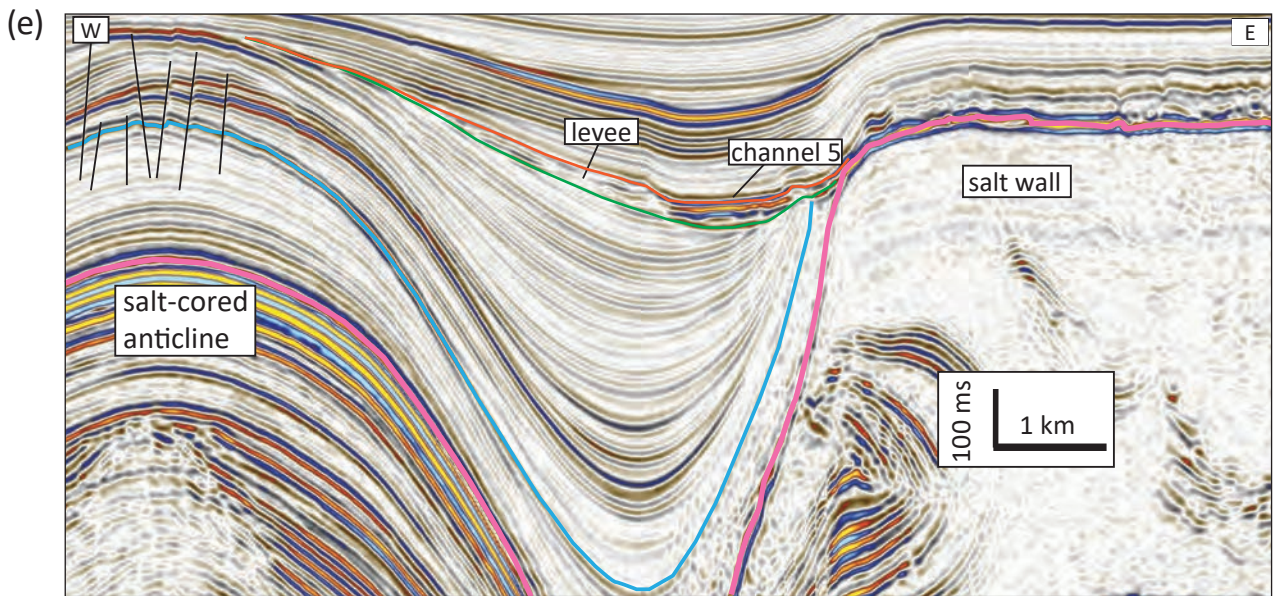
FIGURE 13: Isochron (a) and seismic attribute blending (b) for unit 3 covering minibasin L and M illustrating deep-water submarine channels across present-day minibasins and salt-related controls. Channel 5 (ch5) is oriented SE and relatively thinner along Minibasin L but gets diverted and laterally confined and wider along Minibasin M due to the bounding salt-wall oriented nearly-perpendicular to the slope. See location and interpretation in Figure 10. (c) A local MTC underlies submarine channel 5 within Minibasin L. Seismic sections in (d) and (e) highlight bounding salt walls and salt-cored anticline, channel 5 and associated levees in minibasins L and M.

FIGURE 13 (cont)

Minibasin L



Minibasin M



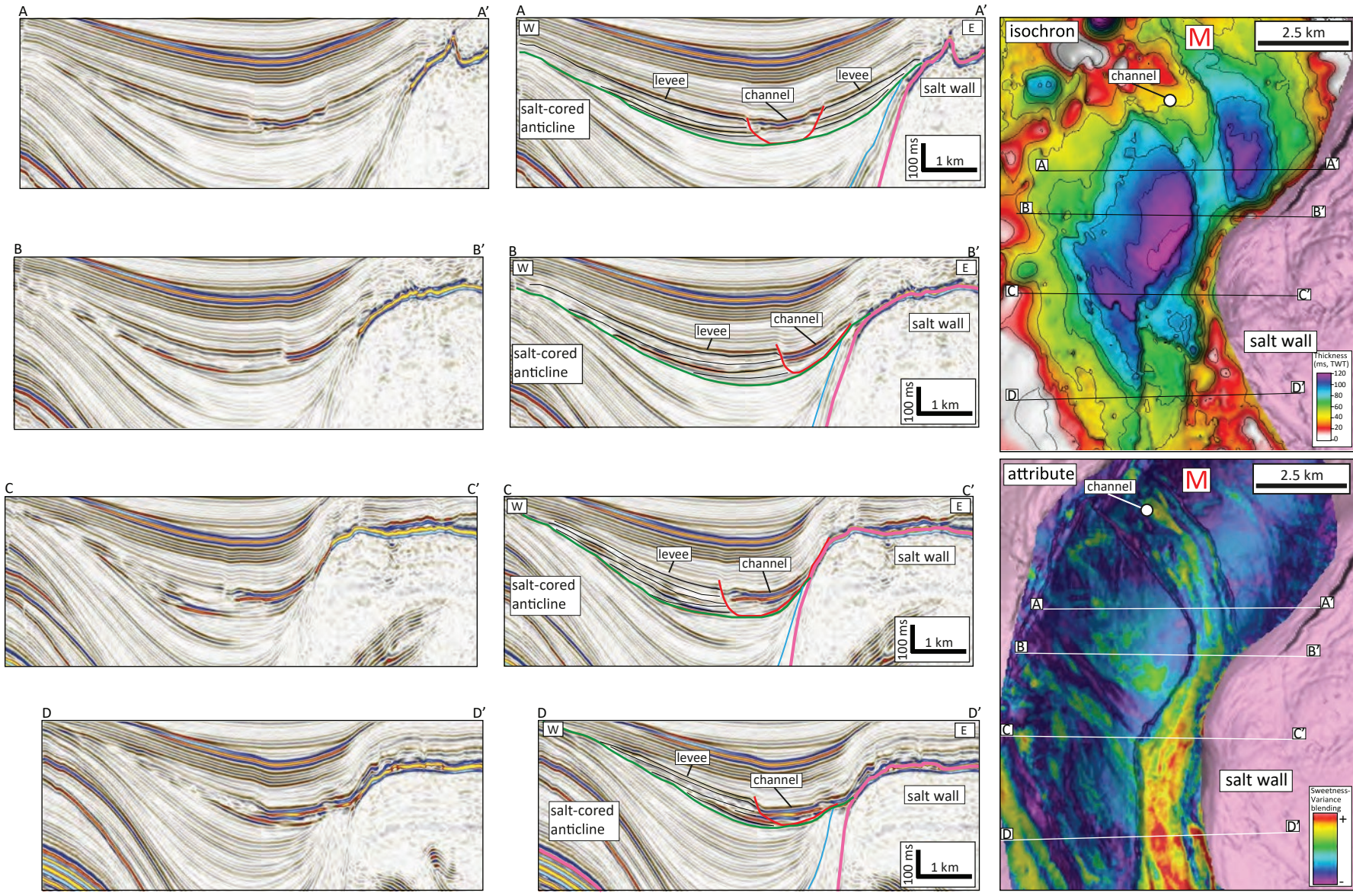
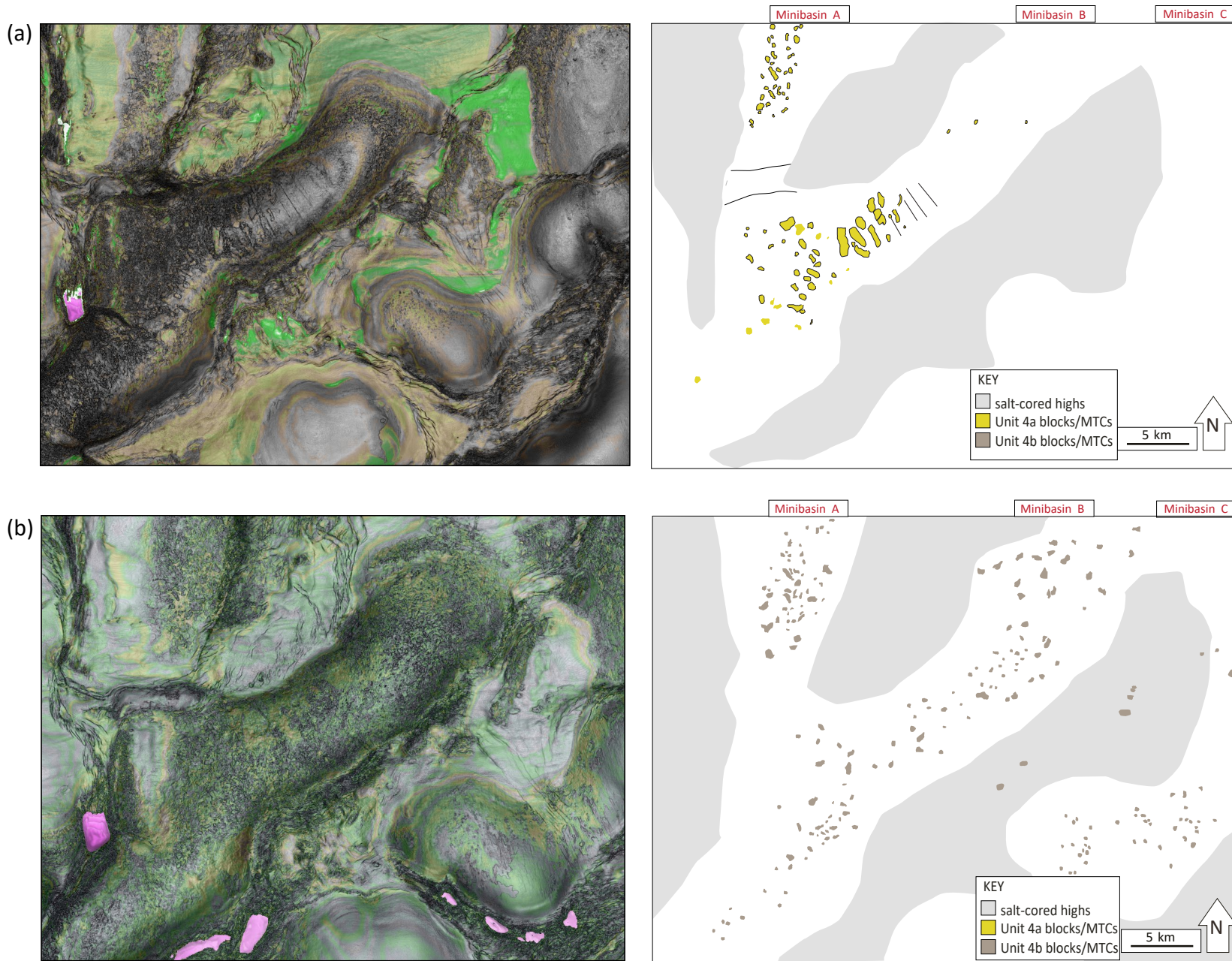


FIGURE 14: : Submarine channel and levee geometry variations along Minibasin M. Isochron and section A-A' illustrate wing-shaped levees developed adjacent to the channel. Seismic attribute and sections illustrate that high-amplitudes are restricted to the channel axis, whereas the levees are characterized by medium to low amplitudes. Channel onlaps and its apparently tilted and rotated where it gets diverted and closer to the bounding salt wall (section B-B'). Intra-levee reflections are rotated towards the channel axis (sections C-C' and D-D') indicating salt movement during deposition



**FIGURE 15:** Seismic attributes sweetness and variance blending and interpretation of intra-minibasin clasts characterizing MTCs in proximal updip minibasins during deposition of Unit 4. See location of minibasins A, B and C in regional map Figure 6c and seismic and geoseismic sections in Figures 9a and 9b.



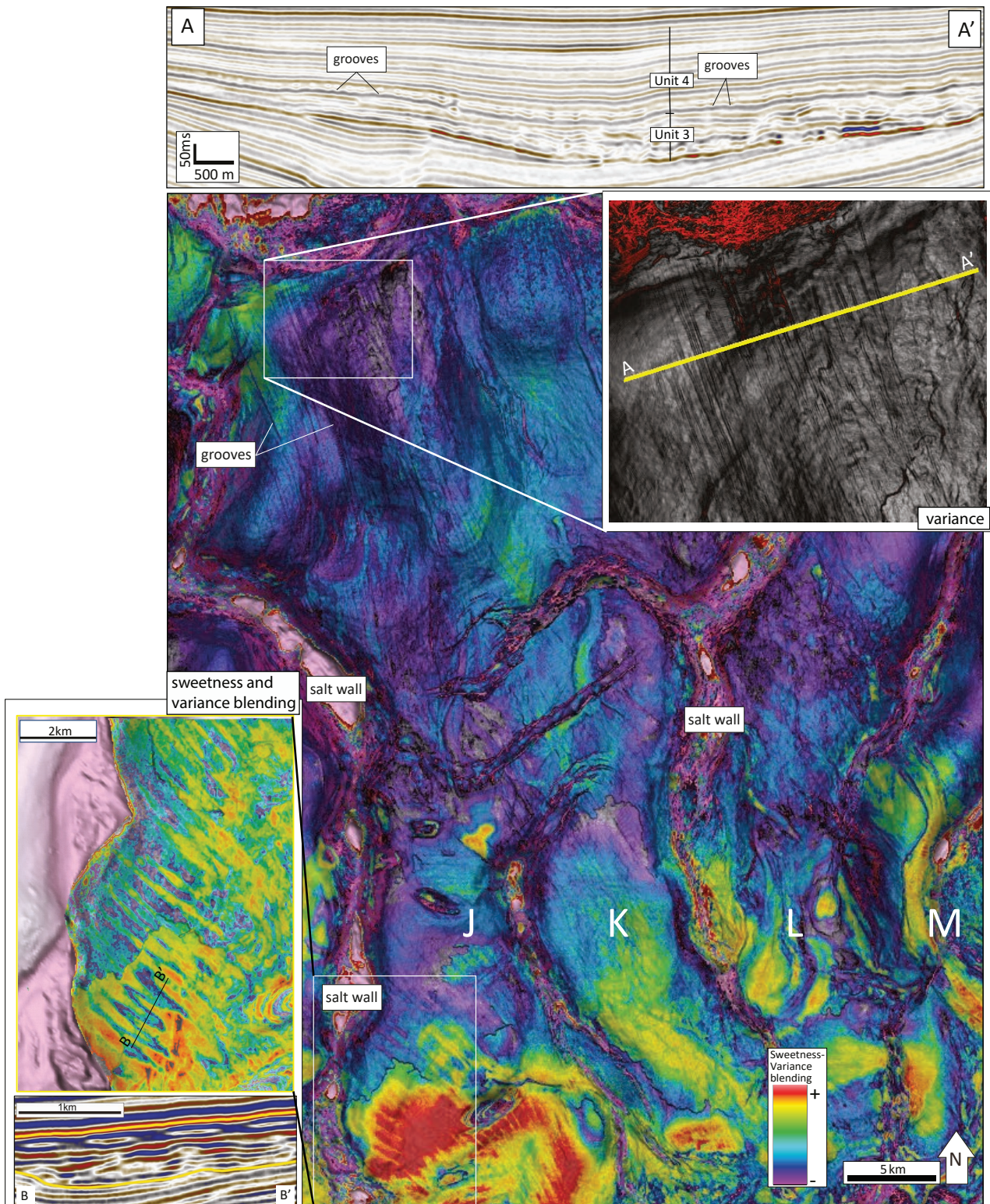
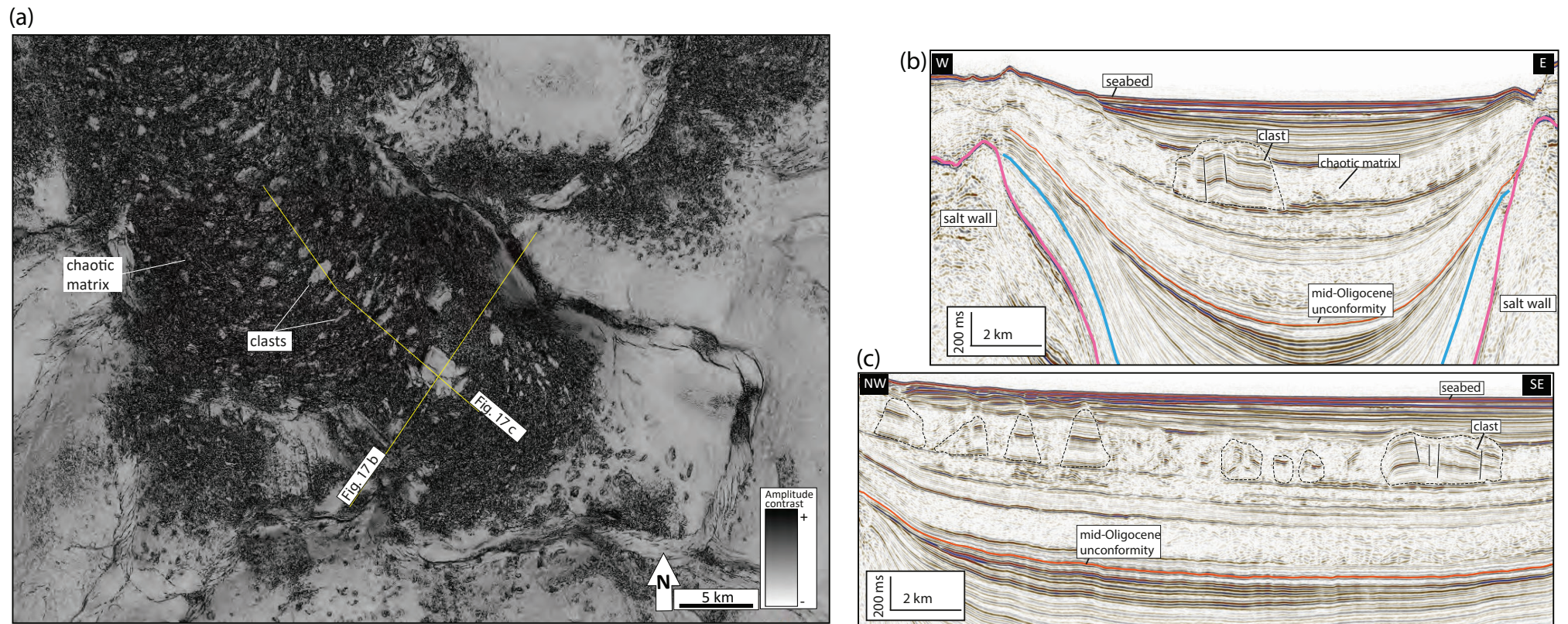
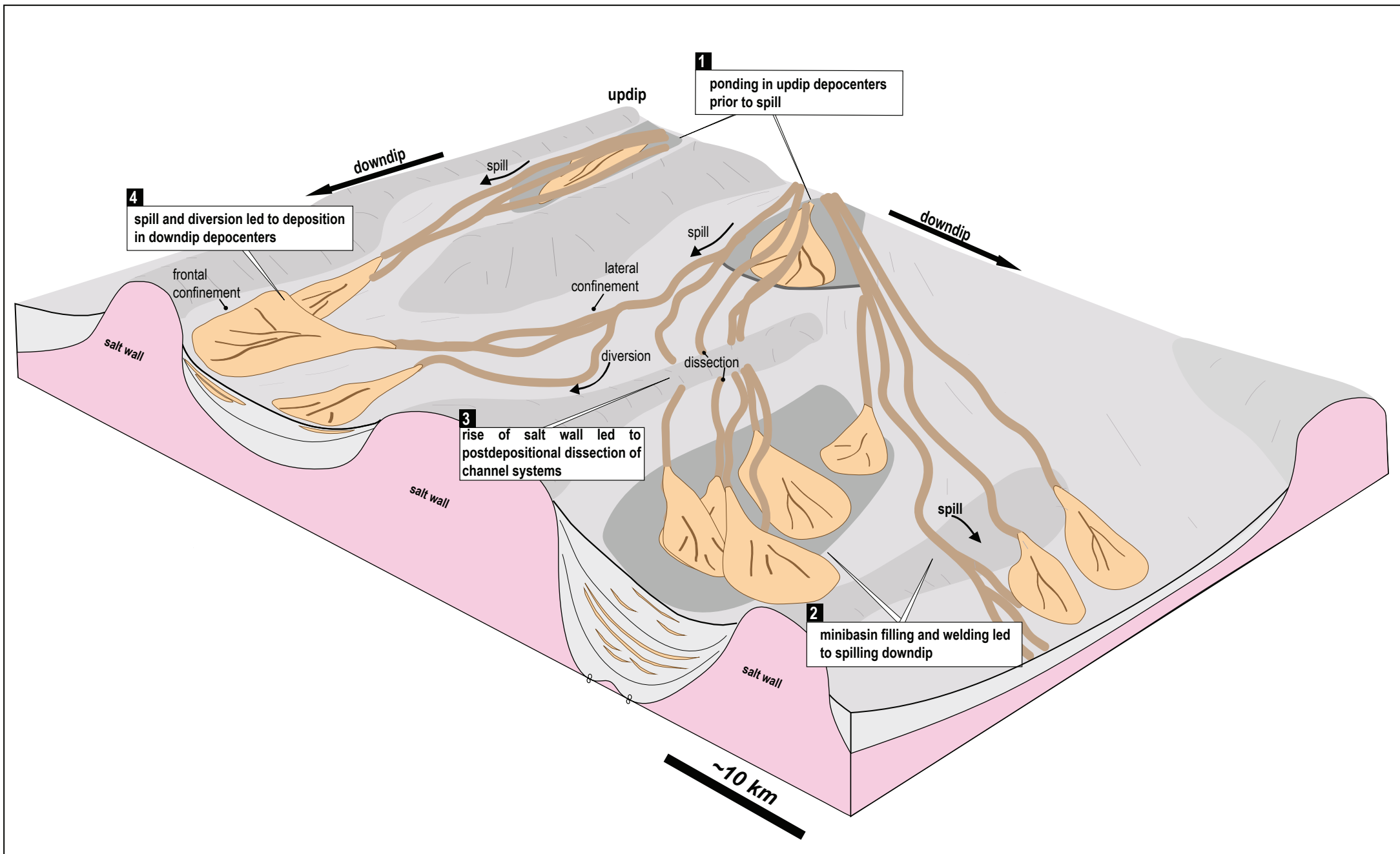


FIGURE 16: Seismic attributes and seismic sections illustrating linear grooves characterizing regional-scale MTCs across the Sao Paulo inner fold-belt and the Sao Paulo plateau and highlighting a drastic change in the evolution of the central deep-water Santos Basin during deposition of Unit 4. See location of minibasins J, K, L, and M in regional map Figure 6c



**FIGURE 17:** Seismic expression of MTCs within Unit 5. a) Amplitude contrast attribute of intra-Unit 5 horizon highlighting clasts and a chaotic matrix; b) seismic section across the minibasin; c) seismic section along the minibasin.



**FIGURE 18:** a) Block diagram illustrating sedimentation within proximal minibasins: Ponding occurs within proximal, updip, intra-minibasin depocenters prior to spilling and deposition along the minibasins (1). Filling of minibasins and subsequent welding of minibasin floor led to spilling towards downdip minibasins (2). Channel systems are post-depositionally dissected by rising salt walls bounding the present-day minibasins (3). Subsequent spilling from updip depocenters and diversion by rising salt walls led to deposition in downdip depocenters (4).

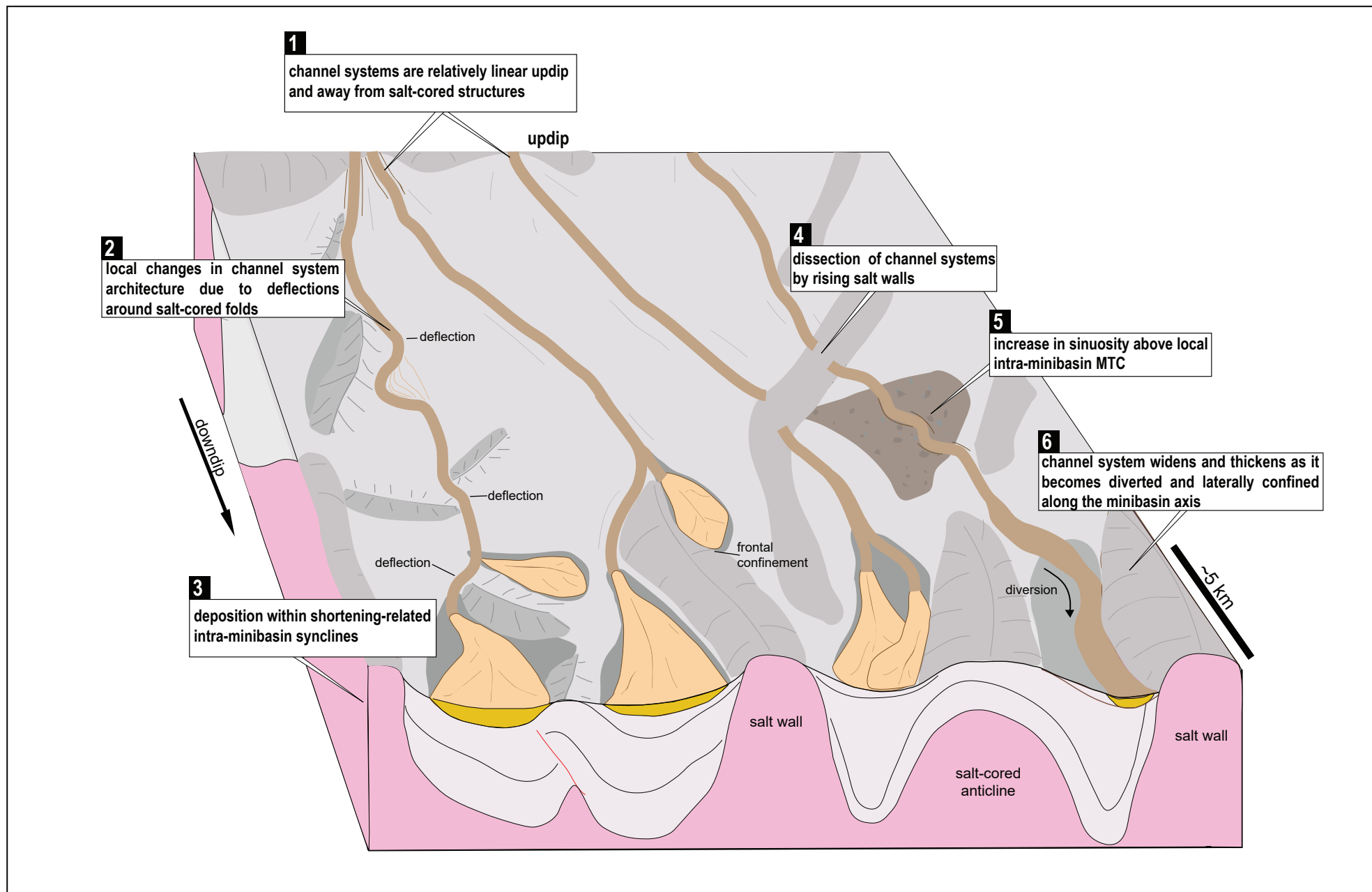


**FIGURE 18 (cont.):** b) Block diagram summarizing salt-related controls in deep-water sedimentation across part of the São Paulo inner fold-belt and the distal minibasins in the São Paulo plateau. Channel systems spilling from the proximal minibasins are relatively linear updip and away from salt-cored structures (1). Local controls in channel system architecture (2) and sediment distribution (3) are observed. Present-day salt walls dissected channel systems similarly to what it is observed in the updip minibasins (4). The architecture of channel systems varies between adjacent minibasins controlled by the presence of intra-minibasin MTCs and confinement (5 and 6).

TABLE 1: Vertical seismic resolution of intervals of interest and across structural domains

Structural Domains	Borehole	Formation	Interval Velocity (m/s)	Frequency (Hz)	Resolution (m)
Proximal deep minibasins	329D	Marambaia	2125	52	10
		Itajai-Acu	3525	37	24
		Itanhaem	4300	17	63
Medial shallow minibasins	369A	Marambaia	1700	37	11
		Itajai-Acu	2300	30	19
		Itanhaem	3700	23	42
Distal elongated minibasins	723C	Marambaia	1500	45	8
		Itajai-Acu	1900	42	11
		Itanhaem	2750	30	23
	709	Marambaia	1500	48	8
		Itajai-Acu	2200	42	13
		Itanhaem	2300	30	19

Table 2: Seismic facies interpretation and seismic attributes calibration with lithology from borehole 329D, minibasin C. See Figure 4a for location

Seismic facies	Amplitude	Continuity	Swetness attribute response	Variance attribute response	Lithology proportions (borehole 329D)
SF1	High	Variable	Moderate to high (light blue to red colors)	Low (grey to white colours)	40% sandstone 56% mudstone 4% siltstone, marlstone and carbonate
SF2	Modetate to high	Discontinuous	Medium (light blue)	High (black colour)	56% sandstone 28% mudstone 16% marlstone and carbonate
SF3	Low	Continuous	Low (dark blue to dark pink colors)	High (black to red colors)	70% mudstone 25% sandstone 5% marlstone and carbonate

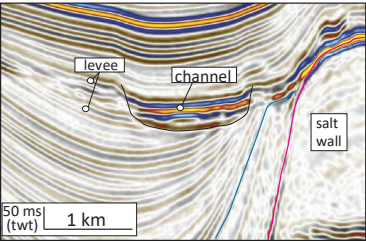
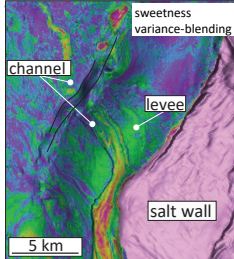
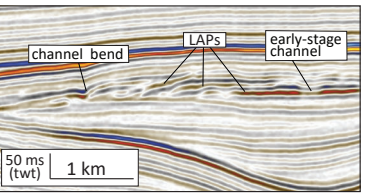
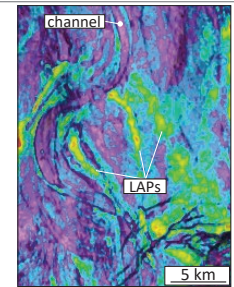
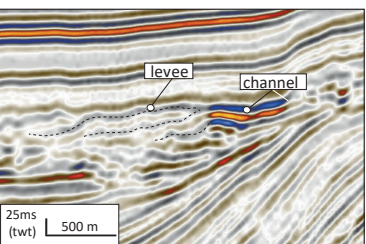
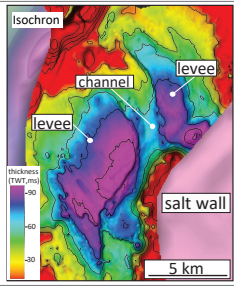
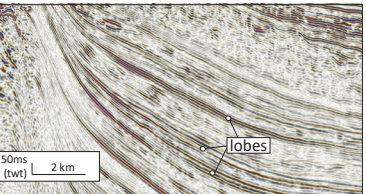
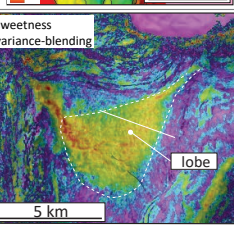
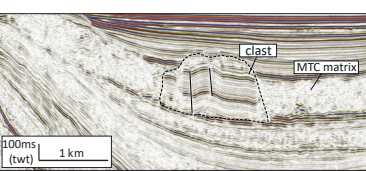
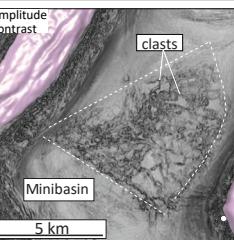
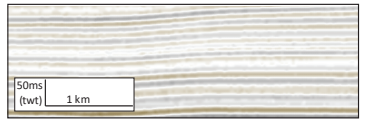
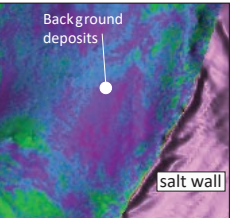
<b>Deepwater depositional elements</b>					
	<b>Seismic Stratigraphy</b>	<b>Seismic geomorphology</b>	<b>Reflection character</b>	<b>Geometry</b>	<b>Interpretation</b>
<b>Channels</b>			Parallel, continuous, moderate-to-high amplitude seismic reflections. Some low-amplitude channels also occur  Bases are flat and weakly erosional  20-150 m thick	Relatively narrow, elongate, low sinuosity, channel forms  0.2 - 3 km wide up to 200 km long sinuosity (<1.5)	Turbidite-fed submarine channels (e.g., Kolla et al. 2000; Fonesu, 2003; Prather, 2003; Gee and Gawthorpe; 2006, 2007; Alves et al., 2009) Sandstone-prone channel-axis if defined by SF1 (Table 2). Siltstone and mudstone-prone if defined by SF3 (Table 2)
			Laterally stacked moderate-to-high amplitude seismic reflections dipping in towards the channel axis  up to 50 m thick	Crescent-shaped forms flanking the inner bend of more sinuous channels  up to 1 km wide up to 5 km long	Lateral accretion packages developed due to channel lateral migration (e.g., Kolla et al., 2000; Abreu et al. 2003; Janocko et al. 2013)  Sandstone or siltstone prone when defined by SF1 seismic facies (Table 2)
<b>Levees</b>			Wedge-shaped seismic packages of subparallel, low-to-moderate amplitude seismic reflections adjacent to the channels  up to 150 m thick but typically thinner	Asymmetrically developed on both sides of the channel axis  up to 5 km wide up to 10 km long	Levees deposited by sediment gravity-currents that escaped from submarine channels (e.g. Fonesu, 2003; Gee and Gawthorpe, 2007; Clark and Cartwright, 2011; Ortiz-Karpf et al., 2015)  Generally fine-grained mudstone or siltstone composition based on seismic facies SF3 (Table 2)
<b>Lobes</b>			Tabular to mounded packages of subparallel, continuous, moderate-to-high amplitude seismic reflections  thinning towards the fringes downlap  up to 200 m thick	Sub-rounded, to lobate to elongate  up to 5 km wide up to 10 km long	Lobes deposited at the mouth of submarine channels (e.g. Gee and Gawthorpe, 2006; Saller et al., 2008; Prélat et al., 2010) Largely composed of sandstone based on high amplitude and evidence of differential compaction
<b>MTCs</b>			Discontinuous to chaotic, low-to-moderate amplitude seismic reflections up to 200 m thick Basal surfaces are sharp and not erosional or highly irregular with v-shaped grooves Clasts are parallel continuous moderate-to-high-amplitude reflections. Up to 200 m thick	Fan-shaped or subparallel lineations up to 50 km long  Semi-circular to angular clasts of various sizes:  0.1 to 200 m wide 0.2 to 1 km long	Mass transport complexes (e.g., Posamentier and Kola, 2003; Gee and Gawthorpe, 2006, 2007; Gamboa et al. 2010; Jones et al. 2012; Oluboyo et al. 2014)  Variable composition based on seismic facies (SF2 and SF3, Table 3)
<b>Background deposits</b>			Parallel, continuous, low-to-moderate amplitude reflections	Continuous with slight variations in seismic amplitudes	Fine-grained deep-water deposits emplaced by dilute turbidity currents or suspension setting (e.g., Hadler-Jacobson et al. 2007; Oluboyo et al. 2014)

Table 3: Seismic geomorphologic elements identified within the post-salt sequence in central deep-water Santos Basin. Interpretation is mainly based on the analysis of the seismic stratigraphy and seismic geomorphology